Plasma Wave Heating in the E-region

A Thesis Submitted to the

College of Graduate Studies and Research

in Partial Fulfilment of the Requirements

for the degree of Master of Science

in the Department of Physics and Engineering Physics

University of Saskatchewan

Saskatoon

By

Arpita Barua

Permission to Use

In presenting this thesis in partial fulfilment of the requirements for a Postgraduate degree from the University of Saskatchewan, I agree that the Libraries of this University may make it freely available for inspection. I further agree that permission for copying of this thesis in any manner, in whole or in part, for scholarly purposes may be granted by the professor or professors who supervised my thesis work or, in their absence, by the Head of the Department or the Dean of the College in which my thesis work was done. It is understood that any copying or publication or use of this thesis or parts thereof for financial gain shall not be allowed without my written permission. It is also understood that due recognition shall be given to me and to the University of Saskatchewan in any scholarly use which may be made of any material in my thesis.

Requests for permission to copy or to make other use of material in this thesis in whole or part should be addressed to:

Head of the Department of Physics and Engineering Physics

163 Physics Building

116 Science Place

University of Saskatchewan

Saskatoon, Saskatchewan

Canada

S7N 5E2

Abstract

It has been shown in previous studies that at 110 km altitude, the electron temperature can be quite large in the presence of strong electric fields. This thesis explores the possibility of deviations from the normal trends in the high latitude E-region electron heating in reaction to strong electric fields. The study is based on data from the EISCAT Incoherent Scatter Radar during the International Polar Year. Out of a large number of possibilities (the radar operated essentially on a continuous basis for a year) only seven events proved to have sufficiently strong electric fields and large enough plasma densities to be characterized as 'good heating events'. The electron temperature enhancements in these events, at 110 km, were several hundred K above from the background temperature and correlated well with ion temperature at 150 km altitude. The results for these good events agreed very well with past studies, aside from the smaller starting temperatures which were likely connected to the quiet solar conditions at the time. This stated, a different type of E region electron heating event was identified. In that case the E region electron densities were small (night-time conditions free of electron precipitation) and the electron temperatures reached a maximum near 150 km altitude. In those events the electron temperature enhancements extended down to the lower altitudes, introducing small, but detectable, electron temperature enhancements all the way down to 105 km altitude.

.

Acknowledgements

I would like to thank my supervisor, Dr. Jean-Pierre St.-Maurice, who provided me with the opportunity to come to the University of Saskatchewan to work on this project. I am very grateful for his patience and guidance. His advice and push was the great encouragement for me. I am truly blessed to have had such a supervisor. I also like to thank Dr. Andrei Smolyakov for his useful guidance. I would also like to acknowledge my advisory committee members Dr. Andrei Smolyakov, Dr. Rob Pywell and Dr. Adam Bourassa. Special thanks to Dr. Pasha Ponomarenko, Bill Marshall, Kevin Krieger, Dieter André and Lindsay Goodwin for their help.

To Mom, Dad, Sumit and Amit and my extended family in India. Words cannot describe your love, efforts and patience. A special thank you also goes to Shaon Ganguly and my friends in Bangladesh and Canada. I thank you all for your love and confidence.

CONTENTS

List of Tables

List of Figures

List of Abbreviations

EUV	Extreme Ultra-Violet
DMSP	Defense Meteorological Satellite Program
HF	High Frequency
IMF	Interplanetary Magnetic Field
IPY	International Polar Year
ISR	Incoherent Scatter Radar
MLT	Magnetic Local Time
RADAR	RAdio Detection And Ranging
UT	Universal Time
IRI	International Research Institute
ACF	Autocorrelation function
CP	Common Program

List of Nomenclature

$\boldsymbol{B}$	Geomagnetic field strength
$\boldsymbol{E}$	Electric field
e	Charge of an electron
n	Number density
H	Scale height
u	Mean velocity
P_i	Chemical production
L_i	Chemical loss
τ	Stress tensor
J	Current density
k_b	Boltzmann constant
m	Mass
p	Pressure
ν	Collision frequency
D_a	Ambipolar diffusion
g	Gravitational constant
T	Temperature
z	Altitude
t	Time
q_{max}	Maximum production rate when $\theta = 0°$ for a given reduced height
χ	Solar zenith angle,
q	Heat
W	Energy scattered by a single electron into solid angle
r_e	Electron radius
Ψ	Angle between the direction of the electric field and the observer

Δfe	Magnitude of Doppler shift
λ	Radar wavelength
V	Velocity
Q	Ion-neutral scattering cross-section
D'	Non-dimensional ion drift velocity

Chapter 1

INTRODUCTION

This thesis describes the influence of high latitude electric fields on the E-region electron temperature. It is observed that the electron temperature in the E-region responds to the presence of a strong magnetospherically-driven electric field and correlates with the ion temperature of the lower F-region. The present thesis is a further study of the relation between the E-region heating and the electric field. To present the electron temperature behaviour of the E-region, data from the European Incoherent Scatter Scientific Association (EISCAT) incoherent scatter radar (ISR) have been used. Before getting into the subject, it is important to have a clear view about several ionospheric processes such as the chemistry, magnetospheric driver and the energetics. The rest of the chapter will cover a brief description of these topics.

1.1 Atmospheric Layers

As the altitude increases, the neutral atmosphere can be divided into four layers, namely, the troposphere, the stratosphere, the mesosphere, and the thermosphere. These layers are determined by the temperature profile shown in Figure 1.1. The troposphere is the lowest layer and extends to 15 km from the Earth's surface. The stratosphere is the second layer that extends up to approximately 50 km altitude and contains 20 percent of the molecules. Just above the stratosphere, in the height range 50-85 km is the mesosphere. The stratosphere and the mesosphere together are referred to as the middle atmosphere. Beyond the mesosphere, the rest of the atmosphere is the thermosphere. The thermosphere starts around 85 km where the coldest

atmospheric temperatures are recorded. The thermosphere contains electrically charged particles as well, in regions called the ionosphere and the magnetosphere.

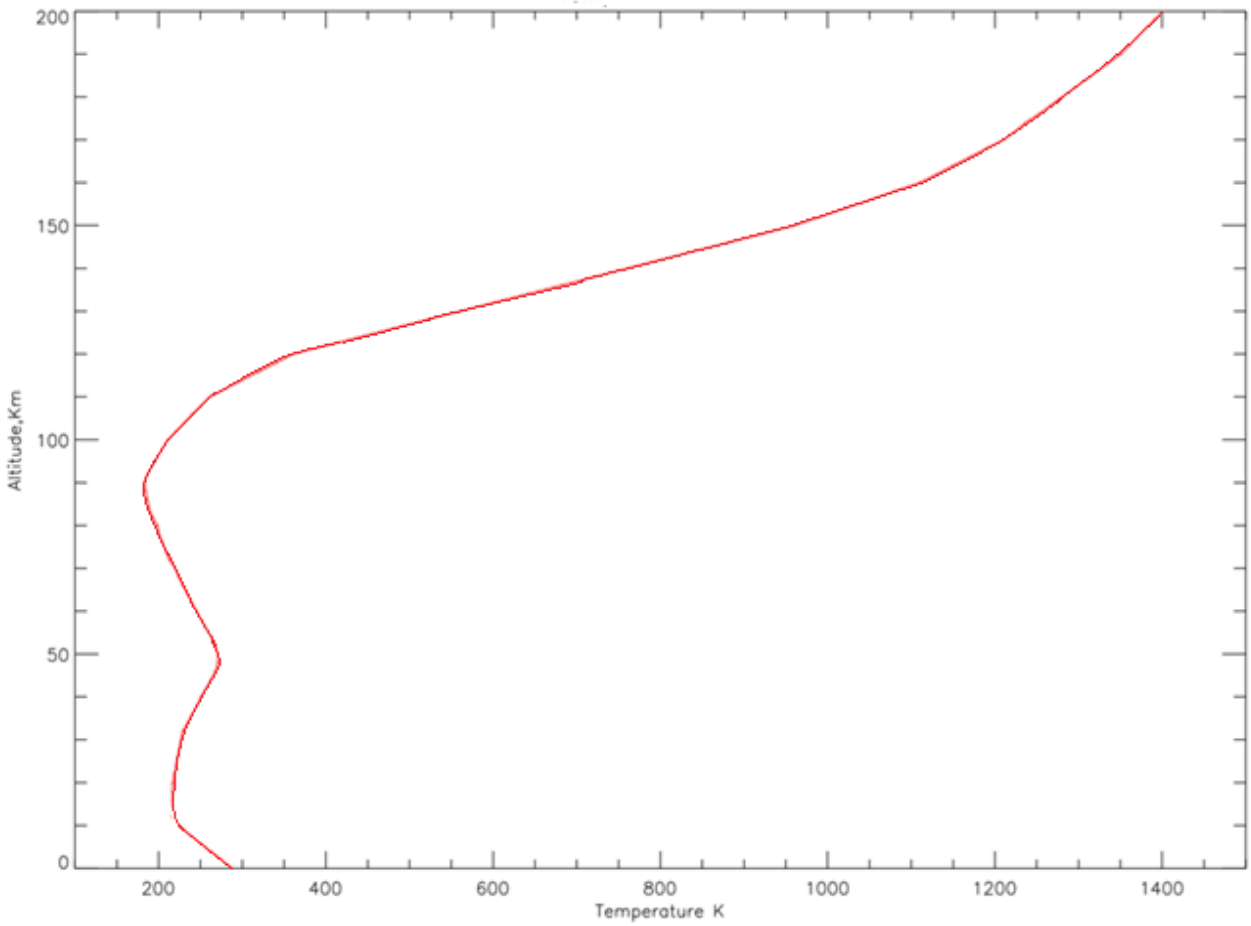

Figure 1.1: Temperature profile of the Earth's atmosphere based on the U.S. Standard Atmosphere of 1976 Data: *(NOAA, 1976).*

In the thermosphere the temperature first increases with altitude to an overall maximum value ($\sim 1000\,K$) and then becomes constant with altitude *(Schunk & Nagy, 2000).* In the lower ionosphere, a vital role is played by chemistry which starts with the photoionization and photo-dissociation of O_2 and N_2 molecules. However, the topside ionosphere is dominated by diffusion.

Figure 1.2 shows the net structure of the neutral density profiles of N_2, O_2, O, He and H with height. The heavy molecular constituents dominate at low altitude and the atomic neutrals dominate at high altitude *(Schunk & Nagy, 2000)*.

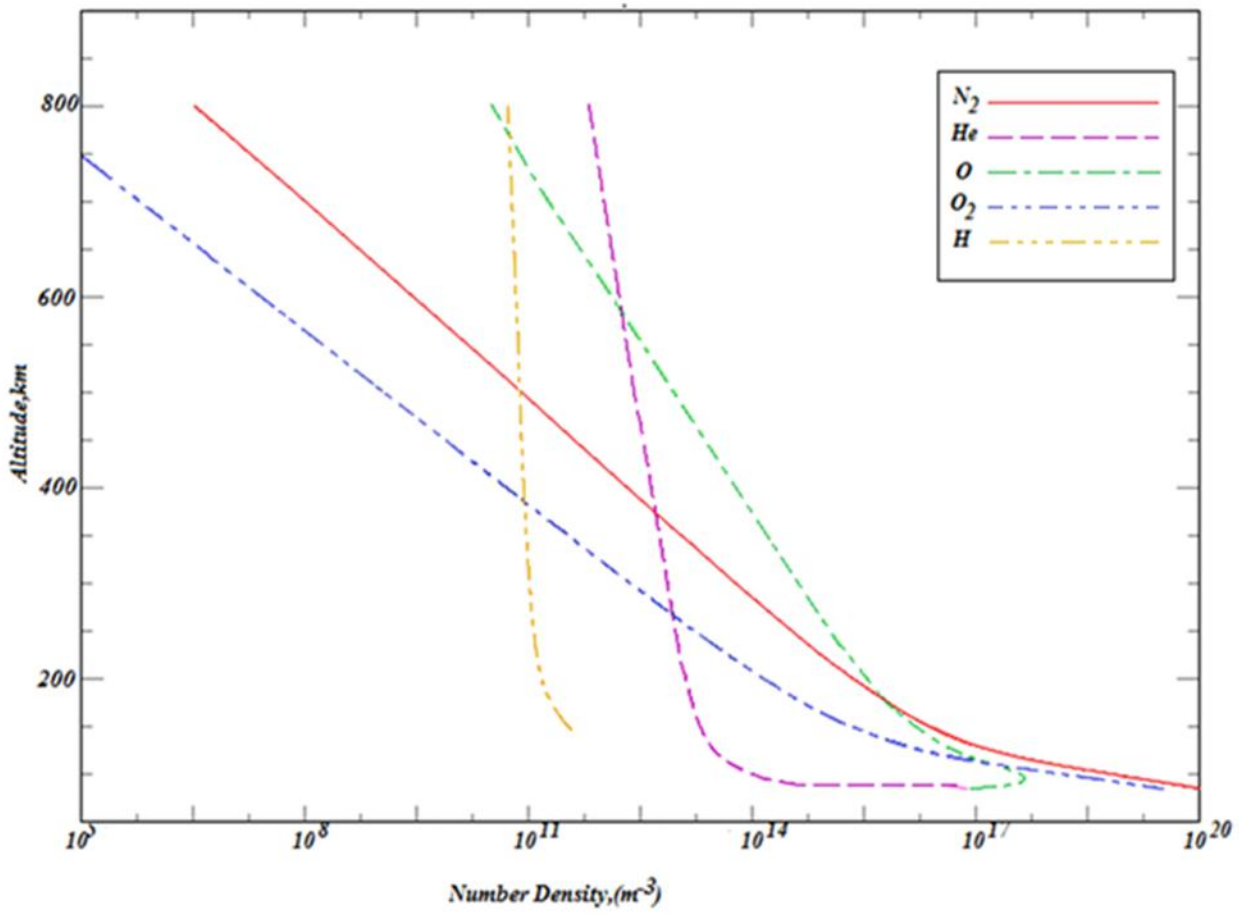

Figure 1.2: Height variation of the main atmospheric constituents according to U.S. standard atmosphere, 1976

1.2 Ionosphere

In 1883, Belfour Stewart discovered the ionosphere *(Roche, 1990)*. The ionosphere consists of plasma and neutral particle mixture *(Baumjohann & Treumann, 1996)*. So the ionosphere can be defined as the region of an atmosphere where a significant number of thermal (<1eV) electrons and ions are present *(Schunk & Nagy, 2000)*. This section discusses the ionospheric composition, its structure and its temperature.

1.2.1 Ionospheric layers

The variability and the structure of the ionosphere are the results of chemical processes. In the composition section, the ionospheric chemistry will be discussed. The ionosphere can be separated into three designated layers identified as the D, E and F-regions. The D-region has a complex and lesser known chemistry. Here, only the E-region and F-region layers will be discussed. During the daytime, electron densities of the two regions are:

E region: $n_e = 10^{10} - 10^{11}\ \ m^{-3}$

F region: $n_e = 10^{11} - 10^{12}\ \ m^{-3}$

The E-region has a simple photochemistry and high electrical conductivity *(Hargreaves & Hunsucker, 2003)*. The E-region peak electron density is around 110 km altitude. During periods of high solar activity, the F-region can be divided into two, namely, the F1 and F2 regions. The F1 region density peak occurs at 200 km and for the F2 region, it nearer 250 km. Transport processes limit the density near the peak of the F region. Table 1.1 shows the characteristics of the three layers.

Layer	Altitude (km)	Major Component	Production cause
E	90-140 km	NO^+, O_2^+	Lyman Beta, Soft X-rays, UV Continuum
F1	140-200 km	NO^+, O^+	He II, UV Continuum (100-800 Å)
F2	200-400 km	N^+, O^+	He II, UV Continuum (100-800 Å)
Topside F	>400 km	O^+	Transport from Below
Plasmasphere	>1200 km	H^+	Transport from Below

Table 1.1: Layers of the ionosphere *(Rich & Basu, 1985)*

Figure 1.3 shows a typical electron density profile for the ionosphere (in cm^{-3} instead of m^{-3}). As can be seen from the figure the electron density above 100 km altitude divides the ionosphere into three regions. In these three layers, different kinds of radiation, recombination, and transport processes are behind the electron density variation. In the lower F-region and below, the loss rate depends on recombination whereas in the topside F-region it depends on diffusion.

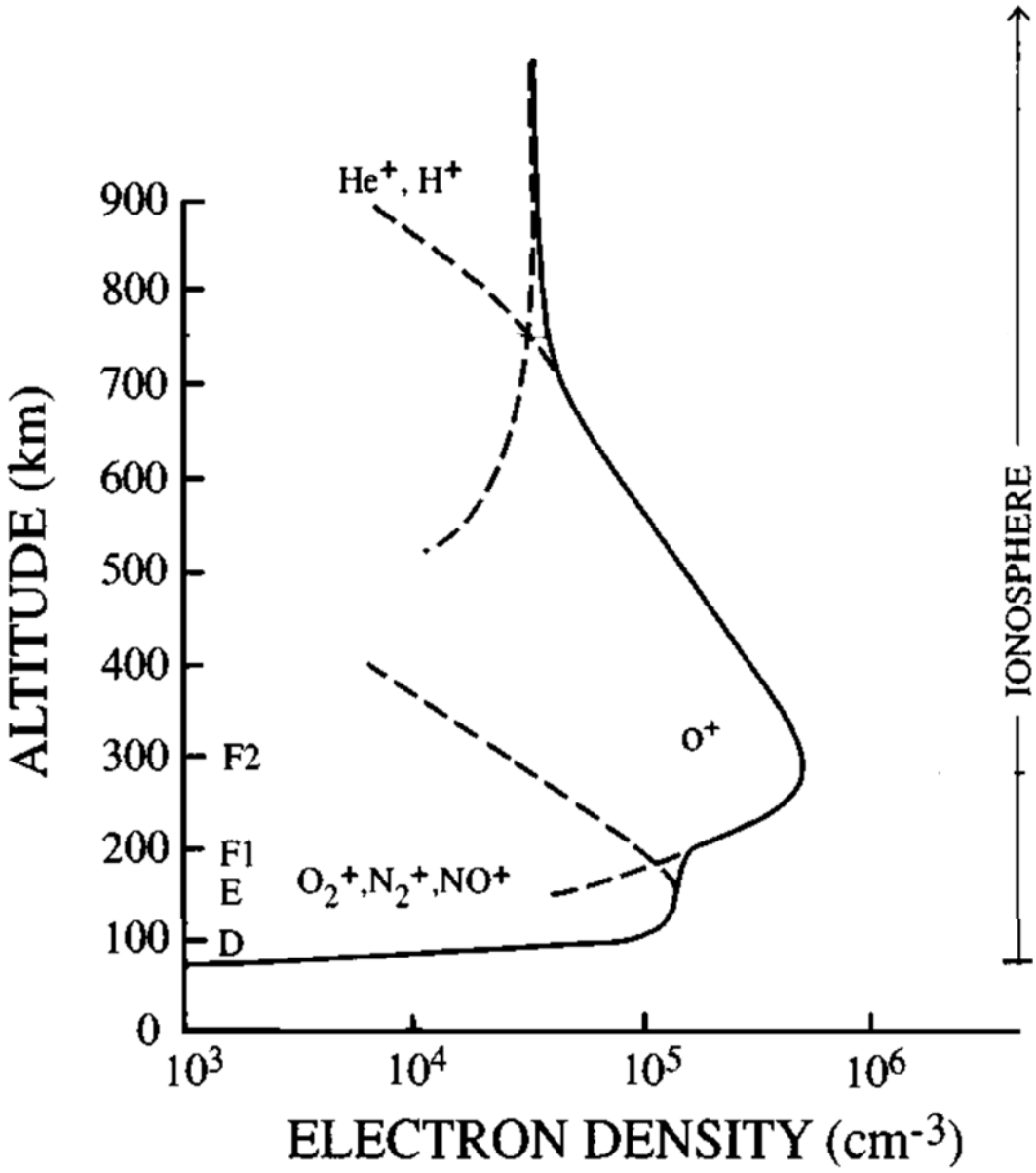

Figure 1.3: Profile plot of the electron density of the layered ionosphere *(Schunk & Nagy, 2000)*

1.2.2 Composition

The ionosphere has various constituents produced by photoionization. Solar X-rays and shorter wavelength ultraviolet (EUV) radiation ionize both molecules and atoms. This leads to interchange, charge transfer and recombination reactions. However, chemistry is not the only factor to consider. The continuity equation is used to describe the various process of interest for an understanding of the atmospheric density profile. The 'continuity equation' is

$$\frac{\partial n_i}{\partial t} + \nabla.(n_i \boldsymbol{u}_i) = P_i - L_i \tag{1.1}$$

Here n_i = ion number density; $\boldsymbol{u}_i$ = mean velocity of ion; P_i and L_i are the chemical production and loss terms respectively. In one dimension along the magnetic field the ions and the electrons momentum equations can be written as *(Schunk & Nagy, 2000),*

$$\nabla_{\parallel} p_i + (\nabla.\boldsymbol{\tau_i})_{\parallel} - n_i e\boldsymbol{E}_{\parallel} - n_i m_i \boldsymbol{G}_{\parallel} = n_i m_i \nu_{ie}(\boldsymbol{u}_e - \boldsymbol{u}_i)_{\parallel} + n_i\, m_i\, \nu_{in}\, (\boldsymbol{u}_n - \boldsymbol{u}_i)_{\parallel} \tag{1.2}$$

$$\nabla_{\parallel}\ p_e + (\nabla.\boldsymbol{\tau_e})_{\parallel} + n_e e\boldsymbol{E}_{\parallel} - n_e m_e\, \boldsymbol{G}_{\parallel} = n_e m_e \nu_{ei}(\boldsymbol{u_i} - \boldsymbol{u}_e)_{\parallel} + n_e m_e \nu_{en}(\boldsymbol{u}_n - \boldsymbol{u}_e\ )_{\parallel} \tag{1.3}$$

where the subscripts *i, e* and *n* are for ions, electrons and neutrals respectively, $\boldsymbol{u}$ is the velocity, $\boldsymbol{\tau}$ is the stress tensor, p is the pressure, m is the mass, ν is the collision frequency and $\mathbf{E}_{\parallel}$ is the polarization electrostatic field caused by charge separation. Note that $n_e \nu_{ei} m_e = n_i\, \nu_{ie} m_i$. Considering $n_e = n_i, \nu_{i\boldsymbol{n}} \cong \nu_{en}$ and using the fact that $m_e \ll m_i$, after adding both equations *(Schunk & Nagy, 2000),* we obtain

$$\nabla_{\parallel}(p_i + p_e) + (\nabla.\boldsymbol{\tau_i})_{\parallel} + (\nabla.\boldsymbol{\tau_e})_{\parallel} - n_i m_i \boldsymbol{G}_{\parallel} = n_i\ m_i\, \nu_{in}\, (\boldsymbol{u}_n - \boldsymbol{u}_i)_{\parallel} \tag{1.4}$$

Now considering the ideal gas equation for ions and electrons, we can write $p_i = n_i k T_i$ and $p_e = n_e k T_e$. So equation (1.3) becomes

$$\nabla_{\parallel}(n_i\, kT_i + n_e\, kT_e) + (\nabla.\boldsymbol{\tau_i})_{\parallel} - n_i m_i \boldsymbol{G}_{\parallel} = n_i\, m_i\, \nu_{in}(\boldsymbol{u}_n - \boldsymbol{u}_i)_{\parallel} + (\nabla.\boldsymbol{\tau_e})_{\parallel} \quad (1.5)$$

The $\nabla.\boldsymbol{\tau}_{i,e}$ terms are associated with strongly non-Maxwellian velocity distributions and are therefore normally neglected. Also T_i and T_e are often considered uniform, resulting in the ambipolar diffusion equation *(Schunk & Nagy, 2000)*

$$\boldsymbol{u_{i\parallel}} = \boldsymbol{u_{n\parallel}} - D_a\left[\frac{1}{n_i}\nabla_{\parallel} n_i + \frac{1}{T_p}\nabla_{\parallel} T_p - \frac{m_i \boldsymbol{G}_{\parallel}}{2kT_p}\right] \quad (1.6)$$

Here, D_a is the ambipolar diffusion and T_p is the plasma Temperature.

$$D_a = \frac{2kT_p}{m_i \nu_{in}} \quad (1.7a)$$

$$T_p = \frac{(T_e + T_i)}{2} \quad (1.7b)$$

Here we can see that $D_a \propto 1/\nu_{in}$ and note that, $\nu_{in} \propto n_n$. So $D_a \propto 1/n_n$. Therefore, D_a increases exponentially with altitude because the neutral density decreases exponentially with altitude *(Schunk & Nagy, 2000)*. It is difficult to turn O^+ to NO^+ above 250 km because $[N_2]$ is small and molecular diffusion is rapid higher up. Therefore, O^+ reaches a peak around 250 km where diffusion removes the O^+ ions formed by photoionization. This means that the topside F-region density is controlled by diffusion.

Above the peak in a steady equilibrium situation, we can consider $\boldsymbol{u}_{i\parallel} = \boldsymbol{u}_{n\parallel} = 0$**,** so that the solution to equation (1.6) will be

$$n_i(z) = n_i(0)e^{-z/H_p} \quad (1.8)$$

where $H_p = \frac{2kT_p}{m_i g}$.

By contrast, the E and F1 regions are known as "Chapman layers" because they are produced by photochemistry and do not involve diffusion *(Aikio & Nygen, 2008)*.

1.2.2.1 Ionization:

Photoionization and collisional ionization are two processes which produce ionospheric ionization.

Photoionization: In photoionization, neutral particles are ionized by EUV radiation.

$$O + h\nu \overset{q_1}{\rightarrow} O^+ + e$$

$$N_2 + h\nu \overset{q_2}{\rightarrow} N_2^+ + e$$

$$O_2 + h\nu \overset{q_3}{\rightarrow} O_2^+ + e$$

Here q is the photoionization rate. If we consider an isothermal atmosphere, the scale height H_n of neutral gas would be,

$$H_n = \frac{KT_n}{m_n g} \qquad (1.9)$$

The Chapman production function is used to discuss the basic electron and ion production rates. During the day, the ionizing radiation intensity varies with the elevation angle of the Sun and the electron density responds to the energy radiation *(Hargreaves & Hunsucker, 2003)*. The basic Chapman theory assumes that *(Aikio & Nygen, 2008)*,

i) The atmosphere is isothermal and obeys the hydrostatic equation so that the scale height H_n is independent of altitude.

ii) Each neutral species can be considered separately.

iii) The absorption cross section is constant (monochromatic radiation)

The Chapman production function can be expressed as *(Baumjohann & Treumann, 1996)*

$$q(\chi, h) = q_m exp[1 - h - \frac{1}{Cos\chi} e^{-h}] \quad (1.10)$$

where $q(\chi, h) =$ production (ionization) rate at the reduced height and $h = \int_{z_0}^{z} \frac{dz}{H} = \frac{z - z_0}{H}$ where z_0 is the altitude at which τ =1. Also, χ is the solar zenith angle, $q_m = \frac{\eta I_\infty}{eH}$ is the peak production rate, τ is the optical depth and η is the efficiency of the photo production reaction. The production rate reaches a maximum when the solar zenith angle is $\chi = 0$.

Figure 1.4 shows the Chapman production profile for different zenith angles.

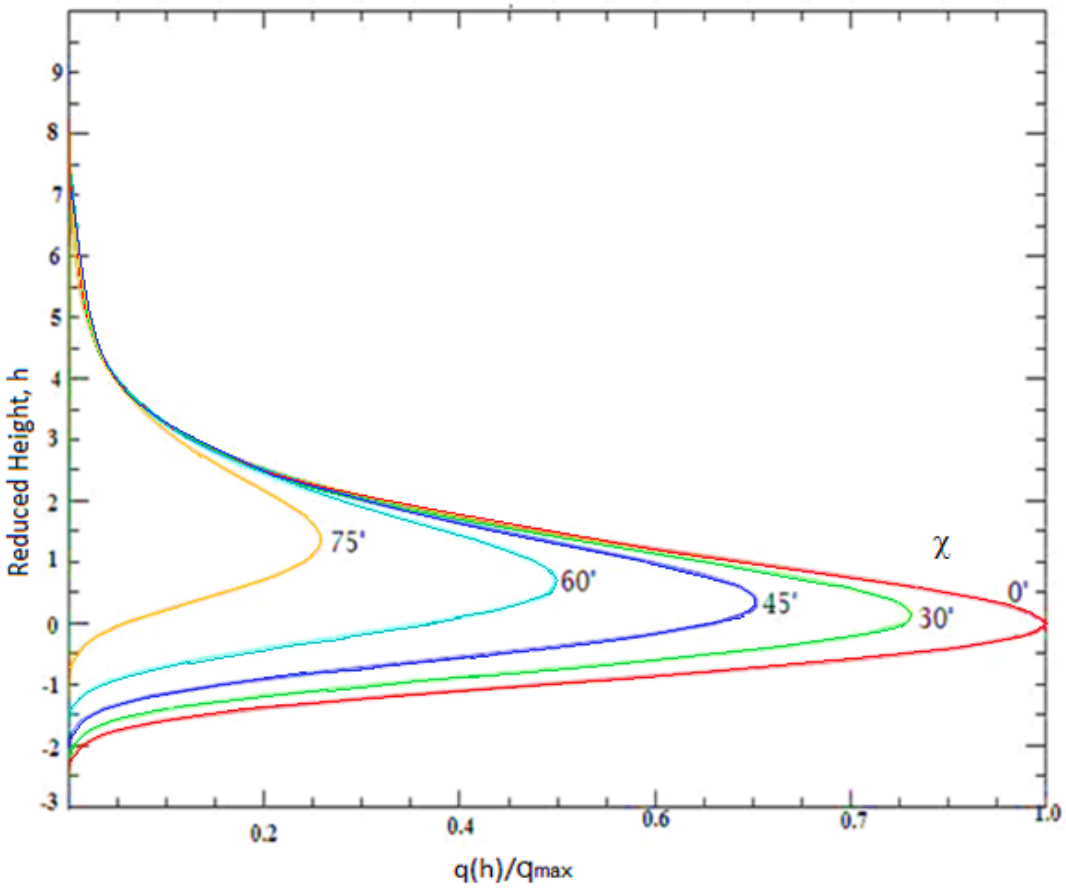

Figure 1.4: Chapman production profile for different zenith angles

1.2.2.2 Chemical Reactions:

We already have mentioned the production of the plasma. Here the loss processes will be discussed. The main neutralizing reactions are interchange reaction, charge transfer and recombination.

Interchange Reactions**:** In the interchange reactions, molecules interchange their atoms.

$$O^+ + N_2 \overset{k_1}{\rightarrow} NO^+ + N$$

$$N_2^+ + O \overset{k_2}{\rightarrow} NO^+ + N$$

Charge Transfer: In charged transfer processes, an electron from a neutral can transfer to an ion.

$$H + O^+ \rightarrow O + H^+$$

$$O^+ + N_2 \overset{k_3}{\rightarrow} N_2^+ + O$$

$$O_2 + O^+ \rightarrow O_2^+ + O$$

Recombination: During the ionization process, ions and electrons are produced continuously but by recombination they produce neutral atoms or molecules. The loss rate depends on the electron/ion densities and the rate coefficients of the recombination process *(Aikio & Nygen, 2008)*. Dissociative recombination and radiative recombination are two different recombination processes. For typical ionospheric densities, the coefficient of the dissociative recombination is the order of $10^{-13}\ m^3 s^{-1}$ whereas for the radiative recombination it is $10^{-18} m^3 s^{-1}$. From the coefficient it is clear that radiative recombination is much slower than dissociative recombination.

Dissociative Recombination: $\mathrm{N}_2^+ + e \overset{k_4}{\rightarrow} N + N$

$$NO^+ + e \xrightarrow{k_5} N + O$$

$$O_2^+ + e \xrightarrow{k_6} O + O$$

Radiative Recombination: $O^+ + e \rightarrow h\nu + O$

The $N_2^+ + O$ reaction is so frequent that we can neglect the $N_2^+ + e$ reactions. Here as an example we can consider the chemistry of NO^+. According to the basic first order reaction schemes

$$p(NO^+) = [O^+]k_1\,[N_2] + k_2\,[O][N_2^+] \tag{1.11}$$

$$l(NO+) = k_5[NO^+]([NO^+] + [O^+]) \tag{1.12}$$

NO^+ satisfies a quadratic equation. Therefore, we have

$$k_5[NO^+]^2 + k_5[NO^+][O^+] = k_1[N_2][O^+] + k_2[O][N_2^+] \tag{1.13}$$

Now adding the N_2^+ and O^+ chemistry

$$[N_2^+] = \frac{[N_2]q_2^*}{k_2[O]} \tag{1.14}$$

$$[O^+] = \frac{[O]q_1^*}{k_1[N_2]} \tag{1.15}$$

Here $q_1^* = q_1/n$ and $q_2^* = q2/n$ are the normalized photo production rates listed at the beginning of section 1.2.2.1. As a result,

$$k_5[NO^+]^2 + k_5[NO^+]\frac{[O]q_1^*}{k_1\,[N_2]} = \frac{k_1[N_2]([O]q_1^*)}{k_1\,[N_2]} + k_2\frac{[O]([N_2]q_2^*)}{k_2\,[O]} = q_1 + q_2 \tag{1.16}$$

With the $\frac{[O]}{[N_2]}$ ratio being small in the below 200 km, we then obtain .

$$[NO^+] \approx n_e = \sqrt{\frac{q_1 + q_2}{k_5}} \tag{1.17}$$

Finally with q_2 peaking near 120 km, $[NO^+]$ is found to peak around 120 km.

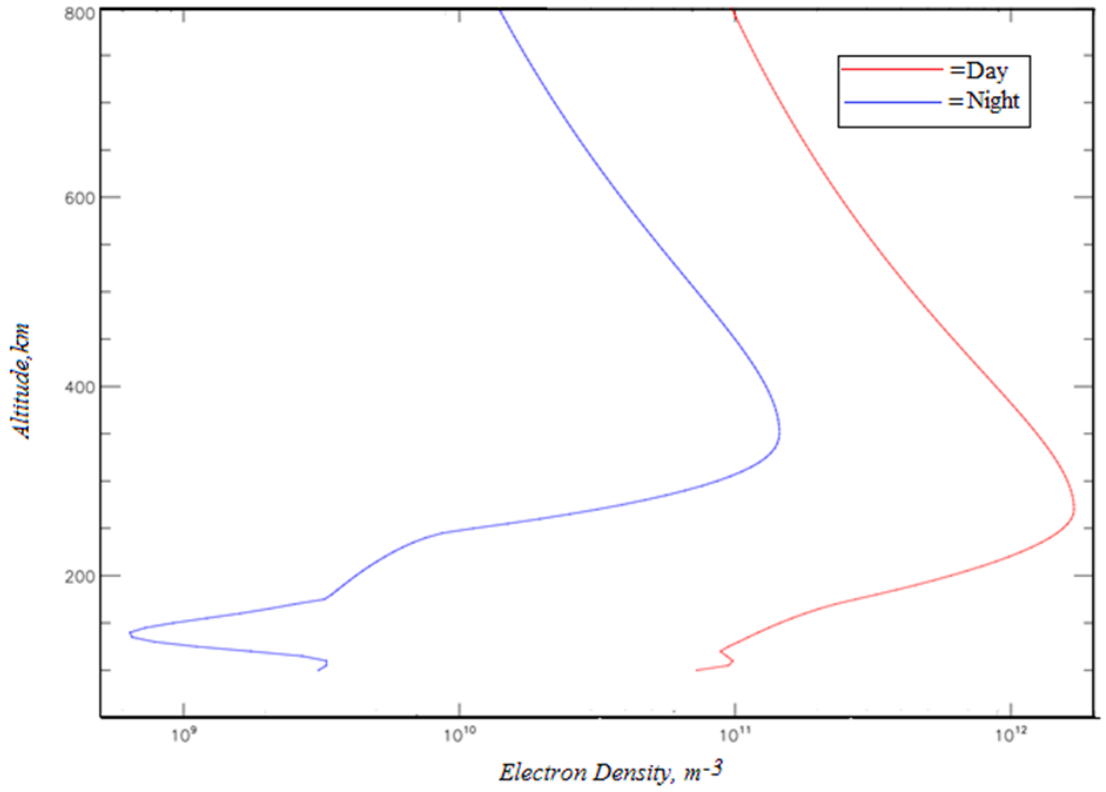

Figure: 1.5 Schematic day and night density profile of the ionosphere. LT 12 hours for day and 24 hours for night on 14th September 2000, Geographic Latitude=50 (Profile obtained from the IRI model)

Note that the $[O^+]$ production rate peaks around 150 km. However $[O^+]$ increases with height because the ratio $[O]/[N_2]$ becomes high (see equation 1.16). This increase stops at 250 km because diffusion becomes faster higher up.

From the density profile of Figure 1.5, we get a clear picture the O^+ and NO^+. At 120 km the peak is the result of NO^+ and known as the 'E-peak', whereas, at 250 km O^+ dominates and is known as the 'F-peak'.

1.2.2.3 Collisional Ionization or Ionization by Energy Particles:

Particle precipitation is also a source of ionization at high latitude and causes variations in the composition and electron density. When the charged particles precipitate from the magnetosphere into the Earth's ionosphere they collide with atoms and molecules, and ionize them. For example, we can have

$$O + e \rightarrow O^+ + 2e$$

Figure 1.6 shows an ionization profile due to precipitation. Electrons that are more energetic penetrate deeper into the ionosphere and a largest fraction of electron-ion pairs can be produced by collision *(Baumjohann & Treumann, 1996)*. Secondary ion-electron pairs are produced for every 35 eV loss of the initial energy *(Kelley, 2012)*. Different satellite measurements show that the energy range of the auroral precipitating energy flux is 1 to 10 keV. Figure 1.6 shows that electrons of 1 keV energy are stopped above 150 km altitude whereas 300 keV electrons penetrate down to 70 km *(Baumjohann & Treumann, 1996)*.

Ionization by energetic particles dominates in the auroral zone at night when photoionization becomes negligible *(Baumjohann & Treumann, 1996)*.

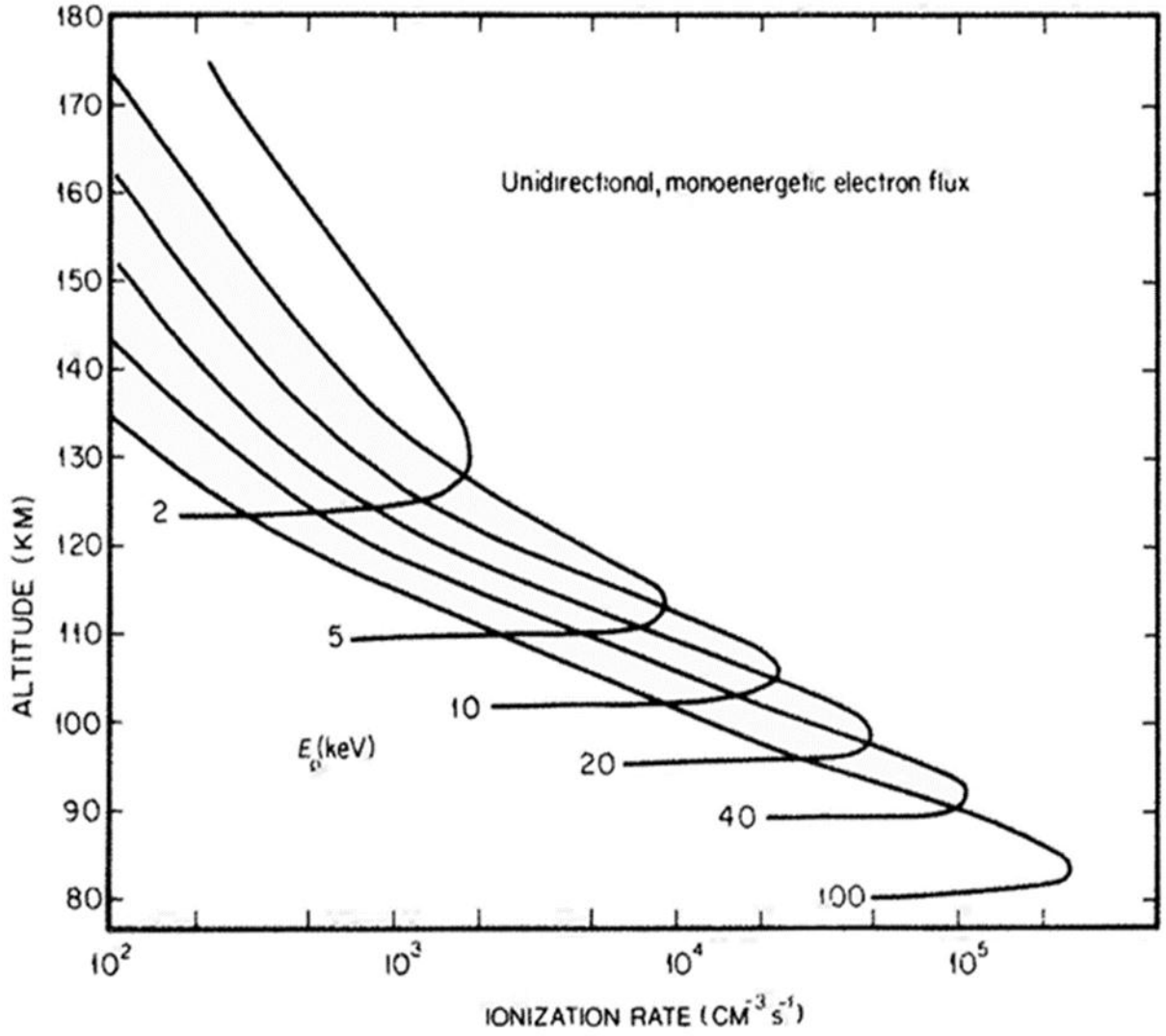

Figure 1.6: Profiles of the rate of ionization due to energy particles precipitating along magnetic field line *(Rees, 1989)*

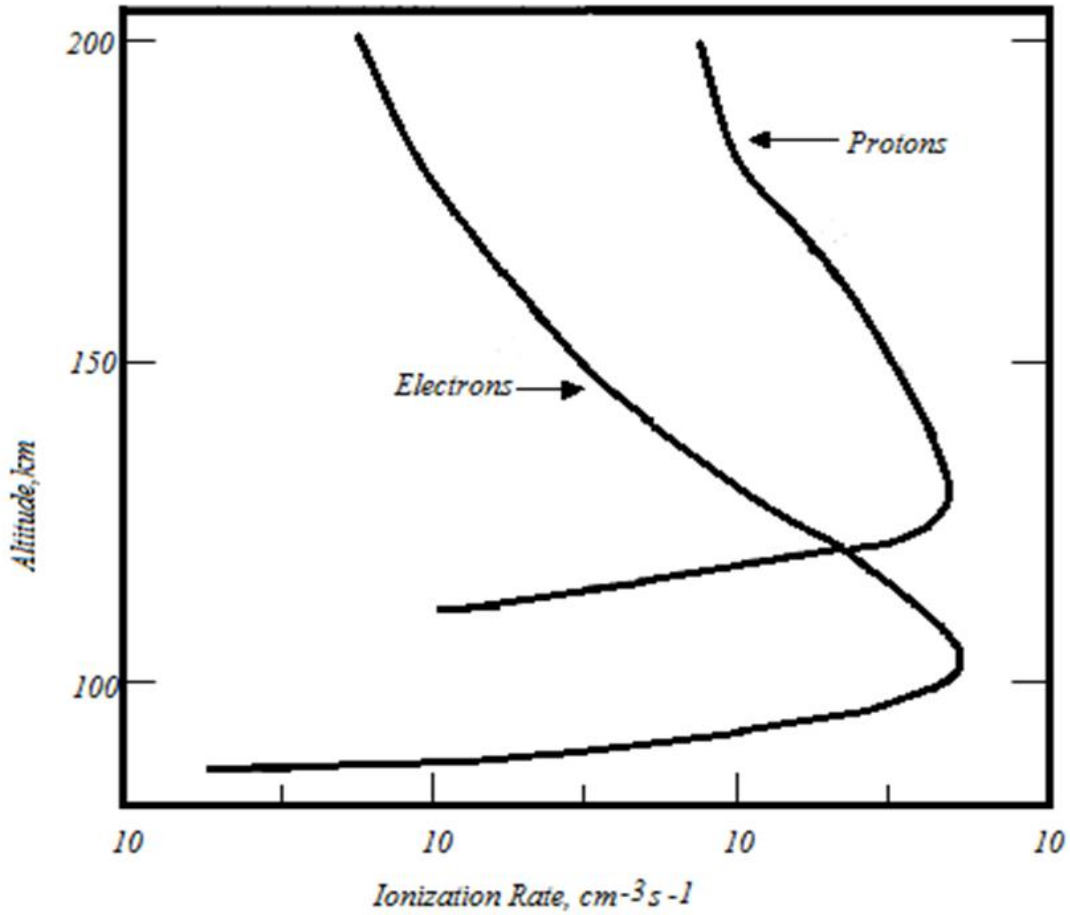

Figure 1.7: Ionization profile due to precipitating protons and electrons computed from rocket observations *(Baumjohann & Treumann, 1996)*

In Figure 1.7, it is indicated that because of lower ionization efficiency, same energy ions are stopped at greater heights than electrons and above 100 km electrons are responsible for ionization whereas above 130 km precipitating ions contribute more to the collisional ionization *(Baumjohann & Treumann, 1996).*

1.2.3 Temperature

Four sources of heat control the ionospheric temperature. These are *(Hargreaves & Hunsucker, 2003)*

a) Photo dissociation, ionization and consequent reactions via absorbing solar UV and X-ray radiation.
b) Precipitation of the energetic particles on the ionosphere from the magnetosphere.
c) Joule heating by ionospheric currents
d) Dissipation of tidal motions and gravity waves by turbulence and molecular viscosity.

Between 90-250 km the O_2, N_2 and O gases absorb the shorter wavelength electromagnetic ultraviolet (EUV) radiation. As discussed above, EUV radiation and X-ray are able to ionize the gases which ultimately increases the ionospheric temperature. At high latitude during storms at 100-130 km auroral electrons and at 115-130 km Joule heating by electric currents are the main sources of heat for the upper atmosphere *(Hargreaves & Hunsucker, 2003).*

Ionospheric electrons can be heated by photoelectrons. Energy is also given off when molecular ions recombine with electrons. At high altitude, photoelectrons transfer energy to thermal electrons and along magnetic field lines, this energy is conducted down *(Schunk & Nagy, 2000)*. In collisional processes, ions get energy from heat exchange with neutrals, and higher up, with thermal electrons. Figure 1.8 represents the profiles of electron, ion and neutral temperature at night-time. During the daytime below 300 km altitude, T_e is associated with photoelectron heating and above 300 km altitude thermal conduction dominates the T_e profile *(Schunk & Nagy, 2000)*. With increasing altitude, the ion temperature increases because of collisions between ions and hotter electrons.

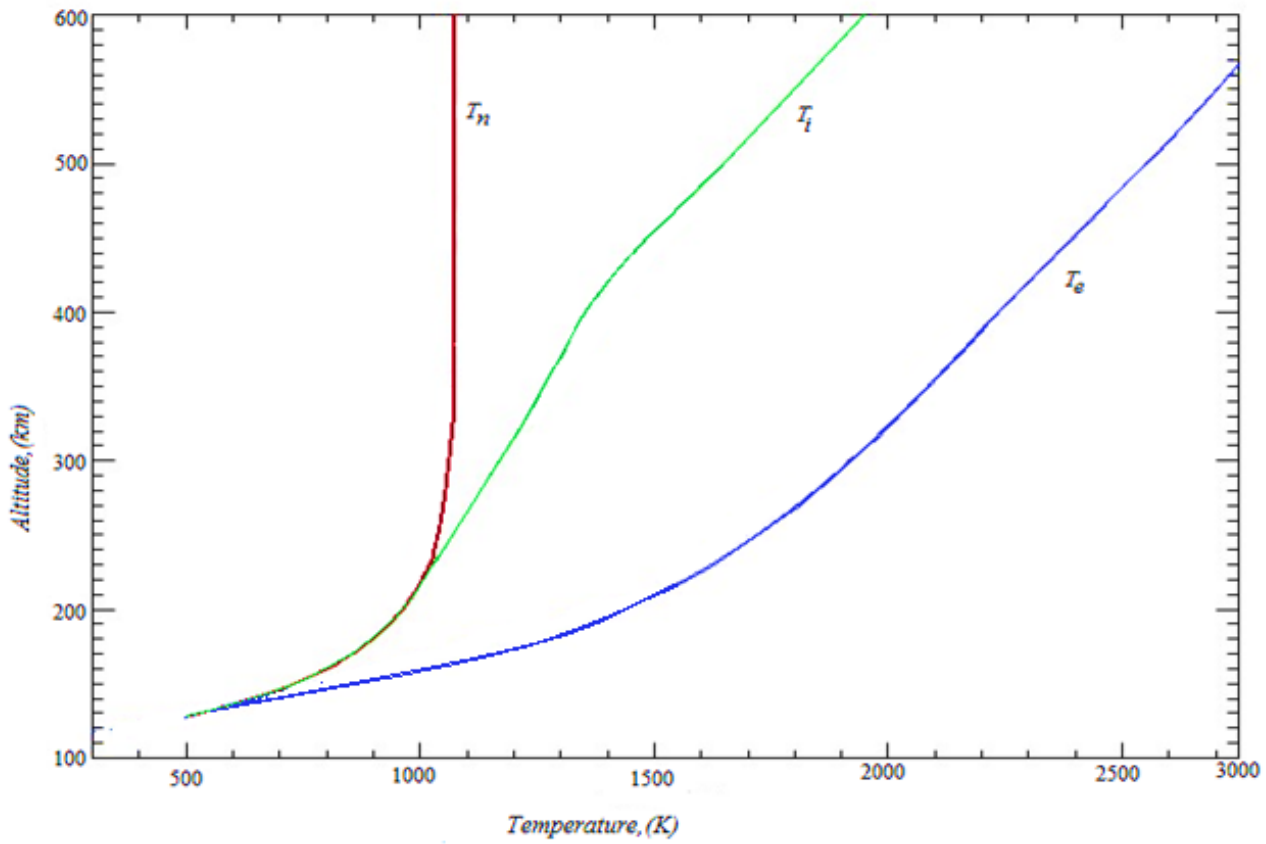

Figure 1.8: Profile of electrons, ions and neutrals temperature within UT 1.5 hours on 14th September 2000, Geographic Latitude=70 according to U.S. standard atmosphere, 1976.

Frictional heating due to collisions with neutrals and other species is very significant for ion heating in the presence of large drifts between ions and neutrals *(Schunk & Nagy, 2000)*. Heat exchange between the ion and neutrals help to balance the frictional heating in the ions in that case. *St.-Maurice & Hanson (1982)* showed that when the DC electric field is 20mV/m or more, heat exchange with the neutral gas is balanced by frictional heating, namely, $|\boldsymbol{V_i} - \boldsymbol{V}_n|$ is large enough to produce a large increase in T_i above T_n.

The general form of the ion energy equation is *(St.-Maurice & Hanson, 1982)*

$$\frac{D}{Dt}\left(\frac{3}{2}p_i\right)+\frac{5}{2}\,p_i(\boldsymbol{\nabla}.\boldsymbol{V}_i)+\nabla.\boldsymbol{q_i}+\boldsymbol{\tau_i}:\nabla\boldsymbol{V}_i$$

$$=\sum_n\frac{n_i m_i \nu_{in}}{m_i+m_n}\{3k_b(T_n-T_i)\psi_{in}+m_n(\boldsymbol{V_i}-\boldsymbol{V_n})^2\phi_{in}\}$$

$$+n_i\nu_{ie}3k_b(T_e-T_i)+n_i\nu_{ie}m_e(\boldsymbol{V_i}-\boldsymbol{V_e})^2 \qquad (1.16)$$

where $\frac{D}{Dt}=\frac{\partial}{\partial t}+\boldsymbol{V_i}.\nabla$ is a convective derivative, p_i is the ion pressure, $\boldsymbol{V_i}, \boldsymbol{V_e}$ and $\boldsymbol{V_n}$ ion electron and neutral drift velocities respectively, $\boldsymbol{\tau_i}$ is the stress tensor, $\boldsymbol{q_i}$ is the ion heat flow, n_i the ion density, m_i, m_e and m_n are the ion, electron and neutral masses respectively, $\nu_{in}$and ν_{ie} are ion-neutral and ion-electron collision frequencies, k_b is the Boltzmann constant, and ψ_{in} and ϕ_{in} are 1 to a first approximation. Also $\boldsymbol{\tau}_i:\nabla\boldsymbol{V}_i=\sum_{l,m}\boldsymbol{\tau}_{lm}\frac{\partial \boldsymbol{V}_l}{\partial x_m}$. If we consider the left hand side terms we have: 1) rate of change of energy per unit volume, 2) cooling (heating) due to pressure change, 3) divergence of the ion heat flow, 4) viscous heating due to stress. Considering the right hand side terms we have: 1) heat exchange between ions and neutrals, 2) frictional heating of ion and neutrals, 3) heat exchange between ions and electrons, 4) frictional heating of ion and electrons.

When there is an electric field, equation (1.16) can be reduced. Time derivative $(\partial/\partial t)$ can be neglected for events where time scale longer than $1/\nu_{in}$ *(Schunk, 1975).* Since the ion drift is incompressible $\nabla.\boldsymbol{V_i}=0$ *(Rishbeth & Hanson, 1974).* *Schunk and Sojka* (1982) presented that below 400 km the effect of heat advection $\boldsymbol{V_i}.\nabla p_i$ and conduction $\nabla.\boldsymbol{q_i}$ on the ion energy balance is negligible. The viscous heating $\boldsymbol{\tau_i}:\nabla\boldsymbol{V_i}$ has a negligibly small affect on the F-region *(Schunk, 1975).* In the F-region $(\boldsymbol{V_i}-\boldsymbol{V}_e)$ terms can be neglected *(St.-Maurice & Hanson, 1982*). So now, equation (1.16) becomes

$$0 = \frac{n_i\, m_i\, \nu_{in}}{m_i + m_n}\{3k_b\,(T_n - T_i\,) + m_n\,(\boldsymbol{V_i} - \boldsymbol{V_n}\,)^2\,\} + n_i\,\nu_{ie}\,3k_b\,(T_e - T_i\,) \qquad (1.17)$$

Or,

$$3k_b\ (T_i - T_n\ ) \cong m_n\ (\boldsymbol{V_i} - \boldsymbol{V_n})^2\ + \frac{m_i + m_n}{m_i}\frac{\nu_{ie}}{\nu_{in}}\ 3k_b(T_e - T_i) \qquad (1.18)$$

In equation (1.18) the left-hand-side term represents heat exchange with neutrals, whereas in the right hand side 1st term is frictional heating and the 2nd term is heat exchange with electrons. When the electric field is zero then there is no friction between ions and neutrals. The heat exchange with electrons plays a secondary role below 400 km, that is, frictional heating with neutrals and cooling with heat exchange with neutrals dominate. Heat exchange with electrons can be neglected entirely when the electric field is more than 20 mV/m. Therefore, the net result from equation (1.18) in the presence of a strong electric field is,

$$T_i = T_n + \frac{m_n}{3k_b}\ (\boldsymbol{V}_i - \boldsymbol{V}_n)^2 \qquad (1.19)$$

In terms of the effective electric field the ion temperature becomes *(St.-Maurice, et al., 1999)*

$$T_i = T_n + \frac{m_n}{3k_b}\frac{\left(\frac{\boldsymbol{E}'}{B}\right)^2}{1 + \alpha_i^2} \qquad (1.20)$$

where $\boldsymbol{E}' = \boldsymbol{E} + \boldsymbol{V_n} \times \boldsymbol{B}$, and $\boldsymbol{E}'$ is the electric field perpendicular to the magnetic field, $\boldsymbol{B}$. Also $\alpha_i = \frac{\nu_i}{\Omega_i}$ is the ion collision to cyclotron frequency ratio. Equation (1.20) shows that electric field is the key driver for the frictional heating. At higher altitude (above 150 km) the collision frequency is small and all charged particles move at the $\boldsymbol{E} \times \boldsymbol{B}$ drift. The ratio of the electrons and ions heating rates is approximately proportional to the electrons and ions mass ratio, and therefore

preferably the ions are heated by the electric field through collisions with neutrals *(Schunk & Nagy, 1978).* Below 400 km altitude when electric field is zero then ion temperature is equal to neutral temperature but when electric field is say for 100 mV/m ion temperature is enhanced at all heights *(Schunk & Nagy, 2000).*

Ionizing photons carry more energy than required for photoionization. Photoelectrons are lighter than photo-ions, so they can acquire most of the extra energy and during photoionization their initial energies are typically some tens of electron volts *(Schunk & Nagy, 1978).* However, equation (1.18) is also applicable for electrons. Because of frictional heating, electrons can be heated. The electrons can also be heated indirectly through the elastic collision with hot ions *(Schunk & Nagy, 1978)*. If frictional heating was to balance the elastic cooling with neutrals for electrons, T_e would react to electric fields with much the same temperature as the ions. However, frictional heating does not influence electrons strongly because inelastic collisions are much more important than elastic collisions in cooling the electrons. Cooling rate due to elastic collisions is negligible for electrons, the cooling due to inelastic collision being roughly 150 times larger than cooling through elastic collisions.

Schunk and Nagy (1978) discussed various electron cooling rates processes. These involve rotational and vibrational excitation of N_2 and O_2, fine structure excitation of O, electronic excitation of $O, N, N_2,$ and O_2, elastic collisions with the neutrals and Coulomb collision with ambient ions. In the lower altitude ionosphere, dominant cooling processes for the electrons are the fine structure excitation of atomic oxygen and rotational and vibrational excitation of N_2 and O_2 *(Schunk & Nagy, 2000).*

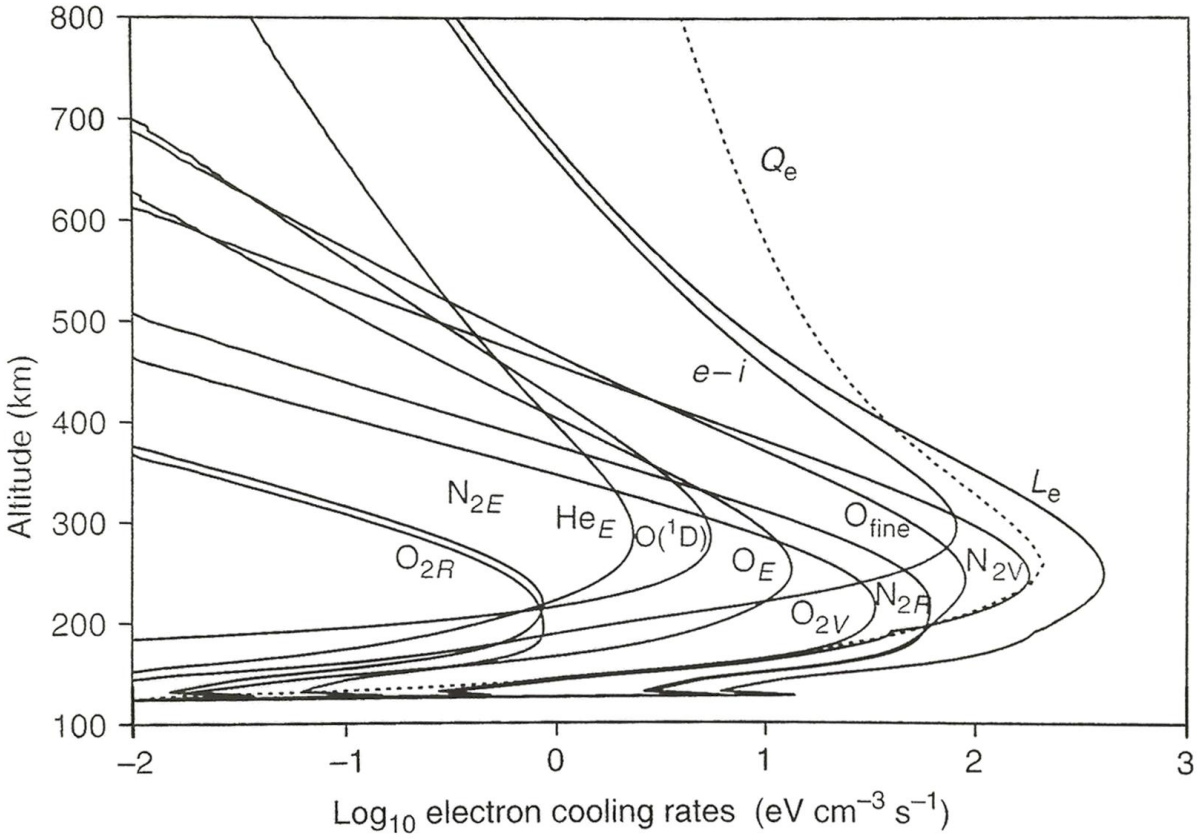

Figure 1.9: Electron cooling rate as a function of altitude in the daytime. Subscripts R, V and E represent cooling rates associated with rotational, vibrational and elastic collisions, respectively. $O(^1D)$ is loss due to excitation of O to the (^1D) state, and that labeled O(^3P) represents the losses due to the excitation of fine structure levels in O. The curve labeled e-I represents the losses in Coulomb collisions between electrons and ions (*Schunk & Nagy, 2000*).

Figure 1.9 shows the comparison of the electron cooling rates at mid-latitudes in the daytime. Here, L_e is the energy loss rate of electron and Q_e represent the total electron heating rate. During the daytime, below 220 km dominating cooling process is fine structure excitation of atomic oxygen whereas above 220 km Coulomb interactions with the ambient ions dominate *(Schunk & Nagy, 2000).*

1.3 Magnetospheric Driver

Before discussing the details of the ionospheric electrons heating by electric fields, it is important to discuss the solar system characteristics and interactions between the solar wind and the magnetosphere. Planetary systems that possess an ionosphere and electric-magnetic environments are the reason for the dynamical processes acting within and on the ionosphere *(Schunk & Nagy, 2000).*

1.3.1 Solar Wind

The Solar Wind is an outflow of plasma from the solar corona and contains a remnant of solar magnetic field that pervades interplanetary space *(Kivelson & Russell, 2005).* The solar wind outflow starts in the lower corona and as the plasma moves away from the Sun, the velocity increases steadily *(Schunk & Nagy, 2000).* The solar wind is a mixture of 95% protons (H^+) and 5% of α-particles (He^{2+}). Typical values of the solar wind parameters are: a flow speed of $350\ \mathrm{kms}^{-1}$, a magnetic field of 5×10^{-9} tesla and proton and electron temperatures of respectively 4×10^4 K and 1.5×10^5 K. At a distance of 10- 20 Earth radii, the solar wind becomes supersonic and collisionless. The solar magnetic field that resembles a dipole near the Sun gets 'frozen' into the solar wind and is carried by it into space, becoming the interplanetary magnetic field (IMF) *(Schunk & Nagy, 2000).*

1.3.2 Magnetospheric Interaction and Reconnection

The magnetosphere is the region above the ionosphere where the motion of a charged particle is controlled by the Earth's magnetic field *(McFadden, et al., 2006)*. The shape of the magnetosphere is the result of the interaction between the Earth's magnetic field and the solar wind. Earth's magnetic field is considered as a dipole tilted $11^{\circ} - 12^{\circ}$ away from the axis of rotation. In this layer, the Earth's magnetic field traps high-energy charged particles which drift around the Earth.

The earth magnetic field and the magnetosphere act as an obstacle when the solar wind comes towards the Earth. On the dayside, the electrically charged particles interact with the magnetosphere and a bow shock is formed where the supersonic flow turns into the subsonic flow and applies a tangential stress on the magnetopause boundary. The region between the shock front and the magnetopause (which envelops the magnetosphere) is the magnetosheath *(Hargreaves & Hunsucker, 2003).*

The magnetic field of the Earth's surface is dipole. Because of that, the magnetic force of the Earth deflects solar wind ions to the right and electrons to the left as they move antisunward. The magnetopause reconnection entrains magnetic flux from the dayside and adds it to the night side. As a result, the magnetosphere is compressed at the dayside and the field dragged into a comet like tail at the night side (Figure 1.10). Hence we see that the dayside magnetosphere 'magnetopause' is about ten Earth radii and at the night side it is about 40-60 Earth radii.

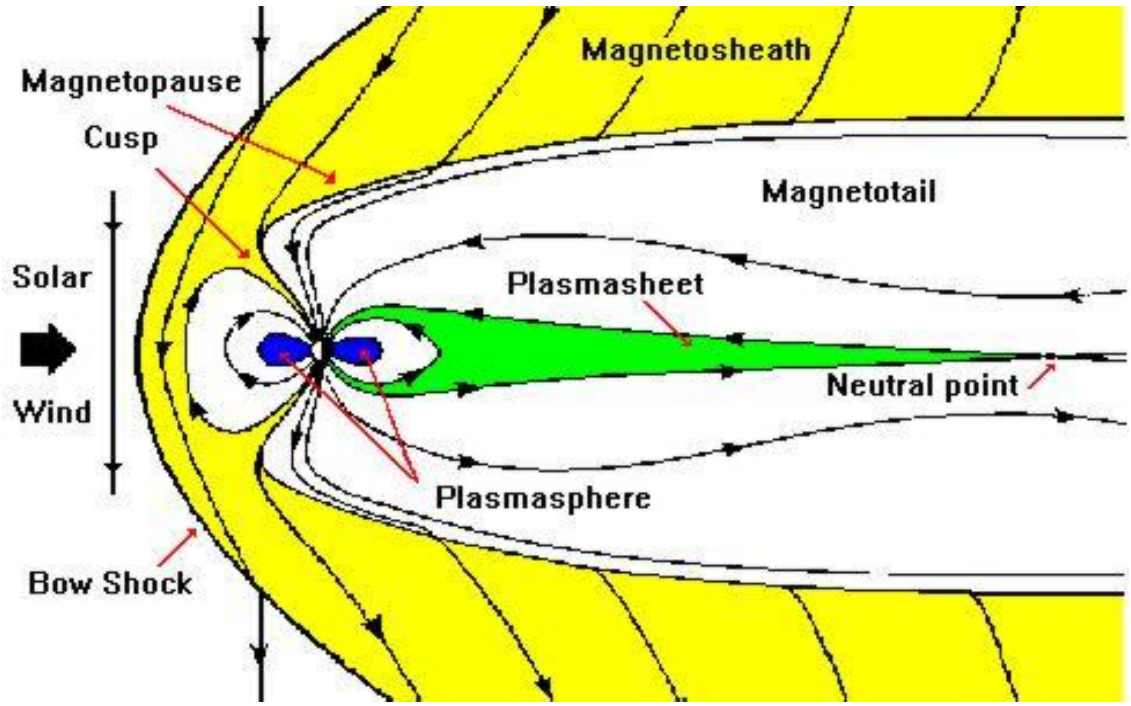

Figure 1.10: Space Environment after interaction between the Solar Wind and the Earth magnetosphere *(Christian R. E., 2012)*

In the case of a southward interplanetary magnetic field, the convection of the ionized plasma is driven by reconnection *(Dungey, 1961)*. A southward interplanetary magnetic field creates an anti-parallel reconnection at the dayside magnetosphere when the solar wind encounters the magnetopause (marked as line-1 in Figure 1.11). The merged field lines will split into two open field lines, each of which connect to the Earth and the other end stretching out into the solar wind (marked as line-2 in Figure 1.11) *(Baumjohann & Treumann, 1996)*. Solar wind particles can travel along magnetic field lines and deposit their energy in the upper atmosphere *(Schunk & Nagy, 2000)*. When the magnetic field of the solar wind and the Earth are oppositely directed, two neutral points are produced. One is in the dayside where solar wind interacts with the earth's magnetic field (denoted as point n_1 in Figure 1.11) and the other is in a compressed field line region in the magneto tail (denoted as point n_2 Figure 1.11). The solar wind particles, along with plasma that

has escaped the Earth's upper atmosphere and has convected to the tail populating a region known as plasma sheet *(Schunk & Nagy, 2000)*. The field line is transported to the down-tail across the polar cap due to the solar wind and the magnetospheric field lines also get transported down-tail (marked as line 3-5 in Figure 1.11) *(Baumjohann & Treumann, 1996)*. To maintain a steady state, reconnection must occur on the night side at the second neutral

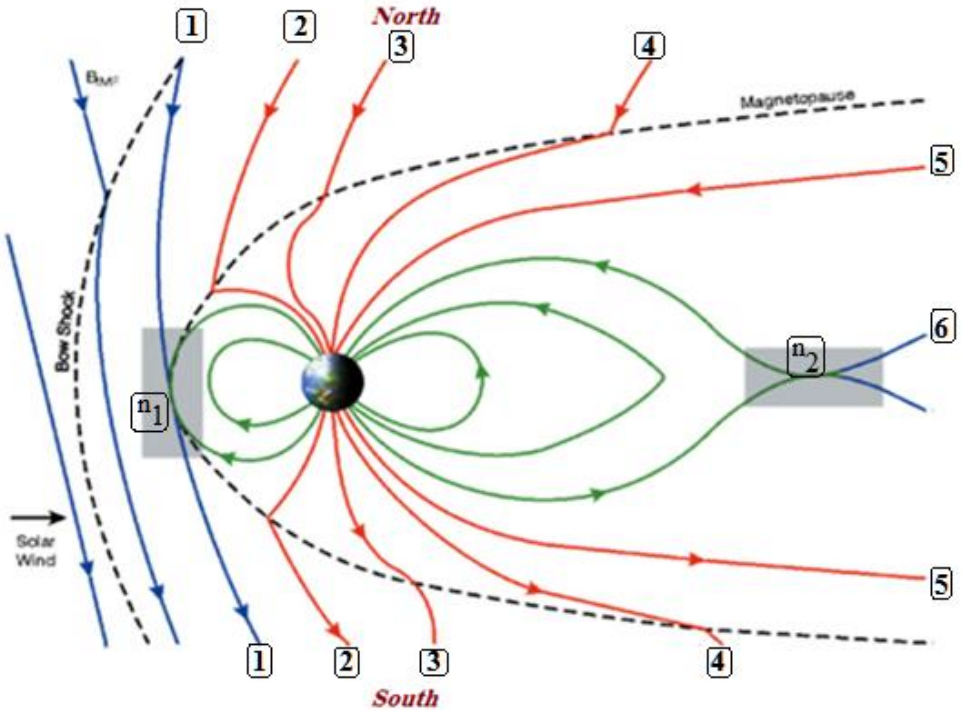

Figure 1.11: Southward Solar Wind and geomagnetic filed line merging and reconnection at the magnetopause *(Lapenta G., 2014)*

point n_2 . Under the equilibrium conditions, the field lines will eventually be brought back to the front side magnetosphere and the same cycle can be repeated *(Baumjohann & Treumann, 1996)*.

The circulation of the plasma over the surface of the Earth is driven by the magnetic reconnection of the magnetosphere. From the perspective of the Earth the circulation is an $\boldsymbol{E} \times \boldsymbol{B}$. Because the solar wind is highly conductive, interplanetary magnetic field is carried with the velocity of the solar wind that can create an electric field *(Aikio & Nygen, 2008)*. The electric.

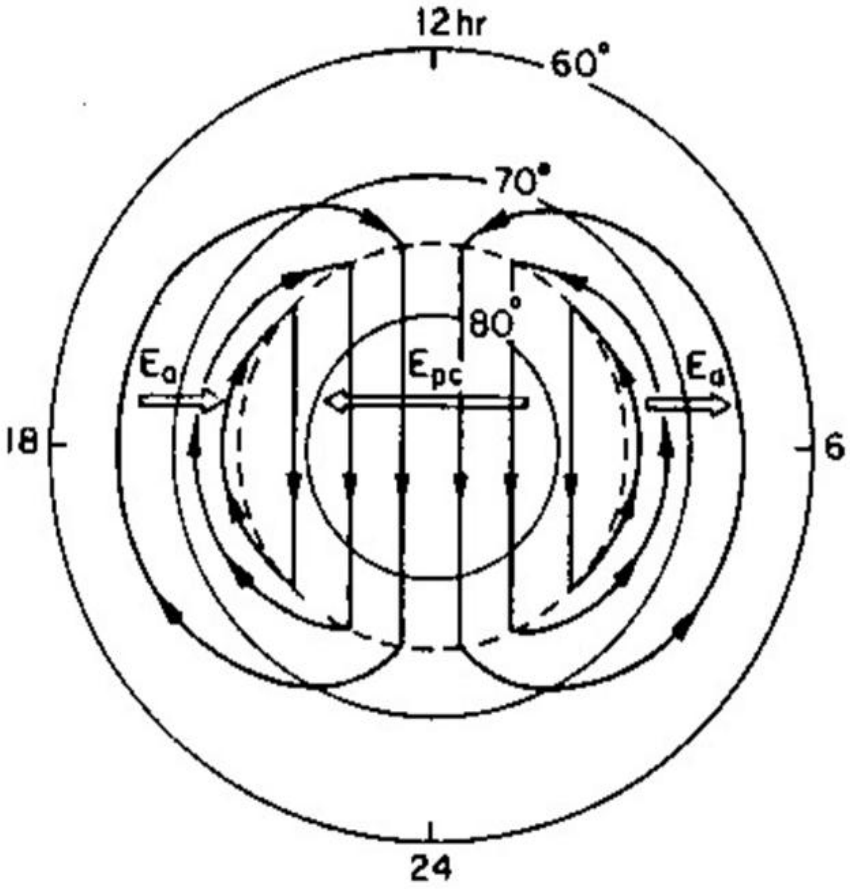

Figure 1.12: Convection pattern of ionospheric plasma flow due to electric field at Northern high latitude *(Kelley, 2012)*.

field dynamo produces a two-cell convection pattern with an antisunward plasma flow over the polar cap.

A returning sunward flow takes place at latitudes corresponding roughly to the auroral oval *(Schunk & Nagy, 2000).* That flow is caused by a convection electric field ($\mathbf{E}_a$) (Figure 1.12) *(Kelley, 2012).* The convection electric field ($\mathbf{E}_a$**)** can causes strong currents at high latitude. These currents will be discussed in another chapter.

The two-cell convection pattern which can be intense, particularly around the auroral regions, maps into the E region. Under very disturbed condition, the corresponding electric field perpendicular to magnetic field can reach a magnitude of more than 100 mV/m (2 km/s plasma drifts).

1.5 Anomalous Electron Heating in the E-region

At the beginning of the 1980's, improvement in radar technology allowed researchers to study the E-region in some detail. In the process, they found an E-region electron temperature enhancement at times, which ended up being correlated with the ambient electric field.

Rees and Walker (1968) in their theoretical work considered a typical auroral ion and electron temperature profile and two electric fields 10 mV/m and 50 mV/m. They showed that the response of electron and ion to 10 mV/m electric fields is almost negligible whereas for 50 mV/m a moderate increase was noticed in the ion temperature but not the electron temperature. However, using the Chatanika ISR facility *Schlegel and St.-Maurice* (1981) discovered a correlation between electron temperatures and the electric field. They proposed that the waves produced by Farley-Buneman instability were behind the electron temperature enhancement in the 110 to 115 km altitude range. *Wickwar et al.* (1981) also observed the electron temperature enhancement from 99 to 116 km altitude in the presence of 24-40 mV/m electric field. Many subsequent publications *(e.g., Williams et al., 1992, Jones et al., 1991, Haldoupis et al., 1993, St-Maurice et al., 1990, 1999, Bahcivan*

2007) confirmed the previous results. Specifically, *St-Maurice et al, (1990)* showed that for electric fields in excess of 40 mV/m to 50 mV/m the electron temperature increase markedly, being as much as ten times greater than the regular value. Subsequent studies by *Jones et al. (1991)* and *Haldoupis et. al., (1993)* agreed with that result. In the former paper, plasma waves excited by the Farley-Buneman plasma instability were detected by rocket observations during the ERRIS campaign at the same time as the electrons were being heated. With a detailed study of the F-region T_i and E-region T_e in between 100 to 200 km, *St. Maurice et. al. (1999)* found that electron temperature was actually influenced by the effective electric field rather than the electric field itself. *Bachivan (2007)* showed that when the electric field exceeds 20 mV/m the T_e starts increase extended to electric fields as high as 160 mV/m reaching temperatures as high as 4000 K in the process.

On the theoretical side, *St.-Maurice et al., (1981)* used a wave-particle trapping mechanism to describe the electron heating by Farley-Buneman waves. However, *Pfaff et al.* (1984) showed that the wave amplitudes needed to enhance the electron temperatures from the trapping theory were much higher than waves observed in situ. This led *Robinson* (1986) to propose that wave-particle interactions were behind the electron heating process, arguing that electron–neutral collisions were actually dominated by the electron – plasmon collisions. Along the same vein *Primdahl & and Bahnsen* (1985) suggested that anomalous electron collisions were responsible for the heating. This led *St-Maurice (1987)* to pursue the notion further through a more in-depth study of this question. He showed that there were serious problems with this explanation, including electric fields that were increasing instead of decreasing in the presence of the Farley-Buneman structures. The anomalous diffusion theories all indicated that the plasma conductivity also had to be affected by the large-amplitude waves that heated the electrons.

S*t.-Maurice & Laher (1985)* were the first to suggest that parallel wave electric fields were behind the electron gas heating. This conclusion was supported by *Milikh and Dimant (2003)*. In summary, the parallel electric fields of the waves are now believed to be responsible for the electrons heating in the presence of strong electric fields in the high latitude E-region where electron temperatures as high as 4000K have now convincingly been demonstrated.

Chapter 2

RADAR SYSTEM

The ionospheric environment is studied with various ground-based radars (incoherent, coherent) and various instruments carried on rockets and satellites. For the present research, incoherent scatter radar (ISR) data from Tromso were collected from the Madrigal site. The purpose of this chapter is to present the basic ISR system and its basic techniques. This includes a brief description of the European Incoherent Scatter Scientific Association (EISCAT) ISR system in Northern Scandinavia.

2.1 Radar System

The principle of a normal RADAR (RAdio Detection And Ranging) is to detect the distance and/or the moving speed of a target at regular time intervals. As illustrated in Figure 2.1, a radar transmitter subsystem generates the radiofrequency (RF) energy required for the illumination of a remotely situated target of interest. Receivers are used to record the echo signals. The purpose of the synchronizer is to coordinate the timing and controls the system operation. When a single antenna is used to transmit and receive the signals a duplexer works as a switch to connect them alternately to the antenna. As shown in Figure 2.1 there are seven components common to all radar systems, including those just described.

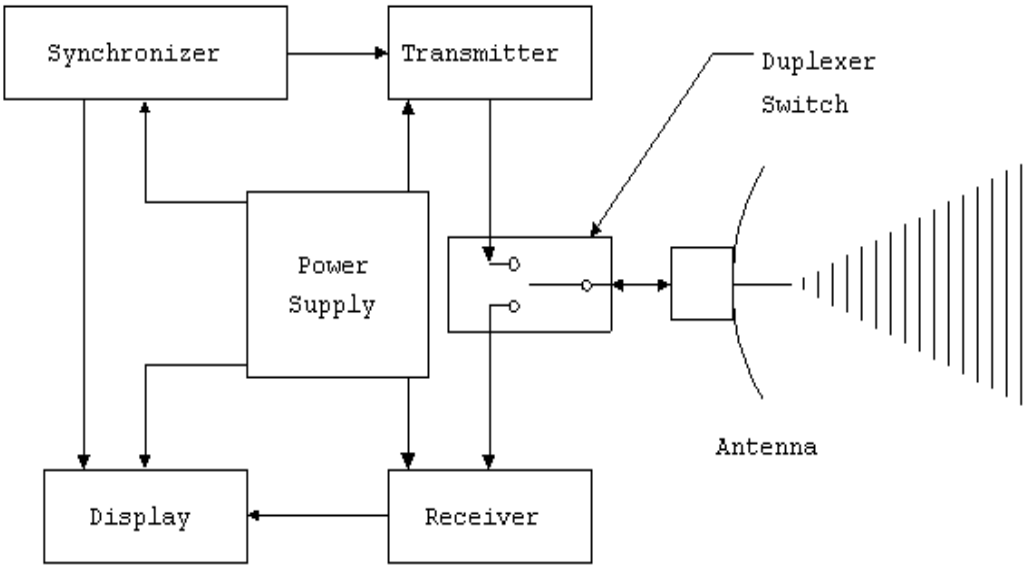

Figure 2.1: Block Diagram of Basic Pulse Radar System *(FAS, 1998)*

2.2 Ionospheric Scatter

Ionospheric properties such as scale height, electron and ion temperature, plasma drift velocity etc. vary markedly with geographic and geomagnetic co-ordinates, local time, solar sunspot and geomagnetic storm *(Hunsucker, 1991)*. Ionospheric scatter from radar signals provides a measure of the full range of parameters, including ion composition, ion temperature, electron temperature and plasma drift velocity *(Benyon & Williams, 1978)*. Single frequency techniques are used for the remote sensing through a measure of the time of flight, amplitude, phase, polarization. For lower frequency radars the angles of arrival are needed in order to account for refractive bending *(Davies, 1990).* Three types of scattering are considered in ionospheric research: coherent scatter, Ionoscatter/Forward scatter and Incoherent scatter. Short scale variations in the electron density is behind coherent and the incoherent scattering. From the incoherent scatter echo spectrum we

can get the information about the magnetoplasma properties. In the next section the incoherent scatter radar system is now discussed.

2.3 Incoherent Scatter Radar and Theory

The observations made over the last decades have shown that incoherent scattering has become one of the most reliable methods of investigating the ionosphere to heights of several thousand kilometres from the ground *(Bowles, 1958).* In ionospheric research, Incoherent Scatter Radar provides the ion and electron density data, electron and ion temperatures and some information about the composition of the ionosphere. Figure 2.2 shows the global distribution of ISR's.

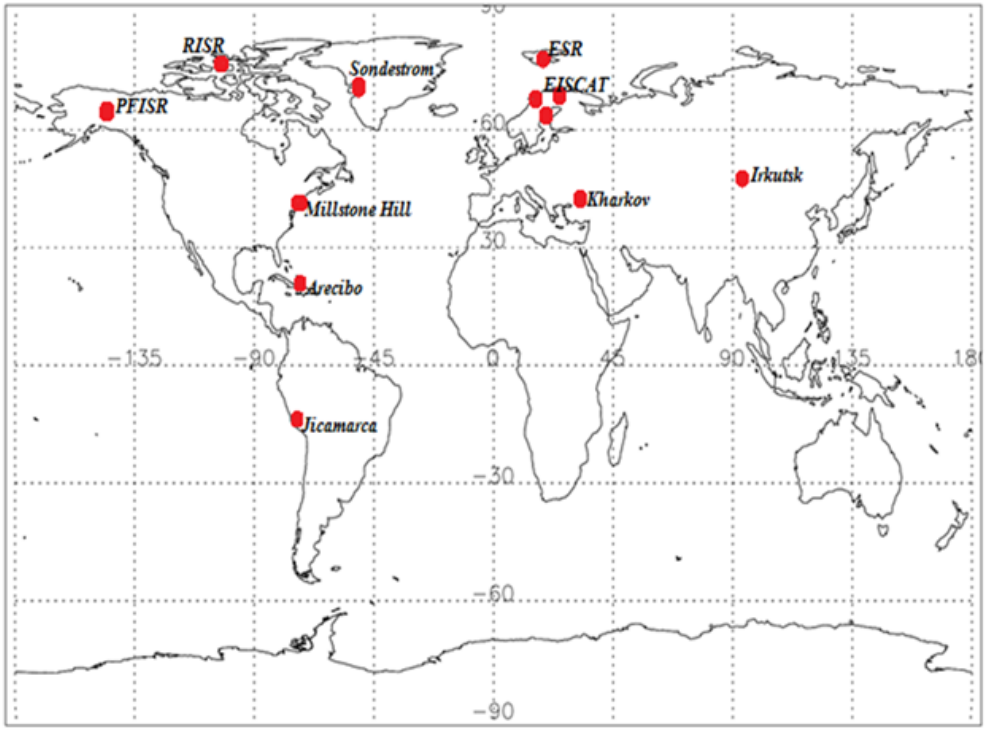

Figure 2.2: Sketch map of Incoherent Scatter Radars around the world

An incoherent scatter radar can observe the ionosphere typically at ranges between 90 km and 2000 km, reaching up to 1000 km altitudes. Table 2.1 lists the incoherent scatter radars that are presently used to probe the terrestrial ionosphere.

	GEOGRAPHIC		CGM	
Station	Lat	Long	Lat	Long
Jicamara	-11.9	284.0	2.3	355.6
Arecibo	18.3	292.3	29.0	9.1
Millstone Hill	42.6	288.5	52.2	6.1
Sondrestom	67.0	309.0	72.41	41.2
EISCAT Tromso	69.6	19.2	66.5	102.9
EISCAT-Kiruna	67.9	20.4	64.7	102.4
EISCAT-Sodankyla	67.4	26.6	62.8	108.0
EISCAT-Longyearbyen	78.2	16.0	75.43	110.68
PFISR	65.2	147.8	----	----
RISR-N	74.7	94.9	----	----
Kharkov	49.6	36.3	45.4	118.7
Irkutsk	52.9	103.3	41.06	104.75
MU-Japan	34.9	136.1	24.9	204.3

Table 2.1: Geographic and geomagnetic Latitude and Longitude of the Incoherent Scatter Radar

Incoherent scattering is a type of electromagnetic wave scattering which detects the electron density fluctuation in the space plasma. The term Incoherent Scatter (IS) refers to the extremely weak scatter from fluctuations in plasma density caused by the random thermal motion of the

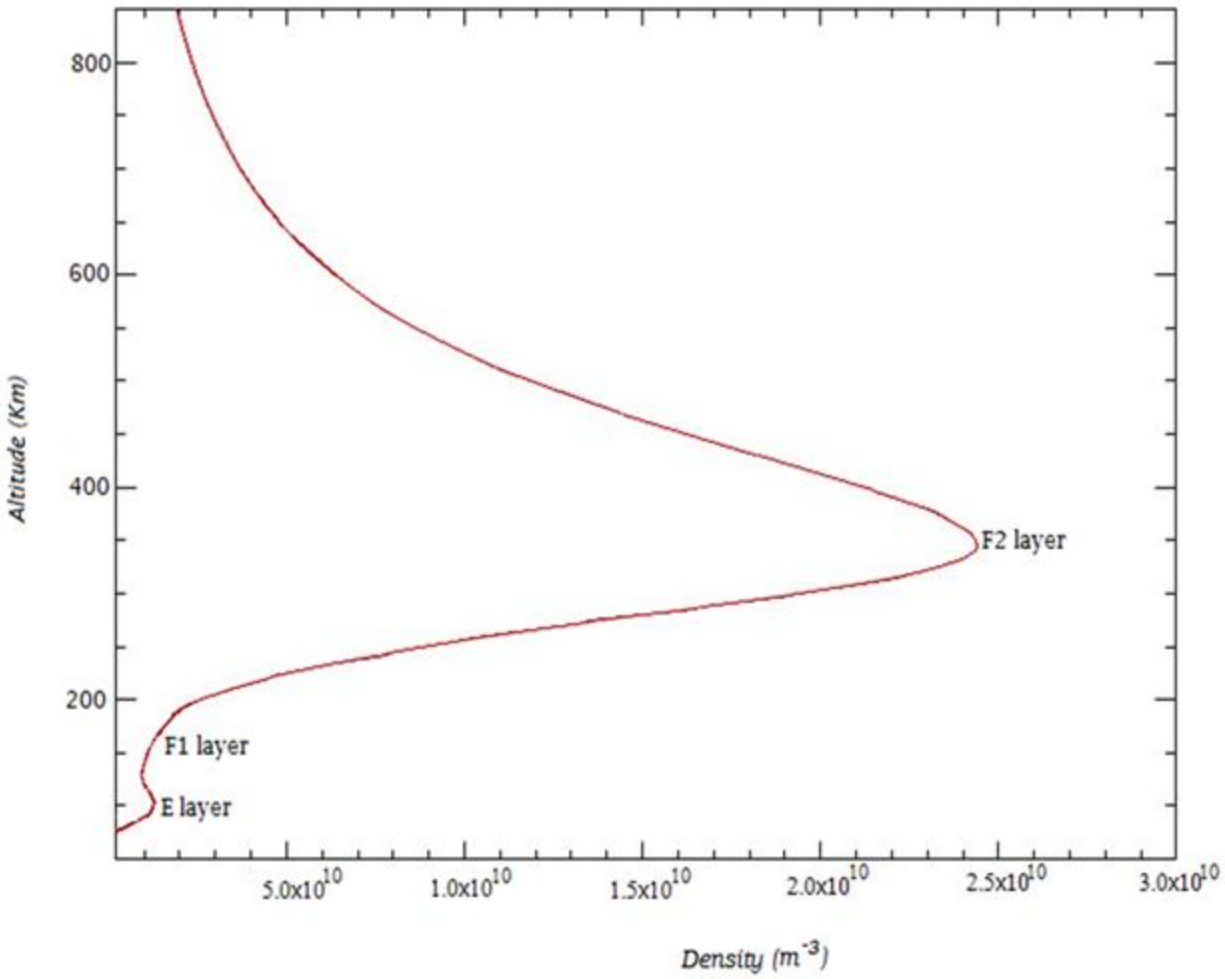

Figure 2.3: Variation of electron density along altitude on UT 1.5 hours on 14th September 2000, Geographic Latitude is 70° (Data from IRI model).

ions and electrons. The electron density fluctuations are created when charged particles move through the plasma. A first task for an ISR experiment is to determine the power spectral density, from which the plasma density can be extracted. When the ISR transmits radar frequency energy pulses in space the free electrons act as the main target. A large part of energy transmitted by the radar antenna is lost to space and only a very small portion is scattered back from the ionosphere Electrons dominate the scattering of the radio waves because of their smaller mass, which allows them to undergo relatively large oscillations in response to the incident electric field from the incident radio waves. The more powerful an antenna receiver is, the more energy scattered from electrons it can detect. The electron density profiles in question were already illustrated in Figure 2.3.

Because of positively charged ions and the electrostatic forces between charged particles, electrons tend to be attracted toward each ion even though, at the same time, their thermal velocities and their mutual repulsion tend to disperse them *(Benyon & Williams, 1978)*. Considering an individual electron, *J.J. Thompson (1906)* proposed a theory based on the scattering of individual free electrons by electromagnetic waves. He correctly found that the ratio of the power scattered from a single electron to the incident power is *(Hunsucker, 1991)*,

$$W = \frac{(r_e \, Sin\Psi)^2}{R^2} \tag{2.1}$$

where R is the distance between the transmitter and the electron, r_e = Electron radius= 2.82×10^{-15} in m and Ψ=Angle between the direction of the incident wave electric field and the observer.

As a result, a radar cross section for the electron in m^2, can be defined as *(Hargreaves & Hunsucker, 2003)*,

$$\sigma_e = 4\pi(r_e sin\psi)^2 = 10^{-28}\sin^2\psi \tag{2.2}$$

where the electron radius, $r_e = \frac{e^2}{\varepsilon_0 m_e c^2}$ and for backscatter $\sigma_e = 4\pi r_e^2$. The cross section σ_e is $1.00 \times 10^{-28}\ m^2$ for a single electron when it scatters electromagnetic radiation. *Farby (1928)* suggested that this phenomenon might be useful to investigate the ionosphere. *Gordon (1958)* followed up by suggesting that a powerful radar system might be revealing the mystery behind waves scattered by the free electrons. In the same year, *Bowles (1958)* did his first observation using a large transmitter to a dipole antenna array. *Fejer (1960)* stated that the radar cross section per unit volume is

$$\sigma = N\sigma_e \tag{2.3}$$

Here N is the electron density *(Hargreaves & Hunsucker, 2003). Buneman (1962)* showed that the effective cross section of the incoherent scatter radar is

$$\sigma_{eff} = \frac{\sigma_e}{\left[(1+\alpha^2)\left(1+\frac{T_e}{T_i}+\alpha^2\right)\right]} \tag{2.4}$$

Here $\frac{T_e}{T_i} < 3.0, T_e$ and T_i are the electron and ion temperature respectively and $\alpha = 4\pi D/\lambda$, where *D* is the Debye length and λ is the radar wavelength. This new expression arose because it was found that a shielding layer forms around ions due to the electrons, the scale of which (*D*) is determined by the balance between random thermal energy and electrostatic potential energy, giving

$$D = \left(\frac{\epsilon_0\, kT_e}{Ne^2}\right)^{\frac{1}{2}} = 6.9\left(\frac{T_e}{N}\right)^{\frac{1}{2}} \tag{2.5}$$

where T_e is in $°K$ and N is in cm^{-3}. Minimum values of *D* are about 0.3 cm at the peak of the F region (~250 km) with values of 6 cm or more in the lower E region (~90 km) or at very great heights (~2000 km) *(Benyon & Williams, 1978)*.

When the Debye length is greater than the wavelength of the radar then the related scattering can be considered to come from the free individual electrons. Gordon's prediction is then satisfied for the observed spectrum from individual electrons. However, when the wavelength is much higher than the Debye length, the observed scattered signals come from collective behavior, namely, 'plasma waves' and their associated electron density fluctuation.

In *Gordon's (1958)* original work the spectrum comes from the electron random thermal motion and the scattered signal should have a Gaussian distribution. The Doppler width (Δf_e), in this case, can be mathematically expressed as

$$\Delta f_e = \frac{1}{\lambda}\left(\frac{8kT_e}{m_e}\right)^{\frac{1}{2}} \tag{2.6}$$

Here, Δf_e = Magnitude of Doppler shift of an electron approaching the radar at the mean thermal speed, T_e = electron Temperature, k=Boltzmann'a constant and λ= radar wavelength in meters. In the ionosphere T_e and N clearly depend on altitude, time of day, season and degree of solar activity *(Benyon & Williams, 1978).*

Because of the electrostatic coupling, plasma waves or ion-acoustic waves are generated by the random thermal motion of ions. The waves occur over a wide and continuous spectrum of

wavelengths propagating in all directions and for upward travelling waves (along the direction of the radar beam) the Doppler shift of the scattered wave *(Benyon & Williams, 1978)* is

$$\Delta f = -\frac{2V}{\lambda} = -\frac{2V}{\lambda} = -F(\lambda/2) \qquad (2.7)$$

Here, *V* is the speed of the wave. $F(\lambda/2)$ is wave frequency and *F* is a function of *V*. Similarly the downward Doppler shift (along the direction of the radar beam) will be $+F(\lambda/2)$. Here, $-F(\lambda/2)$ and $+F(\lambda/2)$ are the frequencies for upward and downward waves respectively and $\lambda/2$ travels upward and downward with velocity *V* along the radar beam.

The typical 'incoherent scatter' echo spectrum is characterized by a double hump if $T_e > T_i$). The actual shape depends on the T_e/T_i ratio *(Davies, 1990).* The two shoulders of the ion line are linked up with approaching and leaving ion acoustic waves with a speed $\sqrt{\frac{K_B(T_e+T_i)}{m_i}}$. When the electron temperature increases, the width of the spectrum also increases since the ion-acoustic speed increases with T_e. From the spectrum width, we can measure the electron temperature and ion temperature. Figure 2.4 shows the spectral shapes for different electron to ion temperature ratios. It can be seen that if we keep T_i constant but increase T_e the velocity of the ion acoustic wave increases *(Benyon & Williams, 1978).* As T_e/T_i increases, the Ion acoustic peaks develop and move further apart *(Raman, et al., 1981).* As a result, the ion spectrum peaks become sharper. The intensity of the overall spectral decreases slightly (Equation 2.4).

The entire plasma is usually in motion and if there is a plasma drift, the entire spectrum will be shifted instead of being centered on the transmitter frequency.

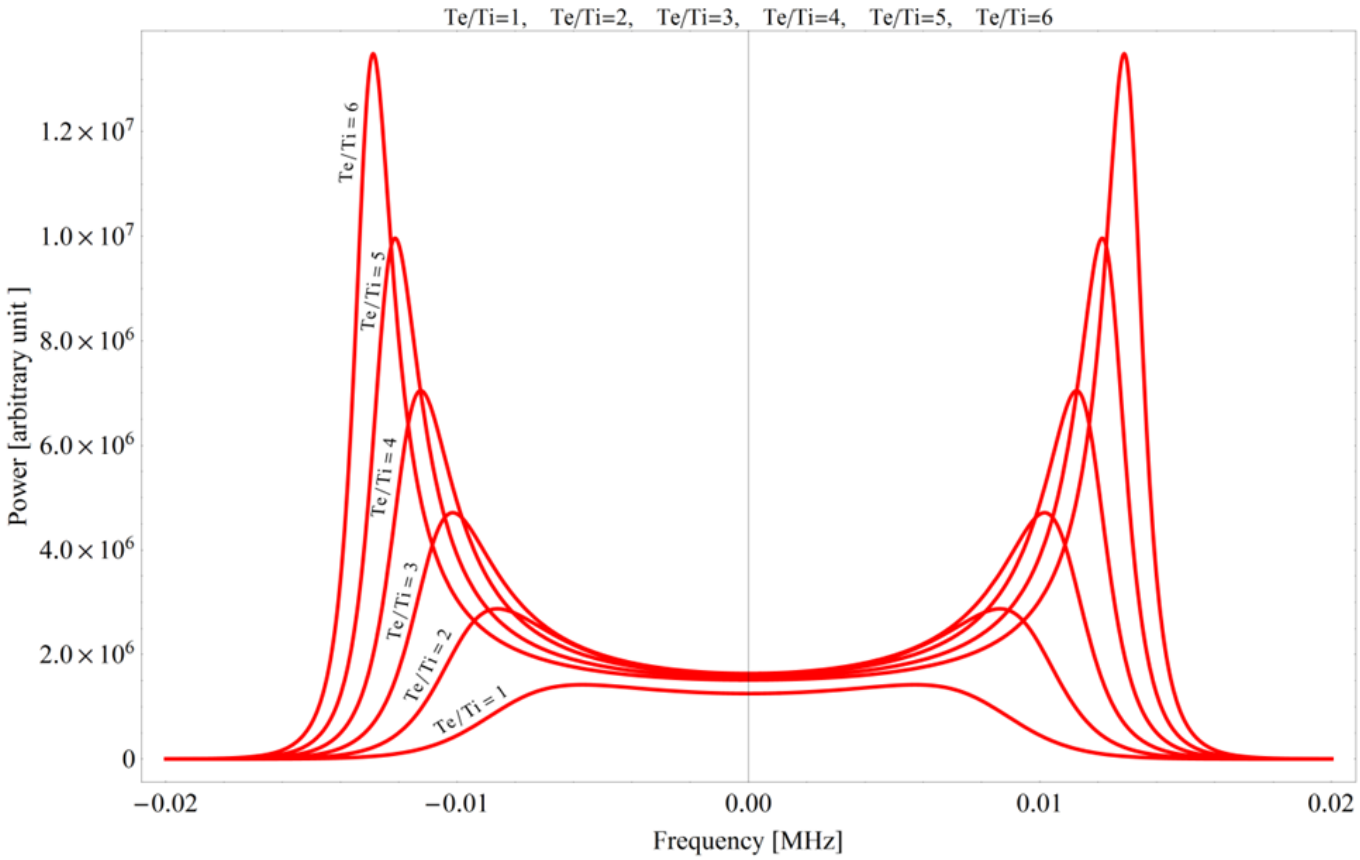

Figure 2.4: Shapes of the ion line for oxygen atom for different T_e/T_i *(Dalipi & Syla, 2013)*

2.4. Parameters Derived from ISR

As discussed in the previous section, if the complete spectrum of the scattered signal is measured with adequate signal-to-noise ratio some parameters can be measured directly *(Benyon & Williams, 1978).* From the directly measured parameters, several other parameters can be determined, such as the ambient electric field, the Hall and Pedersen conductivities, the wind speed etc. With the help of Figure 2.5 it can be shown that the parameters that can be inferred directly from the spectra are

a) Electron Density (N_e): The density N_e is proportional to the area under the curve of the returned spectrum i.e. the total area of the spectrum *(Mendillo, et al., 1990).*

b) Plasma Velocity (V_p): The plasma line of sight velocity can be determined by measuring the mean Doppler shift of the scattered spectrum. The frequency shift (f_0) from the transmitted frequency f_t gives the mean plasma velocity through the Doppler effect.

c) Electron to Ion Temperature ratio:The Ratio (T_e/T_i) can be determined from the intensity of the shoulders in the ion-acoustic spectrum.

d) Ion and Electron Temperature (T_i and T_e): Ion temperature and electron temperature can be determined from the spectrum width which depends on $T_i + T_e$ while the spectrum shape gives T_e/T_i.

Ion mass from altitude profiles can also be derived from profiles, while the ion-neutral collision frequency below 105 km affects the spectral shape so that it can also be determined, assuming $T_e = T_i$ which is usually a good approximation.

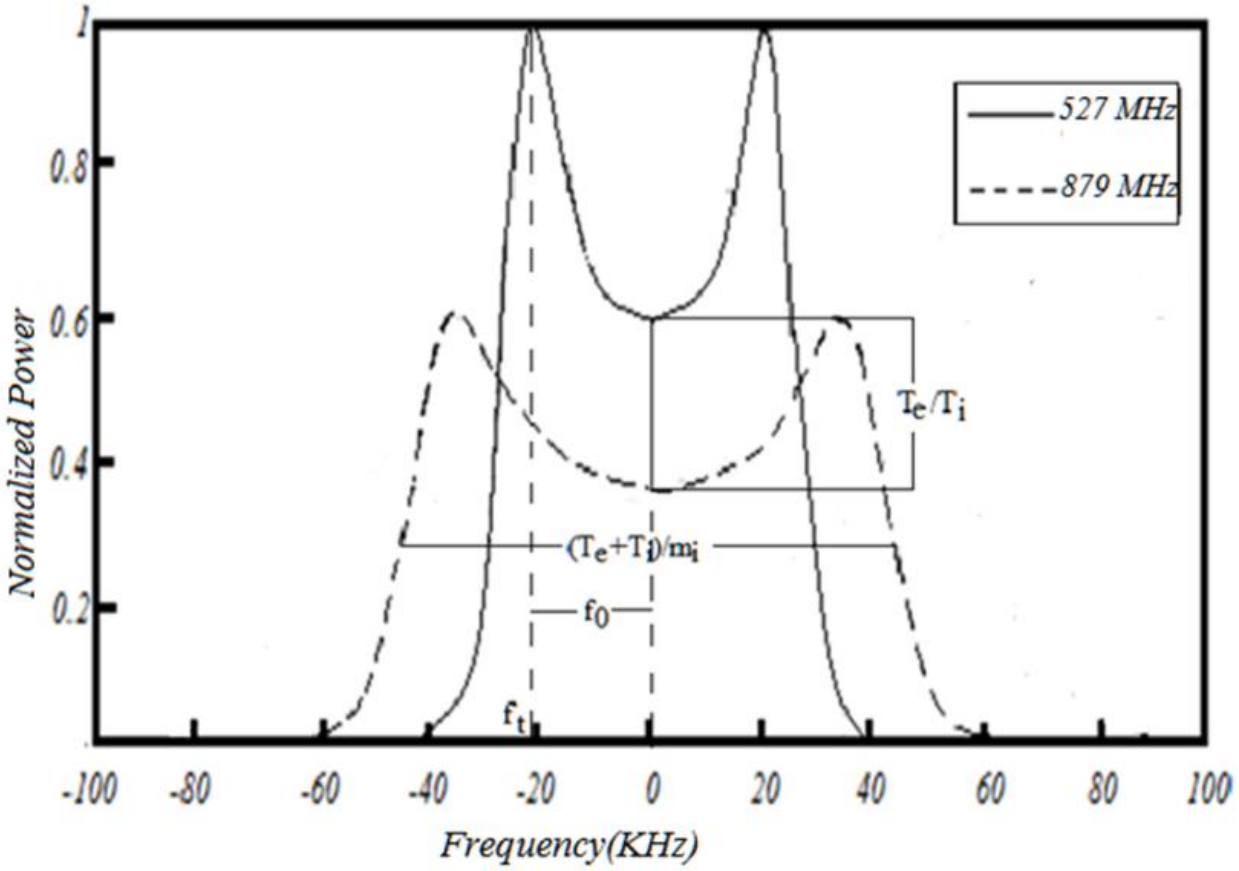

Figure 2.5: Normalized Incoherent Scatter Radar is shown for 2 different radar operation frequencies of 527 MHz (close to AMISR radar frequency), 879 MHz (close to EISCAT, Tromso radar frequency) and the value of T_e/T_i is *2 (Diaz, et al., 2008).*

2.5 EISCAT ISR System:

As mentioned before, the EISCAT system uses the incoherent radar technique to study the lower, middle and upper atmosphere. For its ionospheric studies, EISCAT operates the UHF, VHF and the Svalbard radar (ESR) incoherent scatter radars, an Ionospheric Heating facility, and a Dynasonde in Northern Scandinavia (*Limi, et al., 2014*).

The EISCAT UHF radar in Tromso (Norway) is a tristatic system. The central frequency is 929.5 MHz with a peak transmitter power of more than 2.0 MW. It includes a transmitter and receiver at Tromso and additional receiving sites located near Kiruna (Sweden) and Sodankylä (Finland). The antennas and receiver hardware at all three sites are identical, although of course the transmitter is unique to Tromso *(Limi, et al., 2014).*

In addition, the EISCAT VHF radar in Tromso (Norway) is a monostatic system. Its central power is 224 MHz with a peak transmitter power of 1.6 MW. A monostatic system is a radar system in which for transmitting and receiving share the same antenna.

The EISCAT Svalbard radar (ESR) near Longyearben is again a monostatic system. The central frequency of ESR is 500MHz and the peak transmitter power is 1.0 MW.

2.5.1 Overview of EISCAT Experiments

For EISCAT experiments, various modulation schemes and scan patterns can be used. In the experiments, for modulation schemes, two different pulse references are used namely: plain pulses and pulses with an applied phase code.

Plain pulses are RF transmission phase-continued pulses between few μs to around 1 ms long. Power profiles and long pulses applications use plain pulses. Power profiles are short pulses with less than 10 μs lengths whereas for long pulses typically the range is between 200 and 400 μs (*Limi, et al., 2014)*. As mentioned before, in an incoherent scatter radar (ISR) experiment, a radio wave is transmitted to the ionosphere where a small fraction of the original signal is scattered to the receiver antenna. Lagged products of the received signal and its complex conjugate are calculated to produce samples of the signal autocorrelation function (ACF) *(Virtanen, et al., 2008)*. By means of a fitting routine from the ACF observations, different plasma parameter can be determined. In the E-region, the incoherent scatter is narrow and the autocorrelation function is correspondingly long. In the F-region, the autocorrelation function displays a much more heavily damped oscillatory behaviour, with a decorrelation time of a few hundred μs, in other words the same order as the length of a typical long pulse (*Limi, et al., 2014*). As long as proper time scales are taken into account the ACF and spectra are equivalent.

There are different types of experiments which depend on the investigated altitude. The default pointing directions for the antennas for each experiment are known as radar scan patterns *(Limi, et al., 2014)*. There are 6 types of Common Program (CP) scan patterns: CP1, CP2, CP3, CP4, CP6 and CP7. For each site the scan patterns used for each experiment are listed in Table 2.2.

Location	CP1	CP2	CP3	CP4	CP6	CP7
UHF	tau2pl	tau2pl	tau1	tau1	---	---
VHF	---	---	---	tau8	manda	tau8
ESR	steffe	steffe	tau0	tau0	manda	tau7(tau0)

Table 2.2: Scan pattern for each EISCAT radar *(Limi, et al., 2014)*

The common program scan patterns for EISCAT radar system need to be described briefly because of their relevance to the present study. Note that CP1, CP2 and CP3 are designed for the UHF system and CP4, CP6 and CP7 run on the VHF system.

CP1: Height range is in between 86-600 km and time resolution is about 5 seconds. The antenna is pointing along the magnetic field line. Usually this scan pattern is used to investigate the electron heating, solar-cycle variations, and various other auroral phenomena.

CP2: CP2 is a 4-positions scanning experiment with a cycle time of 6 minutes with a dwell period of 90 s *(Howells, 2009)*. It is used to study travelling disturbances, tides, neutral winds and can calculate E-region velocities

CP3: CP3 is a 17 positions scanning experiments to study the convection mapping, field aligned currents, the spatial arrangement of plasma phenomena and the aurora over a broad latitude range. The cycle time is 30 minutes.

CP4: CP4 covers almost 80° N of the geographic latitudes and the elevation is low. Two beams are operated in a swinging position and used to map convection in the polar cap in collaboration with optical experiments on Svalbard *(Howells, 2009).*

CP6: CP6 probes low altitudes with a height range 60-130 km. The antenna is pointing along the vertical direction. It is mainly a D-region experiment. It is used to study Polar Mesosphere Summer Echoes (PMSE).

CP7: This is a high altitude VHF program, typically focusing on the 250-1700 km height range in the vertical direction *(Howells, 2009)*. This experiment was designed for polar wind studies.

Table 2.3 indicates the basic parameters of each experiment listed in table 2.2 for all the radar system:

Mainland UHF / VHF System

Experiment name	Dish	Pulses (μs)	Sampling rate (μs)	Resolution (km)	Ranges (km)	Time resolution (s)
tau2pl	UHF	two 16x36 AC	12	1.8 - 5.4	50-702	5
tau1	UHF	two 16x60 AC	12	1.8 - 9	54-1361	5
tau1	VHF	two 16x72 AC	24	4 - 11	61-2014	5
manda	UHF/VHF	64x3 AC	3	0.45	58.5-513	6
arc1	UHF	64x6 AC	6	0.9	96- 422	0.44

Table 2.3: Basic parameters of each experiment of UHF and VHF radar

The mainland experiment sets have two kinds of modulation schemes, namely, newer generation schemes and older generation schemes. The newer generation mainland experiments (arc1, arc_dlayer, arc_dlayer_ht, dlayer, manda, pia, tau1, tau2, tau2_pl, tau3, tau7 and tau8) use improved signal processing system and, mostly, they allow improved resolution using alternative

codes. The older generation use long and short pulse system for their experiments. For the present research the data have been used from the Tomso UHF incoherent scatter radar. This means that arc1, tau2, tau2_pl, manda experiments were used. A brief description of these experiments is now given.

arc1 - This experiment is meant for high time resolution studies. It exploits time-slicing techniques to get 0.44s time resolution. It is mainly coded for UHF and remote UHF systems *(EISCAT, 2014)*.

Code	Sampling Speed (μs)	Lowest Decoded Range	Highest Decoded range
128 different 64 bits	6	95.7 km	422.4 km

tau1 – It is mainly designed for the VHF experiments to observe the long latitude slice through low elevation F-region. This experiment is quite similar to tau2.

Code	Sampling Speed (μs)	Lowest Decoded Range	Highest Decoded range
16 bit AC,5	12	54 km(partial),187(fully)	1354 km

tau2 – This experiment was designed to use 16-bit alternating codes to cover in between 90 to 750 km altitudes. The sample resolution is 1.8 km, but unique data are only available at 5.4 km range resolution *(EISCAT, 2014)*.

Code	Pulse Length	Start Range	End Range	Range Res.
Power Profile	2us (x 13)	63	198	0.3
Power Profile	2 us (x 13)	63	198	0.3

Alt. Code	36 us (x 16)	90	720	5.4

tau2_pl – It is a moderate version of tau2. To allow longer range gates out, it used longer phase reception which gives it twice the number of signals obtained in tau2 *(EISCAT, 2014).*

Code	Sampling Speed (μs)	Lowest Decoded Range	Highest Decoded range
16 bit AC, 3	12	50 km (partial), 1 29 (fully)	702 km

manda – This experiment is intended to observe the electric field to join this with D-region and some degree of F-region observations.

2.6 Method of Data Collection

For the present research I focused only on the ion and electron heating of the E-region and lower F-region. To make sure the electric field was the same at all range gates, I only considered data obtained when the EISCAT UHF Tromso antenna was pointing along the magnetic field. To access the data set I used the Madrigal database, which is a science database for the upper atmosphere.

For this research the international polar Year (IPY) data from 2007-2008 have been used. The IPY dataset was chosen because during the IPY the radar ran for the whole year. After analysing the one-year data, a small number of relevant events was uncovered. From the data header, relevant information was obtained from the data file. Only data obtained by looking along the Earth's magnetic field were retained. Five types of experiments (listed in table 2.2) were appropriate. In the end, only seven events displayed electron heating by strong electric fields (the electric field was not often strong during the IPY, which was a time during which the sun was particularly quiet).

The central frequency of the EISCAT UHF radar is 929.5 MHz. The spectrum is greatly affected by collisions with neutrals at the lower altitude gates. Hence, it was impossible to routinely go below 105 km. We were therefore limited to three different altitudes (110,115 and 120km) for our study of the electron temperature. We used the 150 km altitude for the ion temperature based on the notion developed by *St-Maurice et al. (1999)*, which in the absence of good electric field data from line-of-sight observations of the plasma drift, the ion temperature at 150 km could provide a reasonable scalar estimation of the electric field.

Chapter 3

DATA ANALYSIS AND RESULTS

Incoherent Scatter Radar (ISR) data from the IPY dataset were taken and analyzed for this thesis. This chapter presents the process of obtaining the electron and ion temperatures in the E-region from the data collected by the EISCAT ISR system. A significant portion of the data analysis involves the removal of noisy events. The connection between E-region T_e enhancement and the lower F-region T_i (to infer the electric field) is used to study the E region electron temperature response to electric fields.

3.1 Data overview

The measurements came from the EISCAT incoherent scatter radar. The selected datasets were from observations made along the Earth's magnetic field line in order to insure that all altitudes were affected by the same electric field. Though a large dataset was collected, we focused only on events with higher electron temperatures than usual. Electron and ion temperatures were recorded as a function of altitude.

During the International Polar year (IPY) the radar operated nearly continuously for 365 days. For this work we extracted IPY (2007-2008) data from the Madrigal database. Specifically, the data were obtained during the period of 3rd March 2007 to 2nd March 2008. The list of extracted parameters contains

DAYNO: Day number of year (universal time) - Units: day

BEGINNING TIME (BHHMMSS): Beginning hour/min/sec (UT) - Units: hhmmss

END TIME (EHHMMSS): Ending hour/min/sec (UT) - Units: hhmmss

MLT: Magnetic Local Time (hour).This parameter gives the magnetic local time of a particular point in space and time.

GDALT: Altitude (height) - Units: km

ASPECT: Magnetic aspect angle. The angle between the magnetic field line and the radar beam at a given point in the beam. Units: degree

Ne (DENSITY): Electron density (Ne) - Units: m^{-3}

$\mathbf{N_eL}$: Log10 (Ne in m-3) - Units: $\log_{10}(\mathrm{m}^{-3})$

$\mathbf{DN_eL}$: Error in Log10 (Ne in m-3) - Units: $\log_{10}(\mathrm{m}^{-3})$

$\mathbf{T_i}$: Ion temperature (T_i) - Units: K

$\mathbf{DT_i}$: Error in Ion temperature (T_i) - Units: K

$\mathbf{T_e}$: Electron Temperature. Units: K

$\mathbf{DT_e}$: Error in electron temperature, Units: K

Ion and electron temperatures and the electron density were recorded as functions of altitude. To get the values along a magnetic field line, the aspect angle was selected to be 178 to 180 degrees while the altitude range under consideration was 80 to 250 km. For this work, we focused on ion temperatures at 150 km altitude and electron temperatures at 110,115 and 120 km altitudes. In the end, 138 datasets were collected. After plotting the electron temperature against the ion

temperature, two different sets of plots were observed, namely, what we defined as "Good events" and "Noisy events".

Good Events: Smooth profiles with altitudes and low temperature error (no larger than 20%) are defined as Good Events.

Noisy Events: When the profiles with altitude are complicated and the temperature errors are large, the events have been defined as Noisy Events. Note that the error bars were determined through a fit of the data to known theoretical spectra. Noisy data had larger error bars because of larger uncertainties with the parameters extracted from the fits.

In the lower E-region, the standard electron temperature during the day ranges from approximately 200 K to 300 K and increases with height. When the electron temperature enhancement exceeds the background temperature by more than 100 K, it is considered a heating event. For the non-heating days, the electron temperatures are expected to be close to the background neutral temperature.

Four different types of events profiles are shown below. These are for heating but noisy events (Figure 3.1 and 3.2 at 3-minute time interval), non-heating noisy events (Figure 3.3 and 3.4 at 3 min time interval), heating good events (Figure 3.5 and 3.6 at 3-minute time interval) and non-heating good events (Figure 3.7 and 3.8 at 3-minute time interval).

Figure 3.1 shows the profiles of the ion and electron temperatures and electron density with altitudes along the magnetic field lines on 30th November 2007. The top plots shows one individual profile obtained between 00:05:00 and 00:08:50 UT, complete with error bars. The bottom plot shows the median retrieved during the two-hour interval that the event lasted together with the 25% and 75% envelopes (since there was no other way to compute an error bar

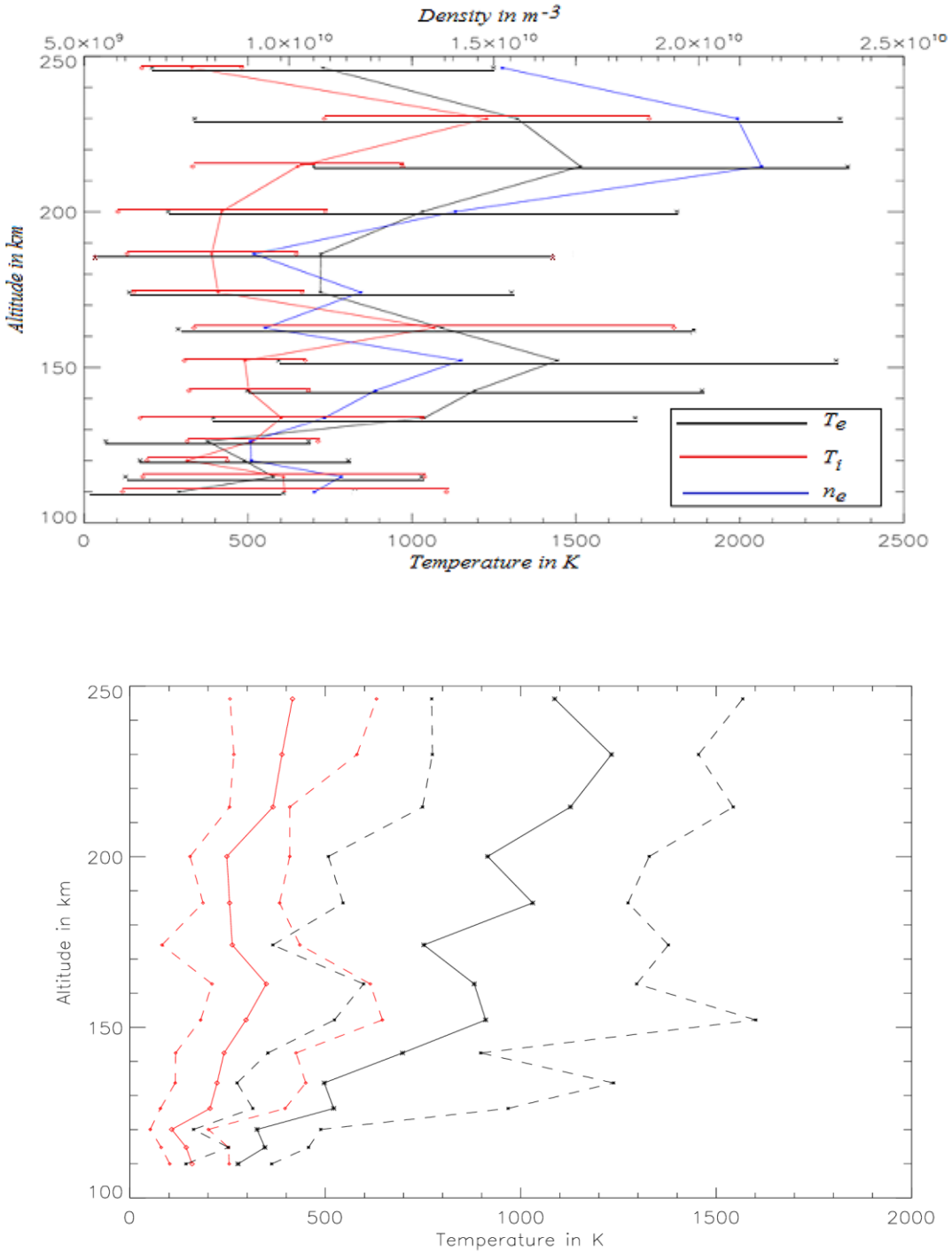

Figure 3.1: Profile of T_i, T_e and n_e along magnetic field line on 30th November 2007 for a heating but noisy event.for the time period 00:05:00 to 00:08:50 UT (Top Plot). Corresponding temperature medians (full lines) and 25 and 75% envelopes for the 2-hours period 00:00:00 to 02:00:00 UT (Bottom Plot) .

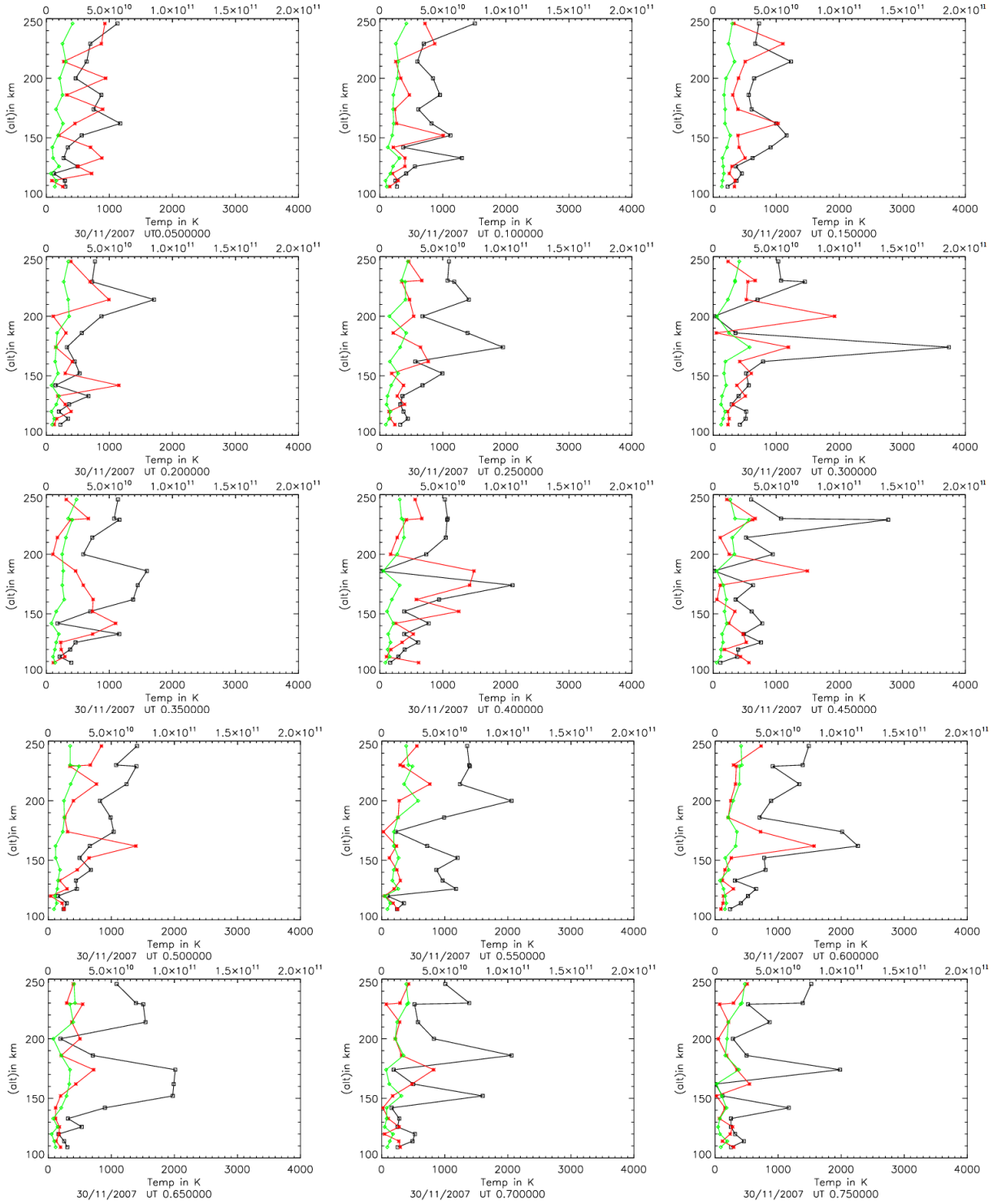

Figure 3.2: Profile plots of electron temperature (black), ion temperature (red) and electron density (green) at 3 minute time intervals on 30th November 2007 (heating but noisy event). The error bars are not shown to make the plots more readable (red lines =T_i, black lines = T_e and green lines= n_e).

for this dataset). As seen in Figure 3.1, the electron temperature ranges from roughly 300 K to 450 K below 120 km. A large uncertainty in the temperatures is observed, because the density is very low, namely, around $5.5 \times 10^9 \ \ m^{-3}$and therefore the signal to noise ratio is quite high. A notable feature is the steady increase in the median T_e between 100 and 250 km on November 30th .

Profiles of electron, ion temperature and electron density at 3 minute time interval are displayed in Figure 3.2 without the error bars to make the plots more readable. These examples are classified as heating events because T_e is greater than T_i on average at the lower altitudes. There is nothing unusual with T_i but something unexpected about T_e, given that there is no evidence for precipitation which could otherwise be a source of heat, not just ionization. One could speculate that there is some type of electrodynamics involved. At low densities small current densities along the magnetic field may produce large T_e. It is known that the frictional heating is proportional to the square of the electron velocity. When only a few electrons are available to carry currents, they have to go fast along the magnetic field and can get heated by friction even though this electrodynamics does not imply huge amount of currents. *Barjatya et. al. (2013)* found large T_e (around $1000\ K$) where the electron density was $10^{10}\ m^{-3}$ or less. Using frictional heating they found that the electrons were moving fast (2 km/s) even though the current was only $1 \mu A/m^2$. However, given that the trend appeared to be real in spite of lack of evidence for an electric field, it may well be that a culprit other than electrodynamics was behind the observations. For instance there might have been a heat flow from above which drove strong temperatures all the way down to 100 km because the electrons had a rather small heat capacity, given their small density at the time.

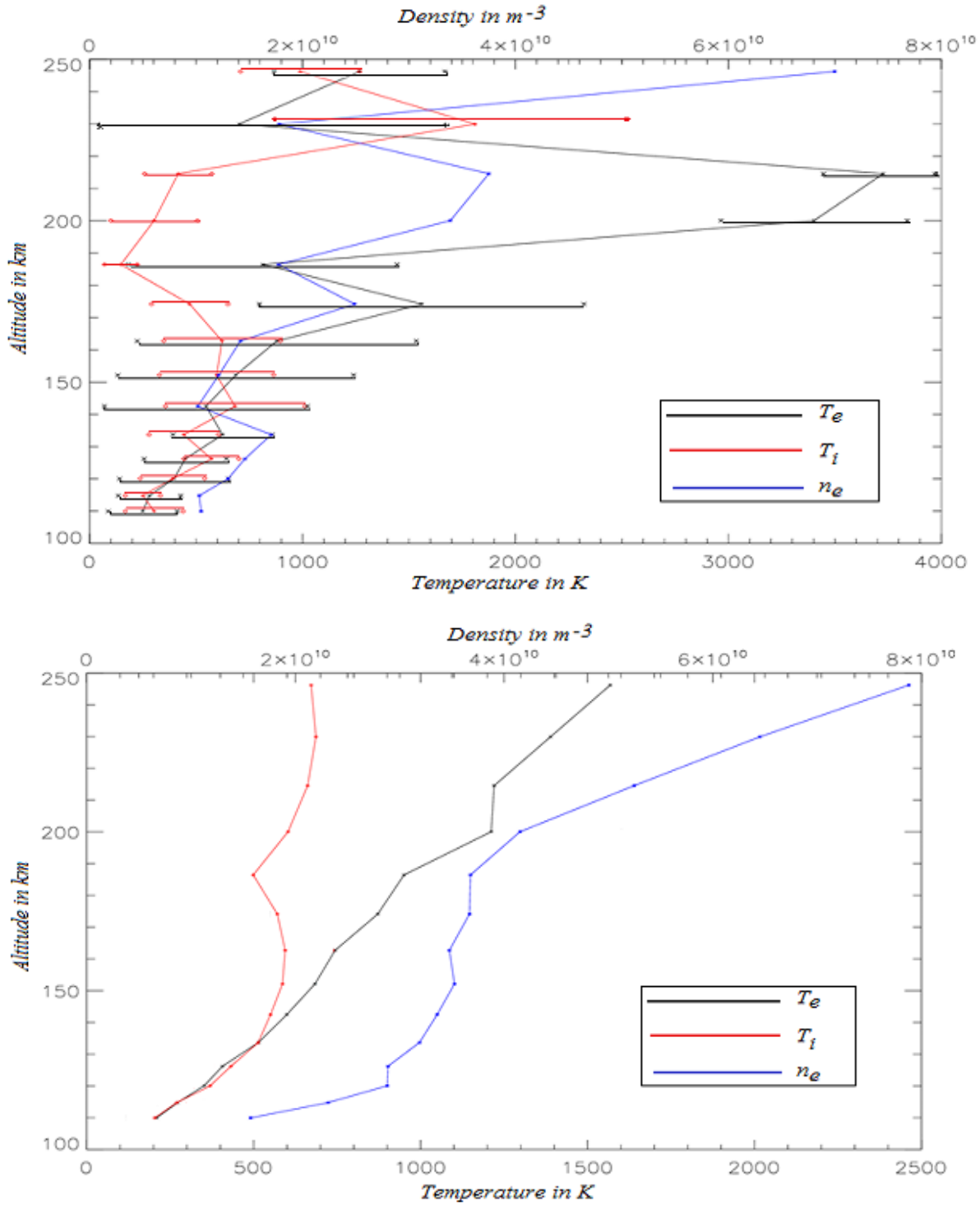

Figure 3.3: Profile of T_e, T_i and n_e along magnetic field line on 3rd November 2007 for the time period 22:01:59 to 22:04:59 UT (Top Panel) and corresponding average for the 2-hours period 22:02:00 to 00:00:00 UT (non-heating and noisy event).

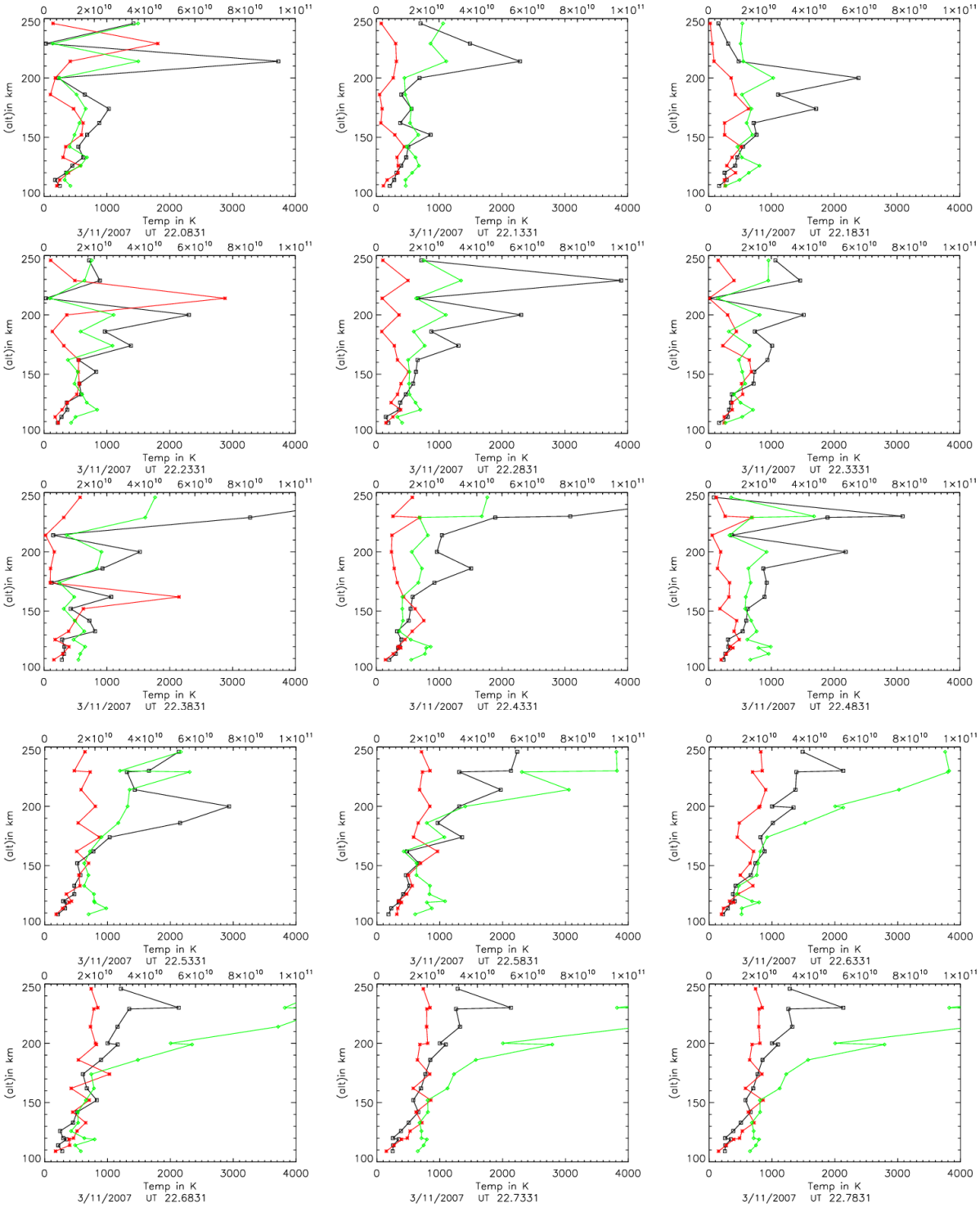

Figure 3.4: Profile plots of electron temperature (black), ion temperature (red) and electron density (green) within 3 minute time interval on 3rd November, 2007 (non-heating and noisy event). The error bars are not shown to make the plots more readable (red lines =T_i, black lines = T_e and green lines= n_e).

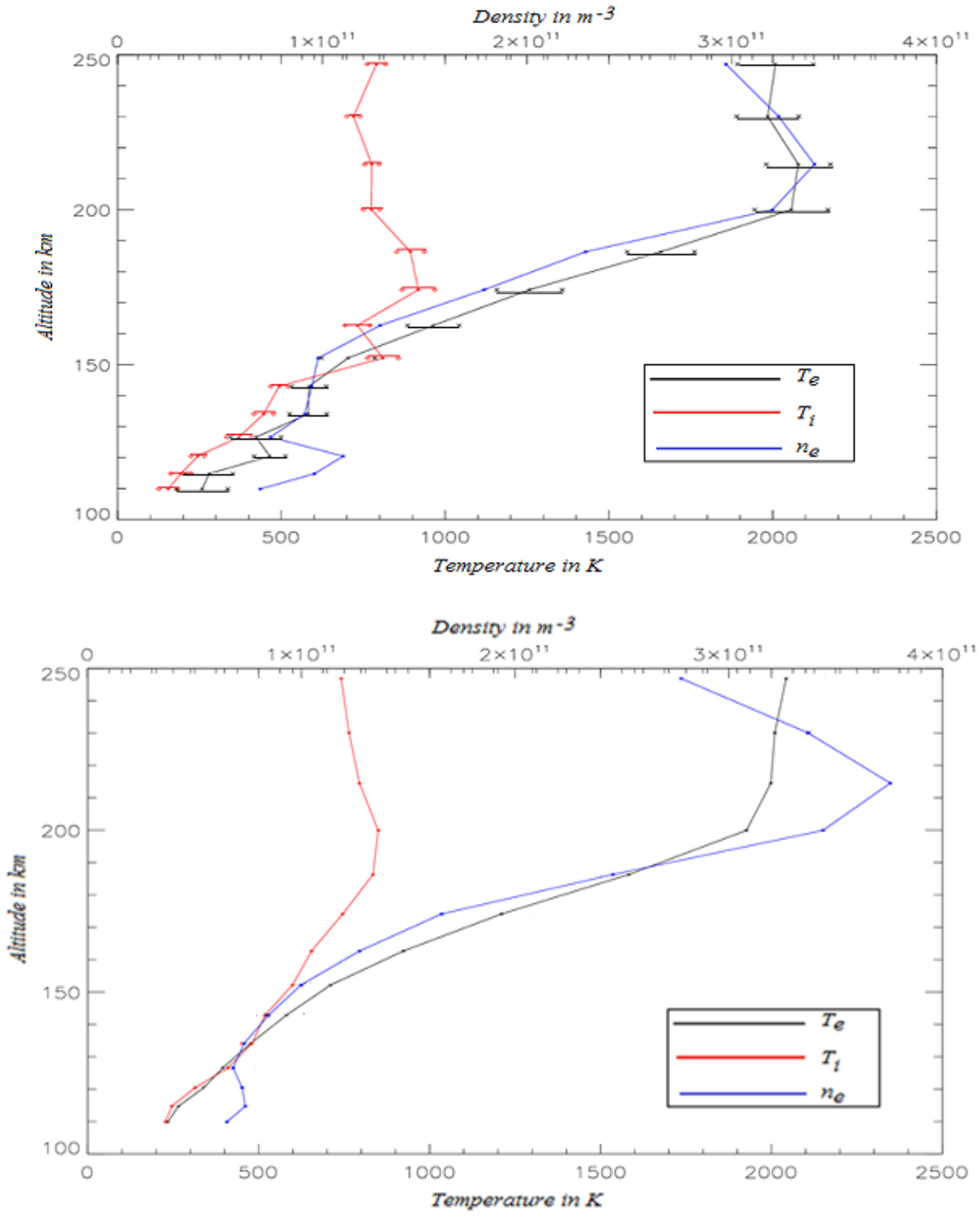

Figure 3.5: Profile of ion T_e, T_i and n_e along magnetic field line on 8th October 2007 for the time period 10:32:45 to 10:36:00 UT (Top Panel) and corresponding average for the 2.5 hours period 10:32:00 to 11:59:00 UT (non-heating and good event).

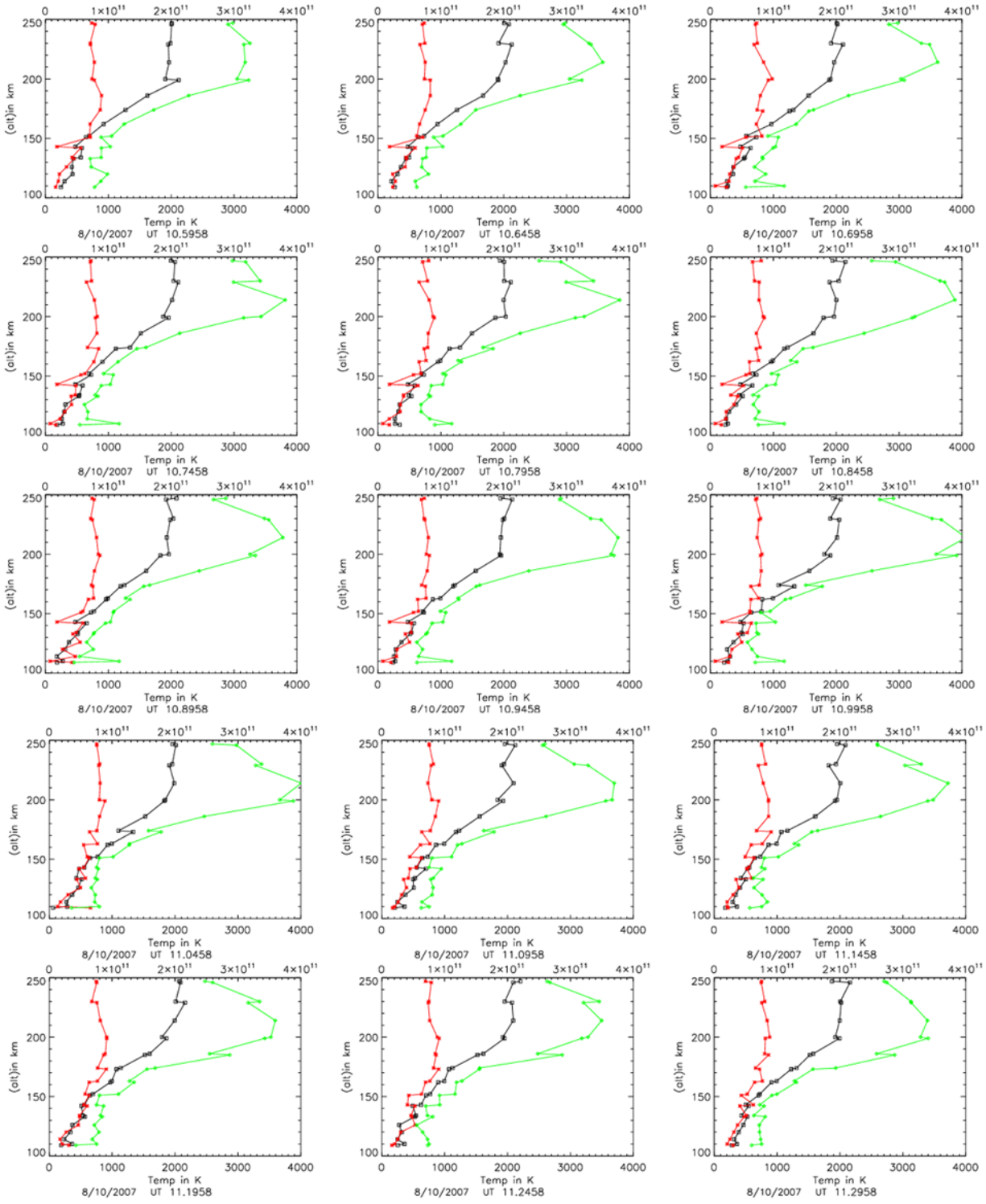

Figure 3.6: Profile plots of electron temperature (black), ion temperature (red) and electron density (green) within 3 minute time interval on 8th October, 2007 (non-heating and good event). The error bars are not shown to make the plots more readable (red lines are T_i, black lines are for T_e and green lines are for n_e).

Figure 3.3 presents profiles of T_i, T_e and n_e along magnetic field line for a non-heating noisy event. It is a night time event so that a colder ion temperature is expected. Figure 3.3 and 3.4 are presented using the same format as Figure 3.1 and 3.2 respectively but for a noisy non- heating event obtained at 22:02:00 to 00:00:00 UT when the electron density was higher than on the previous instance. Figure 3.5 is a non-heating and good event profile. Here the electron density is much larger and the electron temperature at the lower altitude is around 200 K. The electron temperature increased up to 2000 K with altitude. The peak for the ion temperature is 800 to 900 K. It is a daytime event (noon). Ion temperature is a bit higher because of higher neutral temperature.

When considering all the datasets available along the magnetic field line we find a few events with very large T_e at low altitude only 7 good heating events associated with estimated electric fields exceeding 40mV/m were found for the whole year. Figure 3.7 is a profile of one good heating event where T_e at low altitudes was high. In Figure 3.8, we can see a good heating event starting at 19.45:00 UT.

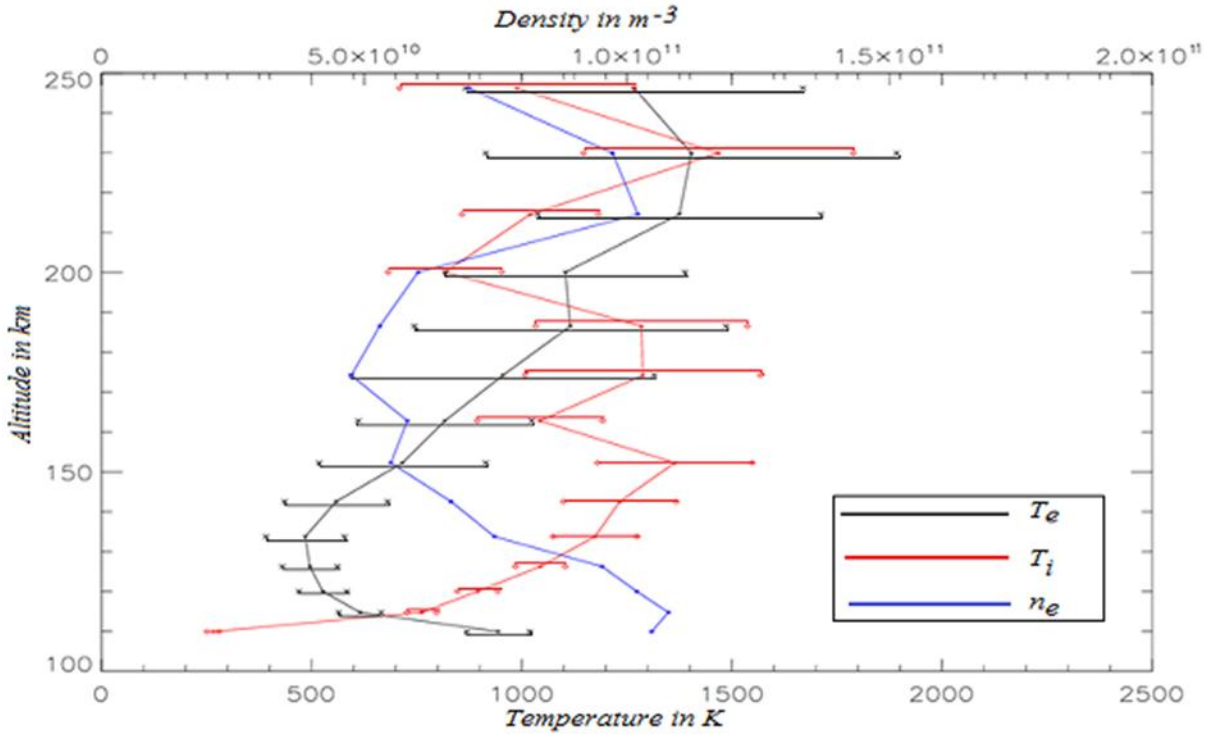

Figure 3.7: Profile of T_e, T_i and n_e along magnetic field line on 8th February, 2008 for the time period 19:32:59 to 19:35:59 UT (heating and good event).

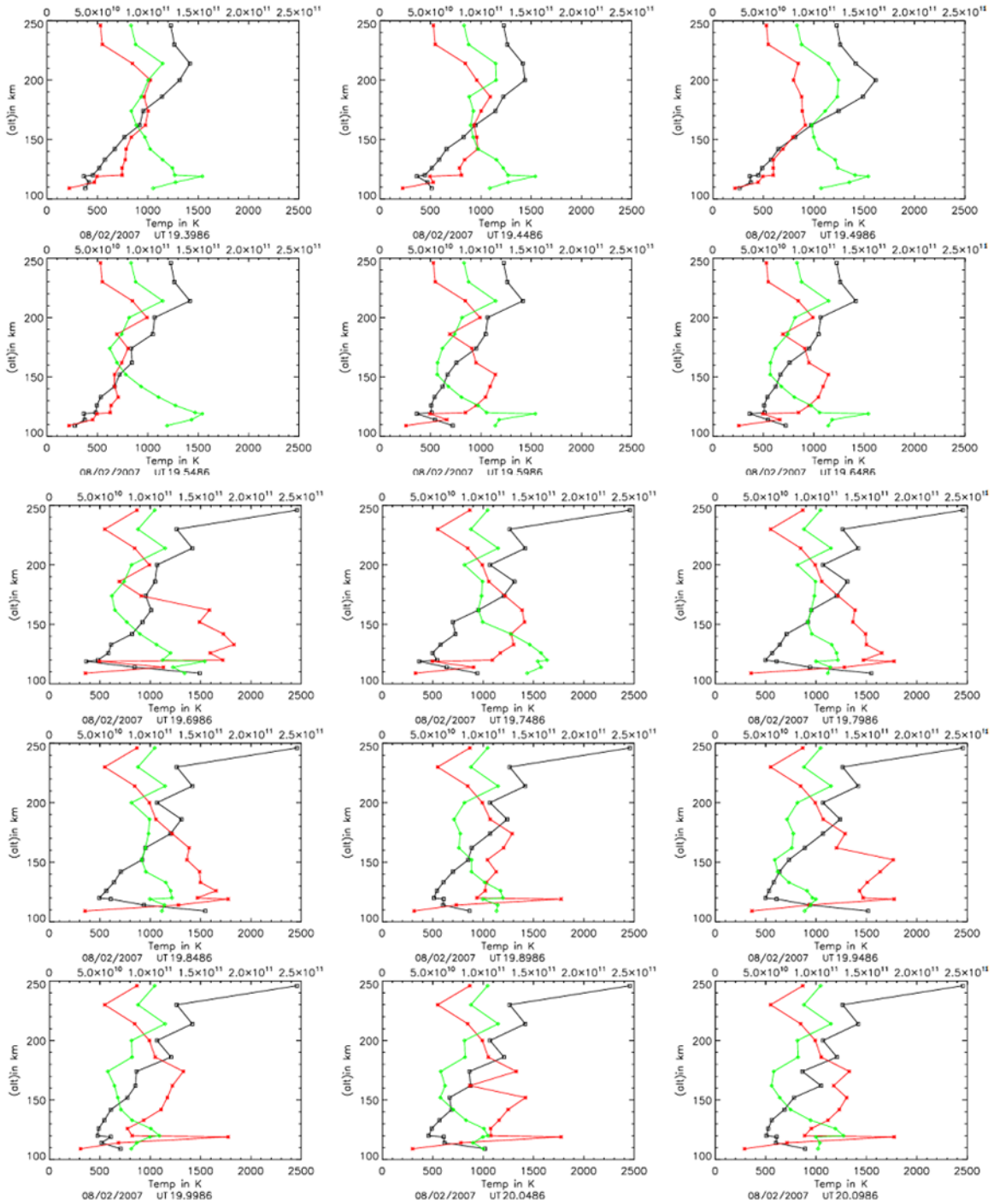

Figure 3.8: Profile plots of electron temperature (black), ion temperature (red) and electron density (green) at 3 minute time interval on 8th February 2008 (heating and Good event). The error bars are not shown to make the plots more readable (red lines are for T_i, black lines are for T_e and green lines are for n_e).

3.2 Electron Temperature (T_e) enhancements through electric fields

Because the ions are only heated by friction in the E and lower F-region, the E-region ion temperature around 150 km altitude can be a good indicator for the electric field strength *(St.-Maurice, et al., 1999)*. For this reason, we have produced scatter plots of the E-region electron temperature from 3 different altitudes versus the ion temperature at 150 km. The data came from the kinds of data shown in the profile plots (like Figure 3.8). These plots show that in the response to the electric fields responsible for the increased ion temperature at 150 km, electron temperatures are often well above the background temperature in 'non noisy' heating events if T_i exceeds 1000 K at 150 km. The electron temperature (T_e) increase ranges from approximately 600 K to 3000 K. These 'good events' temperatures are presented below Figure 3.9a to 3.9g. As discussed in Chapter 1, strong electric fields are expected to heat the electrons below 120 km altitude through large amplitude waves produced by the Farley-Buneman instability *(St.-Maurice, et al., 1999)*.

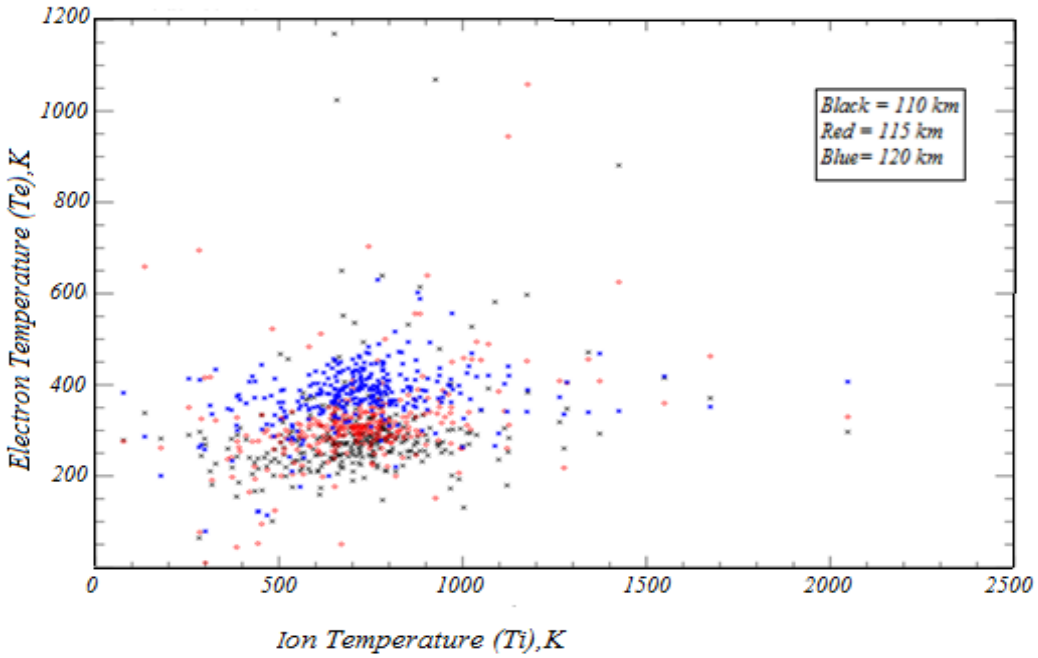

Figure 3.9a: Scatter plot of ion temperature at 150 km and electron temperatures at 110 km, 115 km, 120 km along magnetic field line on 18th October, 2007 for the time period 0:01:00 to 01:30:00 UT and 18:31:00 to 22:27:00 UT.

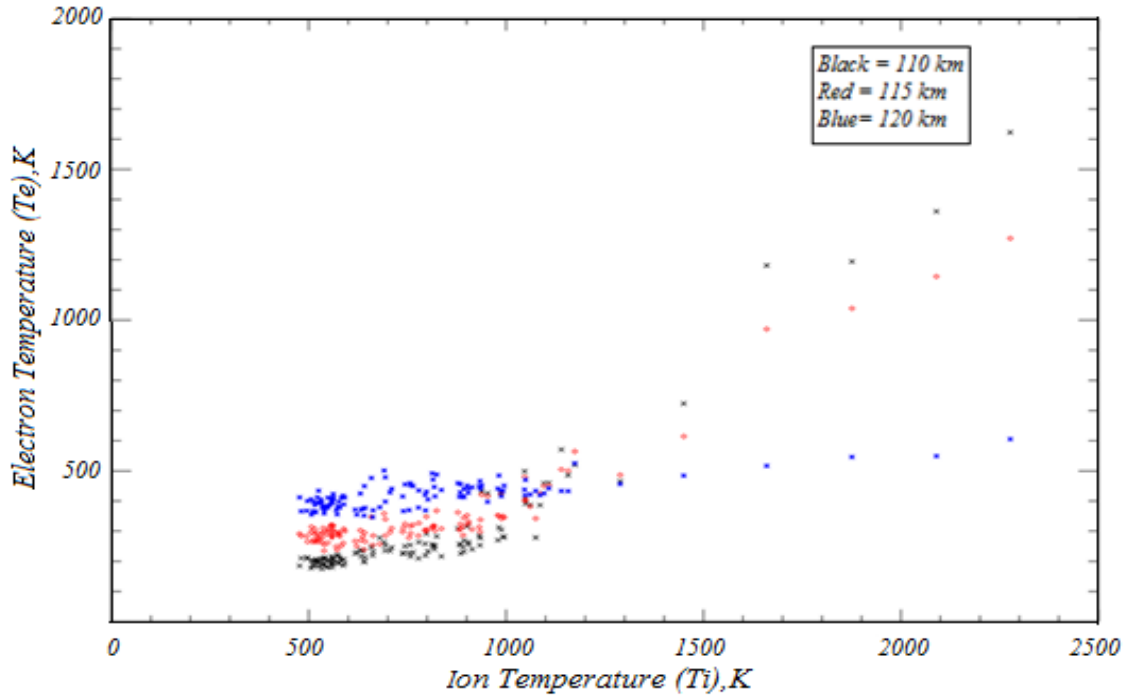

Figure 3.9b: Scatter plot of ion temperature at 150 km and electron temperatures at 110 km, 115 km, 120 km along magnetic field line on 19th November, 2007 for the time period 22:00:00 to 00:01:00 UT

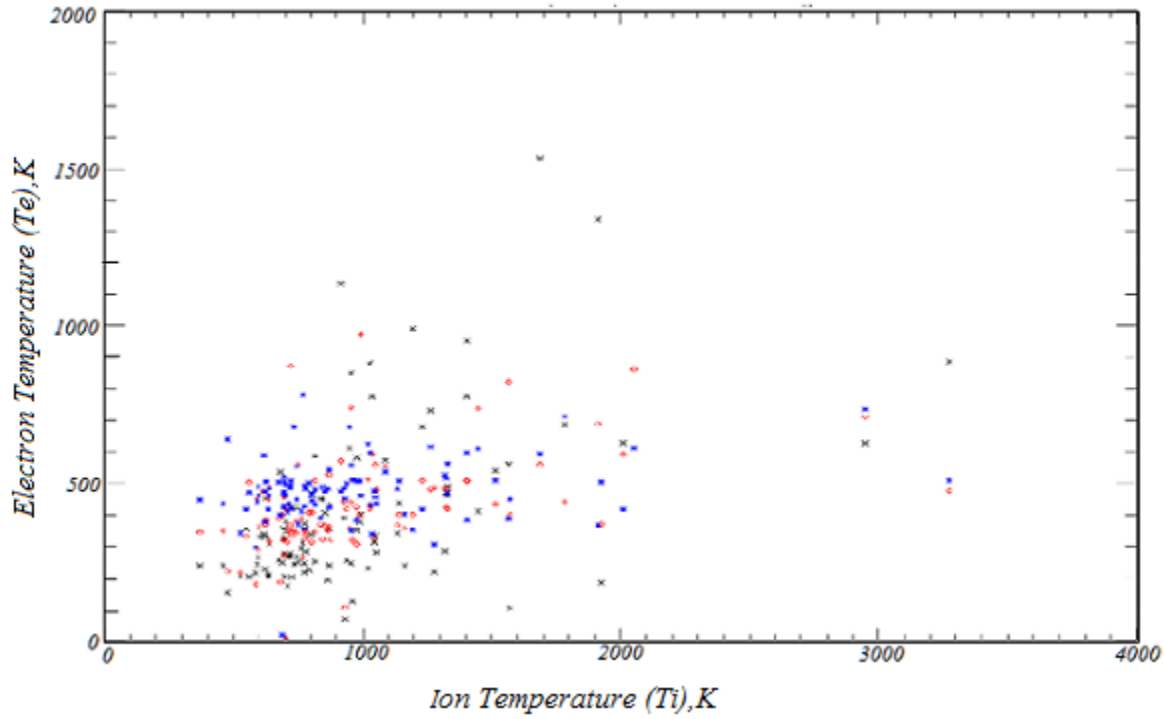

Figure 3.9c: Scatter plot of ion temperature at 150 km and electron temperatures at 110 km, 115 km, 120 km along magnetic field line on 11th December, 2007 for the time period 12:12:00 to 13:54:00 UT

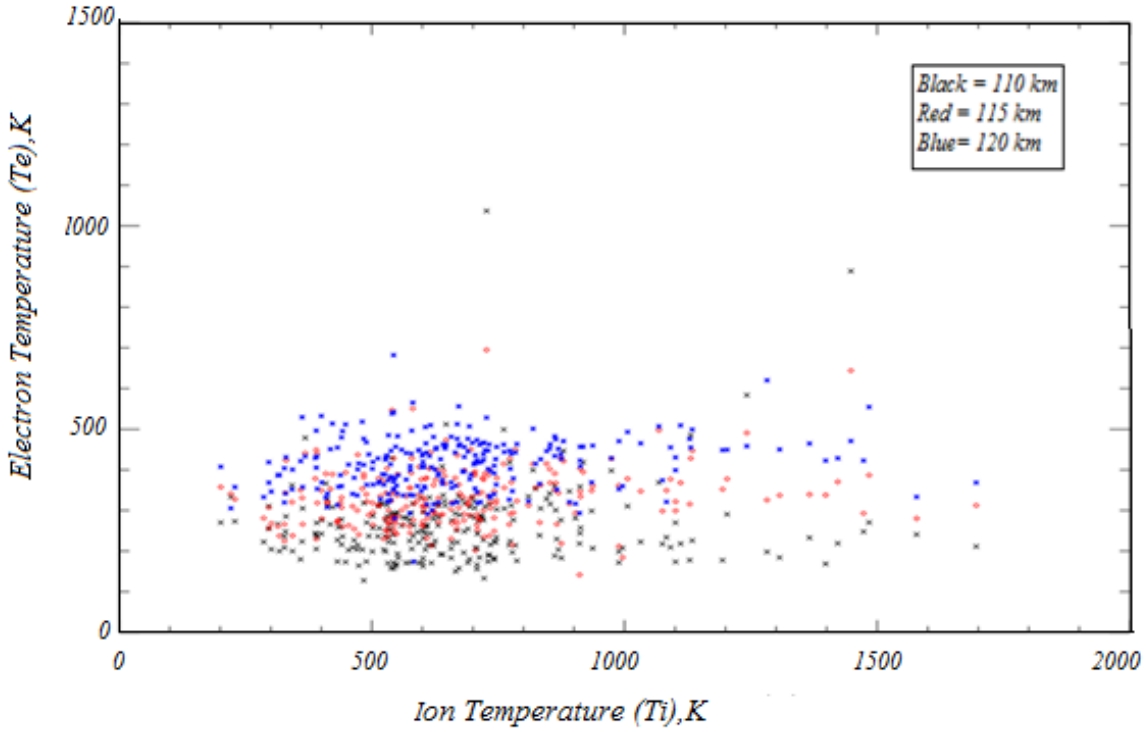

Figure 3.9d: Scatter plot of ion temperature at 150 km and electron temperatures at 110 km, 115 km, 120 km along magnetic field line on 12th December, 2007 for the period 06:16:00 to 23:57:00 UT

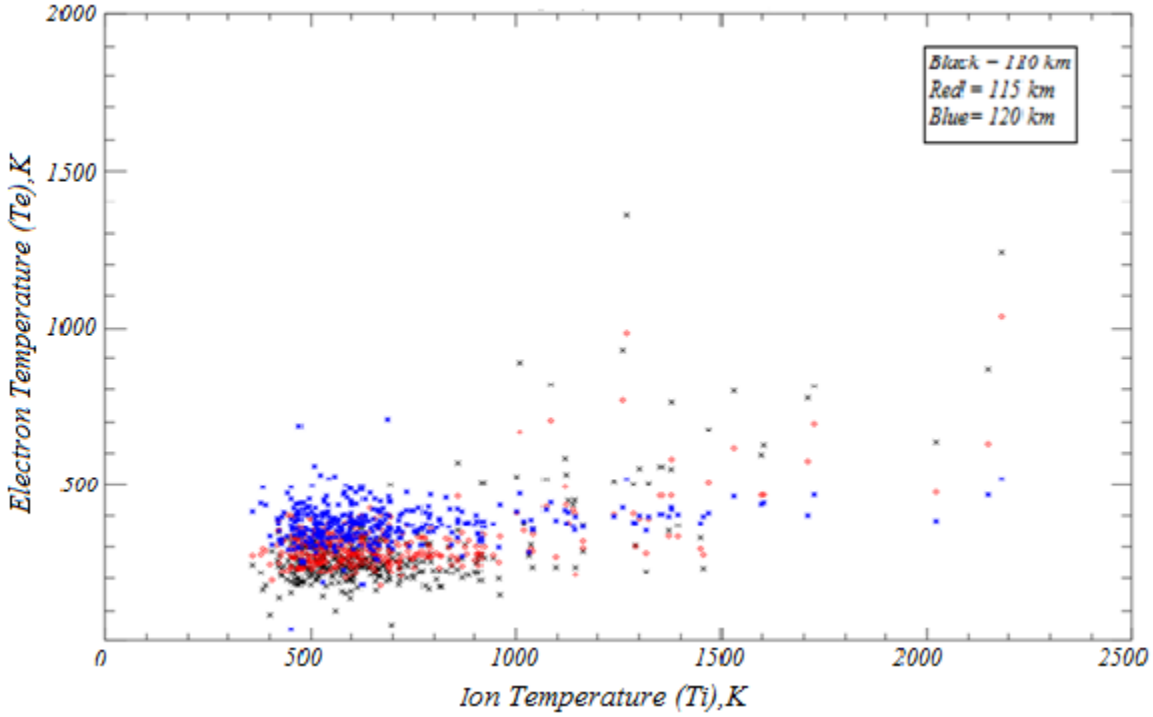

Figure 3.9e: Scatter plot of ion temperature at 150 km and electron temperatures at 110 km, 115 km, 120 km along magnetic field line on 5th February, 2007 for the period 18:00:00 to 00:01:00 UT

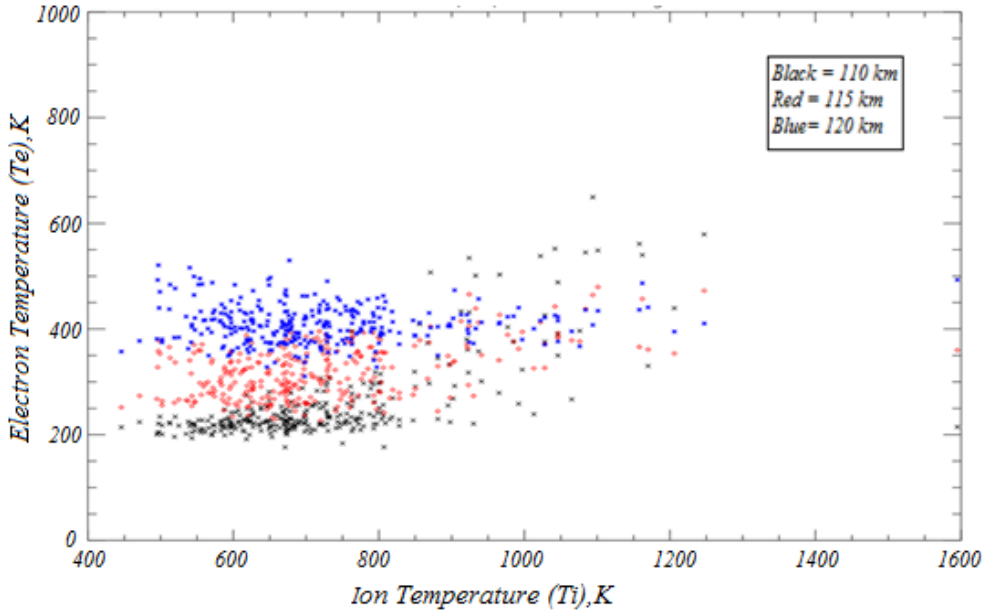

Figure 3.9f: Scatter plot of ion temperature at 150 km and electron temperatures at 110 km, 115 km, 120 km along magnetic field line on 6th February, 2007 for the period 18:34:00 to 00:01:00 UT

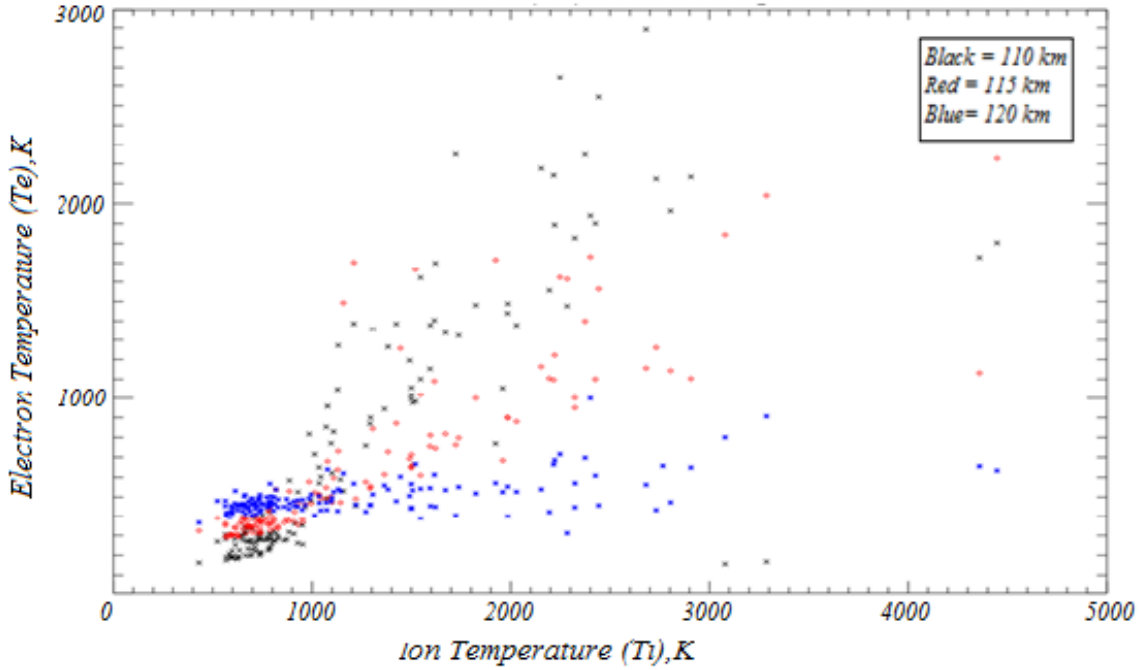

Figure 3.9g: Scatter plot of ion temperature at 150 km and electron temperatures at 110 km, 115 km, 120 km along magnetic field line on 8th February, 2007 for the period 18:44 to 21:14 UT

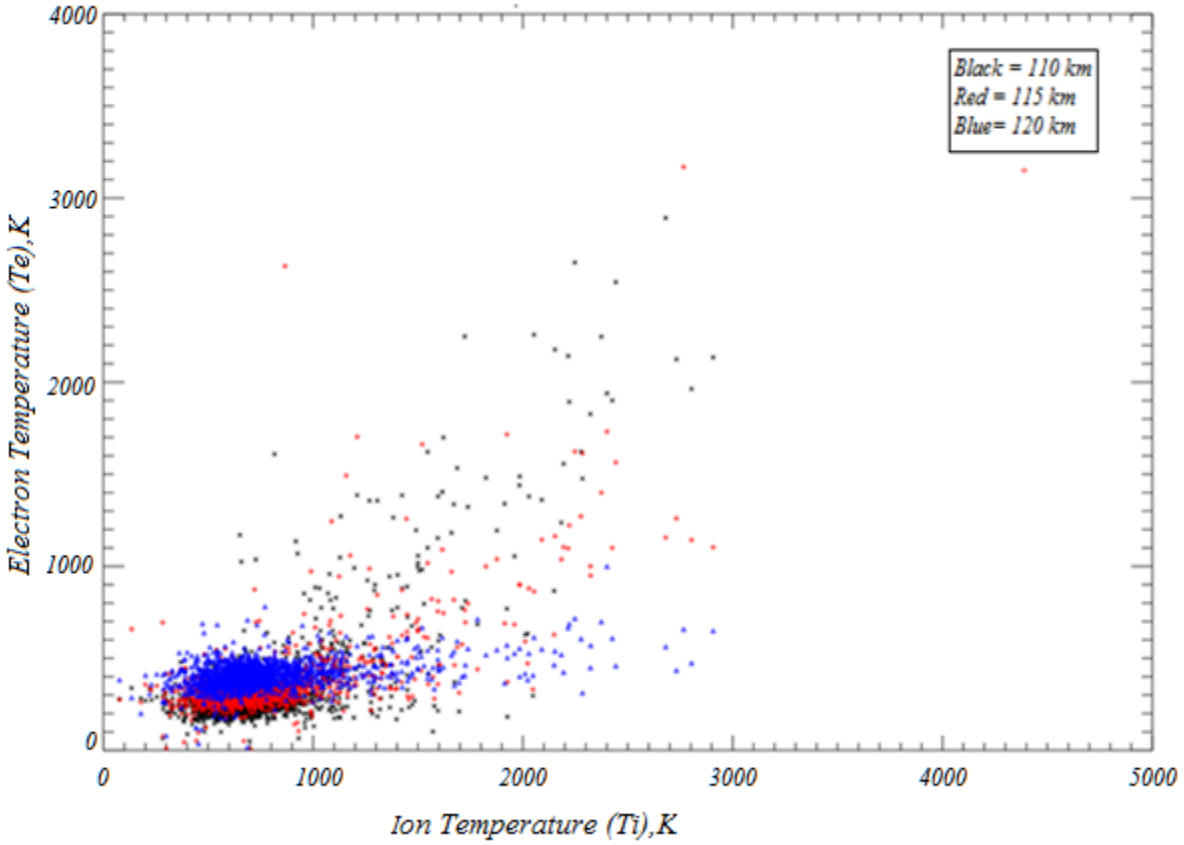

Fig: 3.10: Scatter plot of all good events (top). The X-axis is for the ion temperature at 150 km and the Y-axis is for the electron temperature at various heights depicted through different colors.

Given the significant amount of scatter in heating events, we merged all the scatter data point of the seven events, as shown in Figure 3.10. This figure shows that when the electric field is strong, that is, when T_i at 150 km increases above 800 K, then at 110 and 114 km T_e also increases. The electron temperature enhancement goes from roughly 200 K to 2500 K above the background temperature.

All the scatter plots show the trend of increasing electron temperature (mainly at 110 and 115 km) when the ion temperature is 1000 K and above. However, from these data we still need to convert

from the electron temperature as a function of T_i to an electron temperature as a function of electric field strength. To present the relation between temperature changes with the changing ion temperature (and attendant electric field) we first produced some time intervals plots. We plotted the MLT (magnetic local time) sequences of the electron temperature at three different altitudes and the ion temperature at 150 km. Here we can more clearly see that only when the ion temperature at 150 km exceeds about 1000 K the electron temperature at 110 km and 115 km shows a strong tendency to go up. For instance, Figure 3.11 shows that the electron temperature is enhanced when the ion temperature at 150 km is also going up. If we consider MLT in between 18.6 to 18.7 in particular, where the ion temperature is going up, the electron temperature at 110 km and 115 km also increases, whereas the electron temperature elsewhere does not follow the same pattern. We note that there was not always exact simultaneity in the T_e and T_i increases, presumably because the observations were actually on slightly different magnetic field lines with perhaps somewhat different electric fields at any given time.

To get the trend of electron temperature enhancement I considered the data points from different altitudes (110 km, 115 km and 120 km) separately. The electron temperature at 110 km altitude has been considered for the further studies because it shows stronger heating than at 115 km. Then using LINFIT in IDL programing to study the behaviour of the electron temperature at 110 km a linear regression was obtained. But the linear regression (Figure 3.12) did not fit the data well in the sense that it could not take account of the fact that T_e starts to increase markedly only if T_i has become large enough. For this reason, I switched to a least squares fit to a second order polynomial, which produced a much better fit (Figure 3.13).

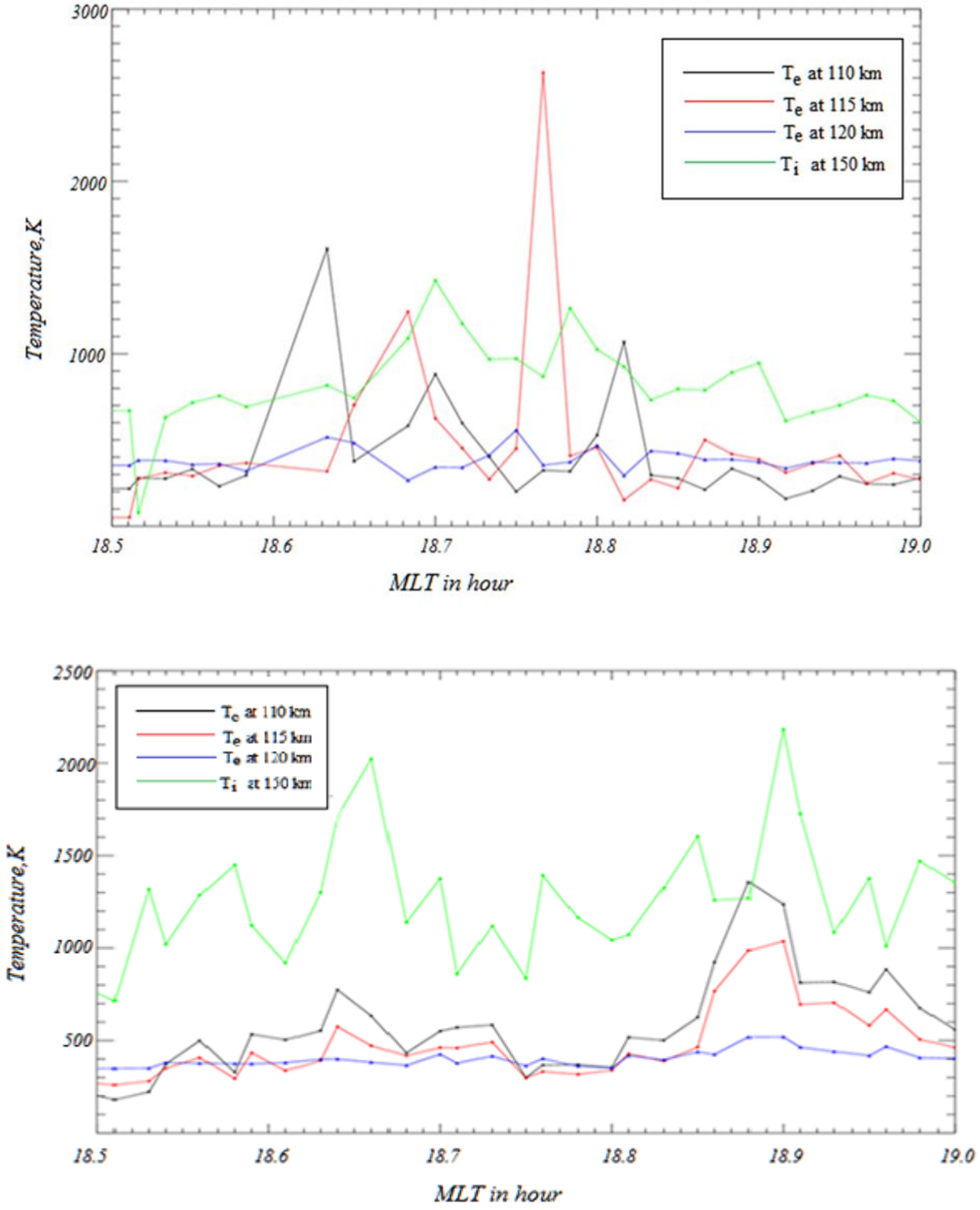

Figure 3.11: Time series for against magnetic field local time T_i at 150 km altitude and for T_e at 110 (black line), 115 (red line) and 120 (blue line) km altitude of 18th October, 2007 (Top Panel) and 5th February, 2008 (Bottom Panel).

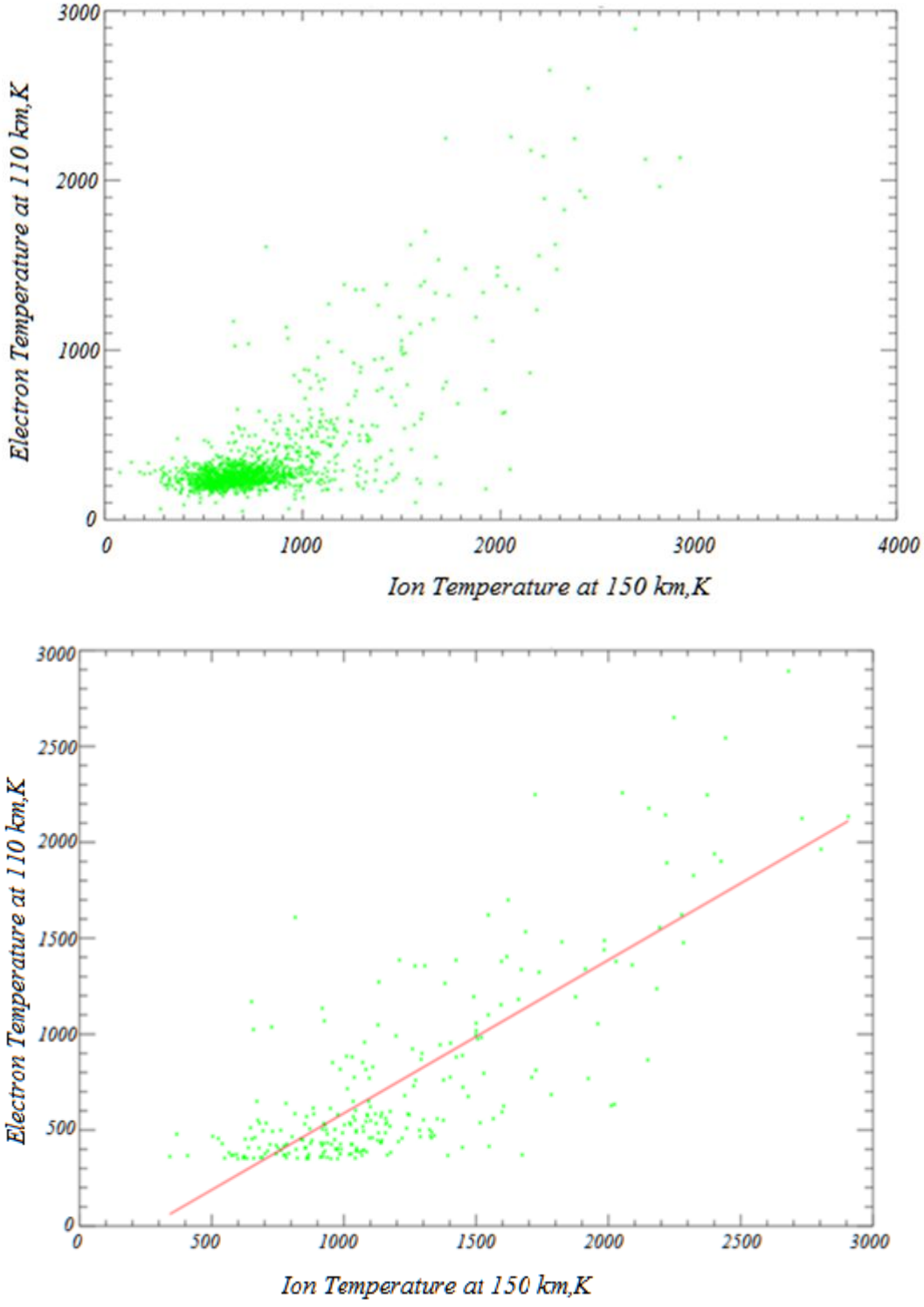

Figure 3.12: Scatter plot of T_e at 110 km and T_i at 150 km for all seven heating good events without linear regression (Top panel), and with linear regression (Bottom Panel). In the bottom panel only T_i in excess of 350 K was considered so as to allow the large temperature effects to be picked up by the correlation.

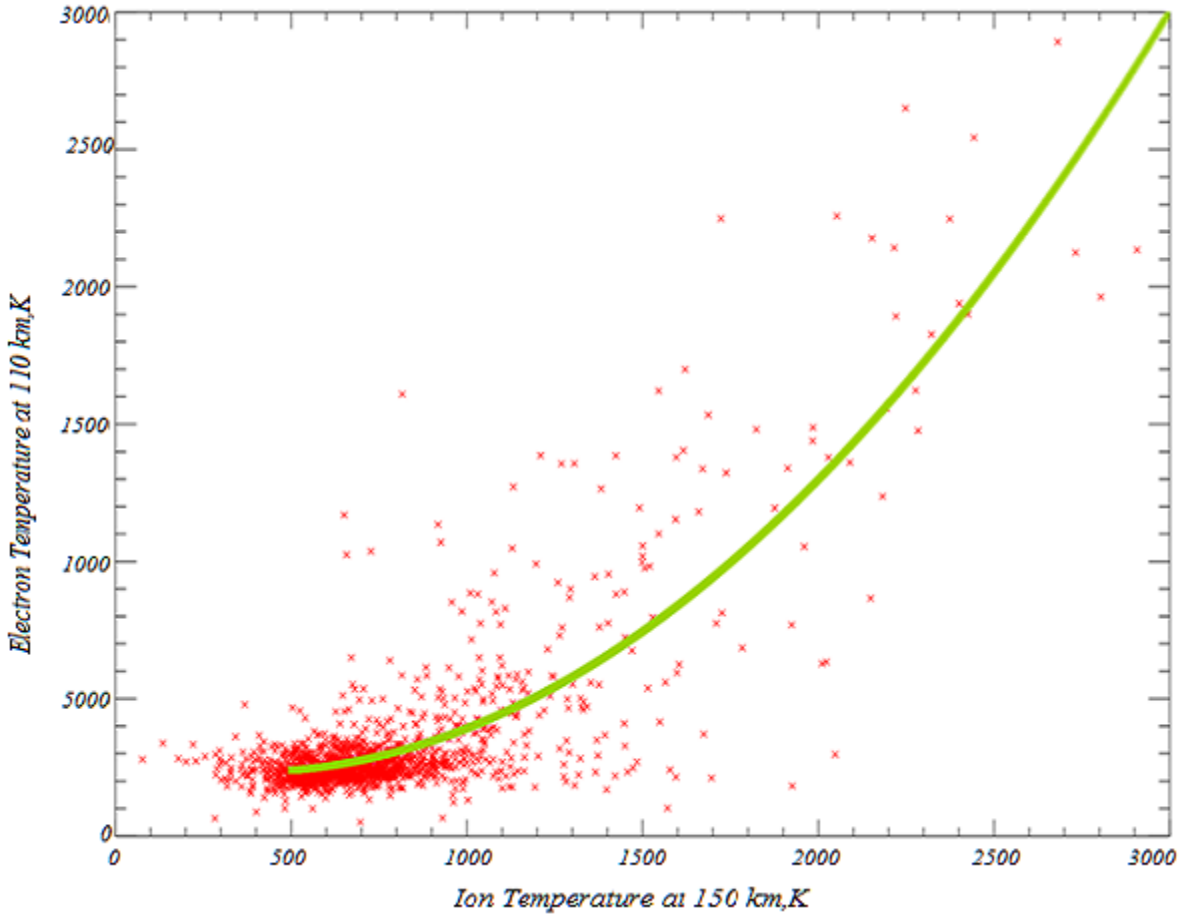

Figure 3.13: Scatter plot of T_e at 110 km and T_i at 150 km for all seven heating good events with a least square fit to a quadratic polynomial.

3.2.1 Conversion of ion temperatures to ion drifts magnitudes

The next task was to use the polynomial fit coefficient and to convert the ion temperature at 150 km into an electric field strength so as to be able to determine the response of the electron

temperature to the actual electric field. To this goal, the relation between the electric field and the parallel ion temperature was determined using the formula from *(St.-Maurice & Schunk, 1977).*

Below 400 km altitude, in the ion energy balance the dominant terms are frictional heating and heat exchange with neutrals. The results from the balance equation *(St.-Maurice & Hanson, 1982),*

$$T_i = T_n + m_n 3k_b \ \ (\boldsymbol{v_i} - \boldsymbol{v_n})^2 \tag{3.1}$$

When ion cooling by collisions is equal to ion heating by the friction we obtain, if we neglect $\boldsymbol{v_n}$,

$$T_i = T_n + \frac{m_n}{3k_b} v_i^2 \tag{3.2}$$

When the electric field becomes large, the ion temperature becomes anisotropic and the ion velocity distribution becomes non-Maxwellian with a larger temperature perpendicular to the magnetic field than along the magnetic field direction. In fact $T_{i\parallel} < T_i$.

We have *(Gaimard et. al, 1998)* and *(St.-Maurice, 1977)*

$$T_{i\parallel} = T_n \left(1 + \beta_\parallel \, m_n \frac{v_i^2}{2KT_n}\right) \tag{3.3}$$

$$T_{i\perp} = T_n \left(1 + \beta_\perp m_n \frac{v_i^2}{2KT_n}\right) \tag{3.4}$$

We must also satisfy the conditions

$$T_i = \frac{T_{i\parallel} + 2T_{i\perp}}{3}$$

which is equivalent to $\beta_\parallel + 2\beta_\perp = 1$. Here $\beta_\parallel$ and $\beta_\perp$ are pure numbers that depend on the ion-neutral collision model and on the mass ratio. For the present work we need $\beta_\parallel$ for the NO^+ in the presence of N_2.

From *St.-Maurice and Schunk (1977),*

$$T_{i\parallel} = T_n + \frac{1}{4}\left(1 + \frac{m_n}{m_i}\right)\frac{Q2}{Q1}\left[1 + \frac{3}{4}\frac{m_n}{m_i}\frac{Q2}{Q1}\right]^{-1}\frac{m_n D^2}{K} \tag{3.5}$$

$$T_{i\perp} = T_n + \frac{1}{2}\left[1 + \frac{1}{4}\left(2\frac{m_n}{m_i} - 1\right)\frac{Q2}{Q1}\right]\left[1 + \frac{3}{4}\frac{m_n}{m_i}\frac{Q2}{Q1}\right]^{-1}\frac{m_n D^2}{K} \tag{3.6}$$

Here Q2 and Q1 are integrals of the ion-neutral scattering cross-section. and $D = \frac{E_\perp}{B}$ is the magnitude of $\boldsymbol{E}_\perp \times \boldsymbol{B}$ drift. From these expressions we obtain

$$\beta_\parallel = \frac{1}{4}\left(1 + \frac{m_n}{m_i}\right)\left(\frac{Q2}{Q1}\right)\left(\frac{1}{\left(1+\frac{3m_nQ2}{4m_iQ1}\right)}\right) \tag{3.7}$$

$$\beta_\perp = \frac{\left(\frac{1}{2}\left[1+\frac{1}{4}\left(\frac{2m_n}{m_i}-1\right)\left(\frac{Q2}{Q1}\right)\right]\right)}{\left(1+\frac{3m_nQ2}{4m_iQ1}\right)} \tag{3.8}$$

It can be shown from these expressions that $\beta_\parallel + 2\beta_\perp = 1$ as expected

We can also write the results in the following form:

$$T_{i\parallel} = T_n\ [1 + \beta_\parallel D'^2\ ]$$

$$T_{i\perp} = T_n\ [1 + \beta_\perp D'^2\ ]$$

Where $D' = \frac{D}{vT_n}$ is the non-dimensional ion drift speed, with $v_{T_n} = \left(\frac{2KT}{m_n}\right)^{\frac{1}{2}}$ the neutral thermal. This also means,

$$T_i = \frac{T_n}{3}\ [3 + (\beta_\parallel + 2\beta_\perp)D'\ ] = T_n + \frac{\beta_\parallel + 2\beta_\perp}{2}\ D'^2\ T_n = T_n + \frac{1}{3}T_n\ D'^2 \tag{3.9}$$

This is consistent with the above since we have

$$T_i = T_n + \frac{\left(\frac{2}{3}T_n\left(\frac{E}{B}\right)^2\right)}{2KT_n}m_n \tag{3.10}$$

We can now proceed with actual numbers: we have, $\frac{m_n}{m_i} = \frac{28}{30} = \frac{14}{15}$, m_n and m_i being the masses of the neutral species and ions. Now, from *(Gaimard et. al, 1998)* for the field of interest (~50mV/m) got the value of $\frac{Q2}{Q1}$ =0.88. Therefore

$$\frac{\frac{1}{4}\left(1+\frac{m_n}{m_i}\right)\frac{Q2}{Q1}}{1+\frac{3}{4}\frac{m_n}{m_i}\frac{Q2}{Q1}} = \frac{\frac{1}{4}\left(\left(1+\frac{14}{15}\right)0.88\right)}{1+\frac{3}{4}\times\frac{14}{15}\times 0.88} = 0.263 \tag{3.11}$$

So, $T_{i\|} = T_n + 0.263m_n\frac{\left(\frac{E}{B}\right)^2}{K}$

However, we cannot neglect the atomic oxygen, O. So, if we consider O the average m_n should be less than 28 and $\frac{.263m_n}{K} \cong 7\times10^{-4}$ would be a lower limit. So, using $\frac{Q2}{Q1}$ =0.88 at 150 km and allowing for some atomic oxygen, a better result would give

$T_{i\|} = T_n + 7.5\times10^{-4}\times(20E)^2 = 3\times10^{-1}E^2$ for E in mV/m.

With these units, we then find that the ion temperature becomes at 150 km

$$T_{i\|} = T_n + .3E^2$$

We have found from the linear regression on a second degree polynomial (Appendix A) that

$$T_e = 286 - 0.2928T_{i\|} + 4.0210\times10^{-4}\ T_{i\|}^2$$

$$= 286 - 0.2928\left(T_n + 7\times10^{-4}\left(\frac{E}{B}\right)^2\right) + 4.0210\times10^{-4}\left(T_n + 7\times10^{-4}\left(\frac{E}{B}\right)^2\right)^2$$

Note that the ion drift velocity is

$$\boldsymbol{v}_i = \frac{\frac{\nu_i}{\Omega_i}}{1+\frac{\nu_i^2}{\Omega_i^2}} \frac{\boldsymbol{E}}{B} + \frac{1}{1+\frac{\nu_i^2}{\Omega_i^2}} \frac{\boldsymbol{E}\times\boldsymbol{b}}{B}$$

This implies

$$v_i^2 = \frac{\alpha_i}{1+\alpha_i^2}\left(\frac{E}{B}\right)^2 + \frac{1}{1+\alpha_i^2}\left(\frac{E}{B}\right)^2 = \left(\frac{E}{B}\right)^2 \frac{1}{1+\alpha_i^2}$$

where $\alpha_i = \nu_i/\Omega_i$. So, at 150 km

$$v_i^2 = \left(\frac{E}{B}\right)^2 \frac{1}{1+\left(\frac{\nu_i}{\Omega_i}\right)^2} \tag{3.12}$$

At 150 km $\frac{\nu_i^2}{\Omega_i^2} \cong 10^{-2}$, so, $v_i^2 = \left(\frac{E}{B}\right)^2 = (20E)^2$, that is, the ion drift is essentially the $\boldsymbol{E}\times\boldsymbol{B}$ drift. This means that the electron temperature equation can be written in terms of the electric field as

$$T_e = 286 - 0.2928(T_n + 7\times10^{-4}\,(20E)^2\,) + 4.0210\times10^{-4}\;\,(T_n + 7\times10^{-4}\,(20E)^2\,)^2$$

(3.13)

Using the Equation (3.13), the electron temperature vs ion velocity was plotted (Figure 3.14).

After plotting the electron temperature against the ion drift velocity the resultant plot was parabolic. Specifically, a plot from *(Erickson & Foster, 2000)* was adapted to include the present results for a precise comparison with previous work. I modified the figure from *Erickson & Foster*

(2000) by adding my own result. After comparing present results with previous observations *(Erickson & Foster, 2000)* , it could be concluded that the results were very similar. The result is presented in Figure 3.14. In that figure, the blue line is from the observation of *(Williams, et al., 1992),* were they studied the E-region heating as a function of F-region electric field observed on the same field line using EISCAT radar. The black line is from the Millstone Hill observations obtained after a carefully designed geometry that considered sidelobe coherent contamination from two-stream irregularities at 110 km. The red line is for the observation done by *Schlegel and St.-Maurice (1981)* where they studied the E-region electron temperature and F-region electric field using incoherent scatter radar at Chatanika. The green curve shows the present study. We see that the present data follow almost the same trends. The starting point of the present study is little lower than the other data sets, likely owing the low solar activity producing lower neutral temperatures.

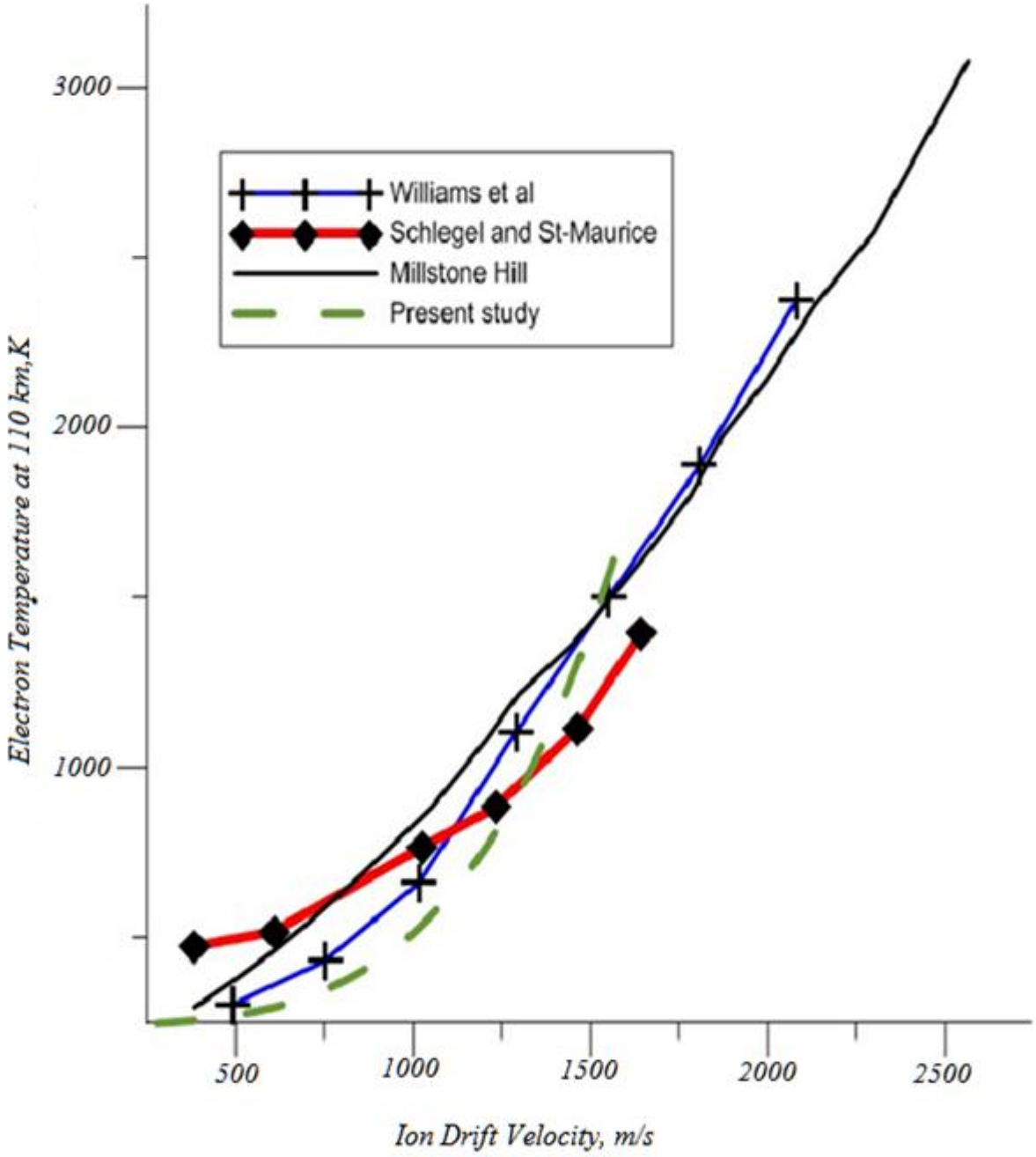

Figure 3.14: Composite plot of T_e vs ion drift at 110 km altitude.

Chapter 4

CONCLUSION AND FUTURE WORK

In earlier studies of the problem, it has been shown that the electron temperature around 110 km altitude can be quite large when the electric field is very strong. It has been assumed that this is caused by the Farley-Buneman instability in the E-region through the development of parallel electric fields that heat the electrons. However, a paper by *St.-Maurice et al., (1999)* gave an interesting exception. In this paper, they were looking for deviations from the normal trends and found a clear example of one exceptional event associated with a neutral wind anomaly. The strong neutral wind changed the effective electric field to the point that the electron temperature looked quite different from the norm. However, after correcting for the effective electric field instead of the electric field they found the same trend as with the rest of the data.

This thesis has focused on exploring the possibility of more deviations from the norm in high latitude E-region electron heating events. In this work, the data for an entire year from the EISCAT radar has been studied. The International Polar Year (IPY) was selected because the radars were operating continuously for almost the whole year. This gave a large number of dates or possible events for the study. However, in spite of the fact that there were many observations, only seven clean "good heating events" were found. This is probably because during the IPY, the Sun was very quiet. Therefore, there was not a large electric field very often. It turned out that the clean events agreed very well with past results. These events were all obtained when the electric field was strong and the electron density large enough to get good signal to noise and small error bars

(less than 15%). One difference with previous studies was with a smaller starting electron temperature. The reason behind the small starting temperature is probably that the neutral temperature was smaller because of the quiet solar conditions and the resulting reduced amount of EUV radiations. Aside from that, and was already stated, the new data agreed very well on average with previous work. This stated, there was often appreciable scatter in the data, but it was assumed that the scattering was due to uncertainties in the ion temperature at 150 km, which had to be used because there was no electric field data. In addition, there were uncertainties in the electron temperature lower down.

By examining the IPY dataset, we came across a different type of heating events. In that sense, it can be stated that there was indeed exceptions to the rules. In these events, the electron temperature at 110 km would be higher than expected in spite of a weak electric field. The exceptional events had several points in common. Firstly, the electron density was always very small, with for consequence that the uncertainty or the error bar in the determination was high. Secondly, in most of the unexpected heating events, the electron temperature was not peaking at 110 km but was steadily climbing up between 100 km and 250 km indicating that there was a different kind of electron heating in the E-region that has not been identified to date and was likely related to heat conducted from above.

References

Aikio, A., & Nygen, T. (2008). *Ionospheric Physics* . URL:https://wiki.oulu.fi/download/attachments/11767976/ionos_ch3.pdf?version=1&modificationDate=1245055843000&api=v2.

Bagad, V. (2009). *Radar System.* Technical Publications.

Bahcivan, H. (2007). Plasma wave heating during extreme electric fields in the high-latitude E-region. *Geophysical Research Letters, 34*, doi: 10.1029/2006GL029236.

Bahcivan, H.; Cosgrove, R.; Tsunoda, R..(2006). Parallel electron streaming in the high-latitude E-region and its effect on the incoherent scatter spectrum. *Journal of Geophysical Research*, 111, A07306, doi:10.1029/2005JA011595.

Baumjohann, W., & Treumann, R. (1996). *Basic Space Plasma Physics,* Imperial College Press.

Benyon, W. J., & Williams, P. J. (1978). Incoherent scatter of radio waves from the ionosphere. *Reports on Progress in Physics,* 41(6), doi:10.1088/0034-4885/41/6/003.

Bowles, K. (1958). Observation of vertical-incidence scatter from the ionosphere at 41 Mc/sec. *Physical Review Letters,* 1, 454-455.

Chain, Y. a. (2007). *Handbook Of the Solar-Terrestrial Environment*, Springer.

Christian R. E. (2012). *The Earth's Magnetosphere*. URL: http://cosmicopia.gsfc.nasa.gov/magnet.html

Dalipi, B., & Syla, N. (2013). Theoretical Analysis of Incoherent Scatter Radar Spectra Behavior for Different Maxwellian Ionospheric Plasma Conditions. *International Journal of Engineering & Technology, 13*, 42-48.

Danby, J. M. (1988). *Fundamentals of celestial mechanics.* Willmann-Bell, 2nd. Rev Sub Addition.

Davies, K. (1990). *Ionospheric Radio.* IET.

Diaz, M., Semeter, J., Oppenheim, M., & Zettergren, M. (2008). Particle-in-cell simulation of the incoherent scatter radar spectrum, *Radio Science,* 43(1), doi: 10.1029/2007RS003722.

Dimant, Y. S., & Oppenheim, M. (2003). Ion thermal effects on E-region instabilities: linear Theory. *Journal of Atmospheric and Solar-Terrestrial Physics,* 66, 1639-1654.

Dungey, W. J. (1961). Interplanetary Magnetic Field and the Auroral Zones. *Physical Review Letters*, 6, 47-48.

EISCAT, (2014). *EISCAT Scientific Association*. URL: https://www.eiscat.se

FAS. (1998). URL: http://www.fas.org/man/dod-101/navy/docs/es310/radarsys/radarsys.htm

Fejer, B. G., & Kelley, M. C. (1980). Ionospheric irregularities. *Reviews of Geophysics*, 18, 401-454.

Foster, P., & Erickson, J. (2000). Simultaneus Observations of E-region coherent backscatter and electric field amplitude at F-region heights with the Millstone Hill UHF radar. *Geophysical Research Letters* . 27, 3177-3180.

Gaimard, P., St.-Maurice, J.-P., Lathuillere, C., & Hubert, D. (1998). On the improvement of analytical calculations of collisional auroral ion velocity distributions using recent Monte Carlo results, *Journal of Geophysical Research*, 103(A3), 4079-4095.

Grydeland, T., Strømme, A., Eyken, T., & Hoz, C. (2013). The Capabilities of the EISCAT Svalbard Radar for Inter-hemispheric Coordinated Studies. *Chinese Journal of Polar Science, 13*(1), 55-66.

Haldoupis, C., Schlegel, K., & E. Nielsen. (1993). Some observations of radio auroral backscatter at 140 MHz during E-region electron gas heating. *Ann. Geophysics. , 11*, 283-295.

Hanuise, C. (1983). High-latitude ionospheric irregularities: A review of recent radar results. *Radio Science*, 18, 1093-1121.

Hargreaves, J., & Hunsucker, R. (2003). *The High latitude ionosphere and its effects on the radio propagation*, Cambridge University Press.

Hedin, M. (2002). Advanced applications of the EISCAT incoherent scatter radar for multi-beam and electron line studies, *IRF Scientific Report*, 277.

Howells, V. (2009).
URL:https://www.eiscat3d.se/drupal/sites/default/files/EISCAT_Radar_School_2012/09_Howells_CommonProgrammes.pdf

Hunsucker, R. (1991). *Radio Techniques For Probing the Terrestrial Ionosphere*, Springer-Verlag.

Incoherent Scatter Radar Tutorial. (2006). *Studying Space Weather – The Incoherent Scatter Radar*.
URL:http://www.haystack.mit.edu/edu/pcr/Data/pdf/Incoherent%20Scatter%20Radarfinal.pdf

Johnson, R. M., & Killen, T. (1995). *The Upper Mesosphere and Lower Thermosphere: A Review of Experiment and Theory.* American Geophysical Union.

Jones, B., Williams, P. J., Schlegel, K., Robinson, T., & I. Haggstrom. (1991). Interpretation of enhanced electron temperatures measured in the auroral E-region during the ERRRIS campaign. *Ann. Geophysics., 9*, 55-59.

Jursa, A. (1985). *Handbook of Geophysics and the Space Environment, Volume 1.* Air Force Geophysics Laboratory, Air Force Systems Command, U.S. Air Force.

Kelley, M. (2012). *The Earth's Ionosphere: Plasma Physics and Electrodynamics,* Academic Press.

Keskinen, M. J., & Ossakaw, S. L. (1983). *Theories of high-latitude ionospheric irregularities: A review,* Naval Research Laboratory.

Kivelson, M. G., & Russell, C. T. (2005). *Introduction to Space Physics.* Cambridge University Press.

Lapenta, G. (2014). *Open Magnetosphere and Reconnection*.
URL: https://perswww.kuleuven.be/~u0052182/weather/les3/node8.html

Limi, A., Runyan, A., & Andersen, V. (2014). *EISCAT-UK*. URL:www.eiscat.rl.ac.uk

Maeda, S., Nozawa, S., Sugino, M., Fujiwara, H., & Suzuki, M. (2002). Ion and neutral temperature distributions in the E-region observed by the EISCAT Tromsø and Svalbard radars. *Annales Geophysicae, 20*, 1415–1427.

Mark, A. R., James, A. S., & William, A. H. (2010). *Principles of Modern Radar: Basic Principles,* SciTech Publishing.

McFadden, T. J. (2006). *Encyclopedia of the Solar System.* Academic Press.

Mendillo, M., Baumgardner, J., & Sultan, P. J. (1990). Optical and Radar Techniques Applied to chemical Release 'Active Experiments' in the Ionosphere/Thermosphere System. *Journal of Geophysical Research. 97*(A4), 4084-4097.

Milikh, G. M., & Dimant, Y. (2002). Kinetic model of electron heating by turbulent electric field in the E region. *Geophys. Res. Lett., 29*, 16-1–16-4.

Milikh, G. M., & Dimant, Y. S. (2003). Model of anomalous electron heating in the E-region: 2. Detailed numerical modeling. *Journal of Geophysical Research, 108*. 6-1− 6-9.

Moses, R. W. (2004). The high-latitude ionosphere and its effects on radio propagation. *Eos, Transactions American Geophysical Union*, 85, doi:10.1029/2004EO190012.

NCAR High Altitude Observatory, (2004).
URL: http://www.meted.ucar.edu/hao/aurora/txt/x_m_3_2.php

No¨el, J. M., St.-Maurice, J.-P., & P.-L. Blelly. (2005). The effect of E-region wave heating on electrodynamical structures. *Ann. Geophysics*. 23, 2081-2094.

NOAA, NASA, & USAF. (1976). *U.S. Standard Atmosphere, 1976.*
URL:http://oai.dtic.mil/oai/oai?verb=getRecord&metadataPrefix=html&identifier=ADA035728

Oppenheim, M. (1996). A wave-driven nonlinear current in the E-region ionosphere. *Geophysical Research Letters, 23,* 3333-3336.

Pfaff, R. F., Kelley, M. C., Fejer, B. G., Kudeki, E., Carlson, C. W., Pedersen, A., & Hausler, B. (1984). Electric field and plasma density measurements in the auroral electrojet. *Journal of Geophysical Research: Space Physics, 89*, 236–244.

Primdahl, F., & Bahnsen, A. (1985). Auroral E region diagnosis by means of nonlinearly stabilized plasma waves. *Ann. Geophysics, 3*, 57-62.

Raman, S. V., St-Maurice, J. P., & Ong, R. S. (1981). Incoherent scattering of radar waves in the auroral ionosphere. *Journal of Geophysical Research, 86*, 4751-4762.

Rees, M. H. (1989). *Physics and Chemistry of the Upper Atmosphere*. Cambridge University Press.

Rees, M. H., & Walker, J. C. (1968). Ion and Electron Heating by Auroral Electric Fields. *Ann. Geophysics, 24*, 193-199.

Rich, F., & Basu, S. (1985). Ionospheric Physics. In A. S. Jursa, & U. A. Laboratory, *Handbook of Geophysics and the Space Environment.* [USA] : Air Force Geophysics Laboratory, Air Force Systems Command, United States Airforce, 1985.

Richmond, A., & Lu, G. (2000). Upper-atmospheric effects of magnetic stroms: a brief tutorial. *Journal of Atmospheric and Solar Terrestrial Physics, 62*, 1115-1127.

Rishbeth, H., & Williams P. J. S.,(1985). The EISCAT Ionospheric Radar - The System and its Early Results, *Royal Astronomical Society, 26*, 478-512.

Rishbeth, H., & Hanson, W. (1974). A comment on plasma 'pile-up' in the F-region. *Journal of Atmospheric and Terrestrial Physics, 36(4),* 703-706.

Robinson, T. R. (1986). Towards a self-consistent non-linear theory of radar auroral backscatter, *Journal of Atmospheric and Solar Terrestrial Physics, 48*, 417-422.

Roche, J. (1990). *Physicists Look Back: Studies in the History of Physics.* CRC Press.

Schlegel, K. (1996). Coherent Back Scatter from Ionospheric E-region Plasma Irregularities, *Journal of Atmospheric and Terrestrial Physics, 58,* 933–941.

Schlegel, K., & St.-Maurice, J.P. (1981). Anomalous Heating of the Polar E-region by Unstable Plasma Waves 1. Obsevations. *Journal of Geophysical Research, 86,* 1447-1452.

Schunk, R. W. (1975). Transport equations for aeronomy, *Planetary and Space Science,, 23 (3),* 437-485.

Schunk, R. W., & Nagy, A. (2000). *Ionospheres Physics, Plasma Physics, and Chemistry.* Cambridge University Press.

Schunk, R. W., & Nagy, A. F. (1978). Electron temperatures in the F region of the ionosphere: Theory and observations . *Reviews of Geophysics, 16(3),* 355-359.

Schunk, R. W., & Sojka, J. J. (1982). Ion temperature variations in the daytime high-latitude F region. *Journal of Geophysical Research, 87(A7),* 5169–5183.

St.-Maurice J. P., & Hamza A. M. (2001). A new nonlinear approach to the theory of E region irregularities. *Journal of Geophysical Research: Space Physics, 106,* 1751-1759

St.-Maurice, J. P., & Hanson, W. B. (1982). Ion frictional heating at high latitudes and its possible use for an in situ determination of neutral thermospheric winds and temperatures. *Journal of Geophysical Research, 87,* 7580-7602.

St.-Maurice, J. P. (Revised 2014). *Lectures in Aeronomy.*

St.-Maurice, J.-P. (1987). A unified theory of anomalous resistivity and Joule heating effects in the presence of E-region irregularities. *Journal of Geophysical Research, 92,* 4533-4542.

St.-Maurice, J.-P. (1990a). Electron heating by plasma waves in the high latitude E-region,Theory. *Advances in Space Research, 10,* 39-49.

St.-Maurice, J.-P., & Laher, R. (1985). Are observed broadband plasma wave amplitudes large enough to explain the enhanced electron temperatures of the high-latitude E region? *Journal of Geophysical Research, 90,* 2843-2850. .

St.-Maurice, J.-P., & Schlegel, K. (1981). Anomalous Heating of The Polar E-Region by Unstable Plasma Waves 2. Theory. *Journal of Geophysical Research, 86,* 1453-1462.

St.-Maurice, J.-P., & Schunk, R. W. (1977). Auroral ion velocity distributions for a polarization collision model. *Planetary and Space Science* , 243-260.

St.-Maurice, J.-P., Cussenot, C., & Kofman, W. (1999). On the usefulness of E region electron temperatures and lower F region ion temperatures for the extraction of thermospheric parameters: A case study. *Ann. Geophysics, 17,* 1182-1198.

St.-Maurice, J.-P., K. S., & Banks, P. (1981). Anomalous heating of the Polar E region by unstable plasma waves. II. Theory. *Journal of Geophysical Research, 86*, 1953-1962.

St.-Maurice, J.-P., Kofman, W., & James, D. (1996). In-situ generation of intense parallel fields in the lower ionosphere. *Journal of Geophysical Research, 101*, 335-356.

Sudan, R. N. (1983). Unified theory of type I and type II irregularities in the equatorial electrojet. *Journal of Geophysical Research, 88*, 4835–4860.

Virtanen, I. I., Lehtinen, M., Nygren, T., Orispaa, M., & Vierinen, J. (2008). Lag profile inversion method for EISCAT data analysis. *Ann. Geophysics, 26*, 571–581.

Wickwar, V. B., Lathuillere, C., Kofman, W., & Lejeune, G. (1981). Elevated electron temperatures in the auroral E layer measured. *Journal of Geophysical Research, 86*, 4721-4730.

Williams, P. J., Jones, B., & Jones, G. O. (1992). The Measured relationship between electric field strength and electron temparaturein the auroral E region. *Journal of Atmospheric and Terrestrial Physics, 54(6)*, 741-748.

Appendix : A

Linear Regression and Second Order Polynomial

The electron temperature data points (x_i, y_i). Fitting them in a linear model, Y= A+ Bx, is done by minimizing the chi-square error given by

$$\chi^2(A,B) = \sum_{i=1}^{N} (y_i - A - Bx_i)^2 \quad \text{(A1)}$$

By minimizing this equation, we get the value for A and B, namely, the derivatives of χ^2(A, B) at minimum give

$$\frac{\partial \chi^2}{\partial A} = 0 = -2\sum_{i=1}^{N}(y_i - A - Bx_i) \quad \text{(A2)}$$

And

$$\frac{\partial \chi^2}{\partial B} = 0 = -2\sum_{i=1}^{N} x_i(y_i - A - Bx_i) \quad \text{(A3)}$$

From equations A2 and A3 we define the entries

$$S1 = \sum_{i=1}^{N} x_i \quad , S2 = \sum_{i=1}^{N} y_i \ , S3 = \sum_{i=1}^{N} x_i^2 \ , S4 = \sum_{i=1}^{N} x_i y_i$$

Using these expressions, Equation A2 and A3 can be written as,

A+B.S1=S2

A.S1+B.S3=S4

The solution to these two equations give us the value of A and B

$$A = \frac{(S2.S3 - S1.S4)}{(S3 - S1^2)}$$

$$B = \frac{(S4 - S1.S2)}{(S3 - S1^2)}$$

I used LINFIT in my IDL programing to get the value of A and B.

The linear regression was not working well because it missed a lot of data points. So then I did a linear least Squares to a second order Polynomial. In this case we minimize

$$P = \sum_{i=1}^{N}(y_i - a - bx_i - cx_i^2)^2 \quad \text{(A4)}$$

Again taking the derivatives, we obtain for a minimum in P

$$\frac{\partial P}{\partial a} = 0 = -2\sum_{i=1}^{N} K$$

$$\frac{\partial P}{\partial b} = 0 = -2\sum_{i=1}^{N} x_i K$$

$$\frac{\partial P}{\partial c} = 0 = -2\sum_{i=1}^{N} x_i^2 K$$

Here $K = y_i - a - bx_i - cx_i^2$

Defining

$$D1 = \sum_{i=1}^{N} x_i \ , D2 = \sum_{i=1}^{N} x_i^2 \ , D3 = \sum_{i=1}^{N} x_i^3 \ , \ D4 = \sum_{i=1}^{N} x_i^4 \ , \ D5 = \sum_{i=1}^{N} y_i \ , D6 = \sum_{i=1}^{N} x_i y_i \ ,$$

$$D7 = \sum_{i=1}^{N} x_i^2 y_i$$

we end up with 3 equations given by

$$a + D1.b + D2.c = D5$$

$$D1.a + D2.b + D3.c = D6$$

$$D2.a + D3.b + D4.c = D7$$

The solution to these three equation give us the values of a, b and c through a simple matrix inversion. I obtained the solutions through IDL.